



**US Army Corps  
of Engineers®**  
Engineer Research and  
Development Center

Surge and Wave Island Modeling Studies (SWIMS) Program  
Coastal Inlets Research Program (CIRP)

# **Boussinesq Modeling of Wave Propagation and Runup over Fringing Coral Reefs, Model Evaluation Report**

Zeki Demirbilek and Okey G. Nwogu

December 2007

# **Boussinesq Modeling of Wave Propagation and Runup over Fringing Coral Reefs, Model Evaluation Report**

Zeki Demirbilek

*Coastal and Hydraulics Laboratory  
U.S. Army Engineer Research and Development Center  
3909 Halls Ferry Road  
Vicksburg, MS 39180-6199*

Okey G. Nwogu

*University of Michigan  
Department of Naval Architecture and Marine Engineering  
2600 Draper Road  
Ann Arbor, MI 48109-2145*

Final report

Approved for public release; distribution is unlimited.

**Abstract:** This report describes evaluation of a two-dimensional Boussinesq-type wave model, BOUSS-2D, with data obtained from two laboratory experiments and two field studies at the islands of Guam and Hawaii, for waves propagating over fringing reefs. The model evaluation had two goals: (a) investigate differences between laboratory and field characteristics of wave transformation processes over reefs, and (b) assess overall predictive capabilities of the model for reef systems with steep slopes and extended widths in shallower water. The focus in this evaluation study was on wave breaking, bottom friction parameterization, and wave setup and runup capabilities of Boussinesq wave model.

In this report, the testing procedure and performance of the Boussinesq wave model are discussed. Because details of the laboratory and field studies were unavailable at the time of writing, and these are expected to be documented in other reports, only some general features of data pertinent to the numerical modeling study are presented. The time series of laboratory and field data were used in the numerical model validation study. These were converted to wave energy spectral densities, significant wave height, peak wave period, and mean water level setup for comparison to model predictions. Findings from comparisons of measurements and model calculations are presented in figures and tables, and these are supplemented as necessary with discussion of the model's capability in describing different wave processes over coral reefs. Overall, the model performed reasonably well for laboratory data with errors of less than 10 percent for the maximum runup height. For the field data, it was determined that wave energy dissipation over extremely rough coral reef surfaces could not be simply described by a quadratic bottom friction law. Reasonable model-data agreement was obtained by using an eddy-viscosity type term to parameterize wave energy dissipation due to the turbulent boundary layer over rough coral reef bottoms.

**DISCLAIMER:** The contents of this report are not to be used for advertising, publication, or promotional purposes. Citation of trade names does not constitute an official endorsement or approval of the use of such commercial products. All product names and trademarks cited are the property of their respective owners. The findings of this report are not to be construed as an official Department of the Army position unless so designated by other authorized documents.

**DESTROY THIS REPORT WHEN NO LONGER NEEDED. DO NOT RETURN IT TO THE ORIGINATOR.**

# Contents

<b>Figures and Tables .....</b>	<b>iv</b>
<b>Preface .....</b>	<b>viii</b>
<b>Unit Conversion Factors .....</b>	<b>ix</b>
<b>1 Introduction .....</b>	<b>1</b>
Background .....	1
Literature review .....	2
<b>2 Description of Boussinesq Model .....</b>	<b>6</b>
Spilling wave breaking formulation (SBF) .....	8
Plunging wave breaking formulation (PBF) .....	9
Numerical solution .....	10
Critical model parameters for runup modeling .....	10
<b>3 Laboratory Experiments at ERDC-CHL .....</b>	<b>13</b>
Description of experiments .....	13
Test conditions .....	15
Validation of Boussinesq model .....	15
<b>4 Laboratory Experiments at University of Michigan .....</b>	<b>27</b>
Description of experiments .....	27
Test conditions .....	29
Validation of Boussinesq model .....	30
<b>5 Field Experiments at Mokuleia, Hawaii .....</b>	<b>44</b>
Description of experiments .....	44
Evaluation of Boussinesq model .....	45
<b>6 Field Experiments at Ipan, Guam .....</b>	<b>58</b>
Description of experiments .....	58
Evaluation of Boussinesq model .....	64
<b>7 Conclusions and Recommendations .....</b>	<b>77</b>
<b>References .....</b>	<b>80</b>
<b>Appendix A: Comparison of Measured and Calculated Wave Parameters for UM Laboratory Experiments .....</b>	<b>83</b>
<b>Appendix B: Comparison of Measured Runup Values with CEM Empirical Formulae .....</b>	<b>94</b>
<b>Appendix C: Comparison of Measured and Calculated Wave Heights for Guam Field Experiments .....</b>	<b>99</b>
<b>Report Documentation Page</b>	

# Figures and Tables

## Figures

Figure 1. Variation of wave friction factor with Reynolds number for smooth impermeable slopes. ....	12
Figure 2. Basin layout for laboratory experiments of Thompson (2005).....	13
Figure 3. Photograph of reef being built in CHL directional wave basin. ....	14
Figure 4. Cross-sectional view of laboratory setup of Thompson (2005). ....	14
Figure 5. Measured and calculated significant wave height distribution for GUAM01 test.....	16
Figure 6. Measured and calculated significant wave height distribution for GUAM02 test.....	16
Figure 7. Measured and calculated significant wave height distribution for GUAM12 test. ....	17
Figure 8. Measured and calculated significant wave height distribution for GUAM13 test.....	17
Figure 9. Measured and calculated wave spectra for GUAM01 test.....	19
Figure 10. Measured and calculated wave spectra for GUAM02 test. ....	19
Figure 11. Measured and calculated wave spectra for GUAM12 test. ....	20
Figure 12. Measured and calculated wave spectra for GUAM13 test. ....	20
Figure 13. Measured and calculated surface elevation time series for GUAM01 test. ....	21
Figure 14. Measured and calculated surface elevation time series for GUAM02 test. ....	22
Figure 15. Measured and calculated surface elevation time series for GUAM12 test. ....	23
Figure 16. Measured and calculated surface elevation time series for GUAM13 test. ....	24
Figure 17. Closeup view of measured and calculated surface elevation time series at Gauge 9 for GUAM12 test. ....	25
Figure 18. Experimental setup for UM fringing reef experiments.....	27
Figure 19. Plunging breaking waves for Test-18 near the reef crest.....	30
Figure 20. Measured and predicted significant wave height and mean water level variation for different wave breaking formulations (Test-29). ....	31
Figure 21. Measured and predicted significant wave height and mean water level variation for Test-36. ....	33
Figure 22. Measured and predicted significant wave height and mean water level variation for Test-29. ....	33
Figure 23. Measured and predicted significant wave height and mean water level variation for Test-48. ....	34
Figure 24. Measured and predicted significant wave height and mean water level variation for Test-17.....	34
Figure 25. Measured and predicted wave spectra for Test-36.....	35
Figure 26. Measured and predicted wave spectra for Test-29.....	35
Figure 27. Measured and predicted wave spectra for Test-48. ....	36
Figure 28. Measured and predicted wave spectra for Test-17.....	36
Figure 29. Measured and predicted surface elevation time series for Test-36.....	37
Figure 30. Measured and predicted surface elevation time series for Test-29.....	38

Figure 31. Measured and predicted surface elevation time series for Test-48. ....	39
Figure 32. Measured and predicted surface elevation time series for Test-17.....	40
Figure 33. Low-frequency wave energy spectra for Test-48 at Gauges 7-9. ....	41
Figure 34. Overview map of field site for Hawaii PILOT experiments. ....	44
Figure 35. 2D map of bathymetry near Mokuleia Beach used for Boussinesq model simulations.....	45
Figure 36. Wave climate recorded at Waimea Bay buoy in April 2004.....	46
Figure 37. Measured directional wave spectrum at Waimea Bay buoy on 3 April 2004 at 04:00 UTC. ....	47
Figure 38. Measured directional wave spectrum at Waimea Bay buoy on 7 April 2004 at 06:30 UTC. ....	48
Figure 39. Measured wave spectrum at Waimea Bay buoy on 3 April 2004 at 04:00 UTC.....	48
Figure 40. Measured wave spectrum at Waimea Bay buoy on 7 April 2004 at 06:30 UTC.....	49
Figure 41. Three-dimensional view of waves propagating over Mokuleia reef.....	50
Figure 42. Google satellite image of waves propagating over Mokuleia reef.....	50
Figure 43. Predicted significant wave height distribution for Storm Event 3 .....	51
Figure 44. Predicted significant wave height distribution for Storm Event 7 .....	51
Figure 45. Measured and predicted wave spectra at outer reef gauge for Storm Event 3.....	52
Figure 46. Measured and predicted wave spectra at mid-depth gauge for Storm Event 3.....	52
Figure 47. Measured and predicted wave spectra at nearshore gauge for Storm Event 3. ....	53
Figure 48. Measured and predicted wave spectra at outer reef gauge for Storm Event 7.....	53
Figure 49. Measured and predicted wave spectra at mid-depth gauge for Storm Event 7. ....	54
Figure 50. Measured and predicted wave spectra at nearshore gauge for Storm Event 7. ....	54
Figure 51. Measured and predicted wave spectra at outer reef gauge for Storm Event 7 obtained with two different values of Smagorinsky coefficient. ....	56
Figure 52. Measured and predicted wave spectra at mid-reef gauge for Storm Event 7 obtained with two different values of Smagorinsky coefficient. ....	57
Figure 53. Measured and predicted wave spectra nearshore at mid-reef gauge for Storm Event 7 obtained with two different values of Smagorinsky coefficient.....	57
Figure 54. Map showing geomorphological reef structure types near field site.....	59
Figure 55. Photograph of reef flat exposed at low tide.....	59
Figure 56. Cross-shore profile of reef along instrumentation transect. ....	60
Figure 57. Aquadopp profiler installed on reef crest. ....	60
Figure 58. Wave climate recorded by CDIP Sta 121 at Ipan in October 2005.....	61
Figure 59. Water level variation recorded at Pago Bay tide gauge in October 2005 .....	61
Figure 60. Significant wave heights and spectral peak periods recorded by Ipan reef gauges in October 2005.....	62
Figure 61. Wave height-to-water depth ratios recorded by Ipan reef flat gauges in October 2005.....	63
Figure 62. Mean current variation recorded by Ipan reef gauges in October 2005.....	64
Figure 63. Two-dimensional map of reef bathymetry near Ipan, Guam, used in BOUSS-2D model simulations.....	65

Figure 64. Three-dimensional view of waves from BOUSS-2D simulation propagating over lpan reef for Storm Event 264 .....	66
Figure 65. Predicted significant wave height field from BOUSS-2D simulation for Storm Event 264 .....	66
Figure 66. Computed and measured significant wave height variation along transect for Storm Event 264 .....	67
Figure 67. Measured and predicted wave spectra for Storm Event 264, different values of bottom friction coefficient. ....	68
Figure 68. Measured and predicted wave spectra for Storm Event 264 at AQD 57 with numerical gauge location moved 15 m shoreward. ....	69
Figure 69. Predicted significant wave height distribution for Storm Event 264.....	70
Figure 70. Computed and measured significant wave height variation along transect for Storm Event 243 .....	70
Figure 71. Computed and measured significant wave height variation along transect for Storm Event 252 .....	71
Figure 72. Computed and measured significant wave height variation along transect for Storm Event 264.....	71
Figure 73. Computed and measured significant wave height variation along transect for Storm Event 282 .....	72
Figure 74. Computed and measured significant wave height variation along transect for Storm Event 294 .....	72
Figure 75. Computed and measured significant wave height variation along transect for Storm Event 306 .....	73
Figure 76. Computed and measured significant wave height variation along transect for Storm Event 318 .....	73
Figure 77. Measured and predicted wave spectra for Storm Event 243 with Smagorinsky dissipation.....	75
Figure 78. Measured and predicted wave spectra for Storm Event 264 with Smagorinsky dissipation.....	76
Figure A1. Predicted versus measured significant wave height at Gauge 1. ....	83
Figure A2. Predicted versus measured significant wave height at Gauge 2. ....	84
Figure A3. Predicted versus measured significant wave height at Gauge 3. ....	85
Figure A4. Predicted versus measured significant wave height at Gauge 5. ....	86
Figure A5. Predicted versus measured significant wave height at Gauge 6. ....	87
Figure A6. Predicted versus measured significant wave height at Gauge 7.....	88
Figure A7. Predicted versus measured mean water level at Gauge 7.....	89
Figure A8. Predicted versus measured significant wave height at Gauge 8. ....	90
Figure A9. Predicted versus measured mean water level at Gauge 8.....	90
Figure A10. Predicted versus measured significant wave height at Gauge 9.....	91
Figure A11. Predicted versus measured mean water level at Gauge 9.....	92
Figure A12. Predicted versus measured maximum runoff at Gauge 9. ....	93
Figure B1. Measured $R_{2\%}$ runoff versus surf similarity parameter.....	96
Figure B2. Measured $R_{max}$ runoff versus surf similarity parameter.....	97

Figure B3. Correlation of best fit curve between measured $R_{2\%}$ runup and CEM empirical runup estimates based on deepwater wave parameters.....	97
Figure B4. Measured $R_{2\%}$ runup and CEM empirical runup estimates based significant wave height at toe of shore slope.....	98

## Tables

Table 1. Summary of simulated test conditions for laboratory experiments of Thompson (2005). .....	15
Table 2. Summary of measured and calculated maximum runup heights. ....	26
Table 3. Wave gauge coordinates.....	28
Table 4. Summary of test conditions.....	29
Table 5. Summary of measured and calculated maximum runup heights. ....	42
Table 6. Summary of selected storm events used in Boussinesq simulations for Mokuleia. ....	47
Table 7. Gauge locations in UTM coordinates.....	60
Table 8. Summary of selected storm events for Ipan simulations. ....	65
Table A1. Measured and predicted significant wave height and wave setup at Gauge 1.....	83
Table A2. Measured and predicted significant wave height and wave setup at Gauge 2.....	84
Table A3. Measured and predicted significant wave height and wave setup at Gauge 3.....	85
Table A4. Measured and predicted significant wave height and wave setup at Gauge 5.....	86
Table A5. Measured and predicted significant wave height and wave setup at Gauge 6.....	87
Table A6. Measured and predicted significant wave height and wave setup at Gauge 7.....	88
Table A7. Measured and predicted significant wave height and wave setup at Gauge 8.....	89
Table A8. Measured and predicted significant wave height and wave setup at Gauge 9.....	91
Table A9. Summary of measured and calculated maximum runup heights. ....	92
Table B1. Measured and calculated runup estimates.....	96
Table C1. Measured and predicted significant wave heights AQD44. ....	99
Table C2. Measured and predicted significant wave heights SBE78. ....	99
Table C3. Measured and predicted significant wave heights at AQD48.....	99
Table C4. Measured and predicted significant wave heights at SBE79. ....	100
Table C5. Measured and predicted significant wave heights at AQD57. <sup>1</sup> .....	100
Table C6. Measured and predicted significant wave heights at SBE80. ....	100
Table C7. Measured and predicted significant wave heights at AQD60. ....	101



## Preface

This technical report describes results of a two-dimensional Boussinesq model, BOUSS-2D, evaluation with laboratory and field data for waves over fringing reefs. This study of wave modeling for island flooding was performed jointly by the Surge and Wave Island Modeling Studies (SWIMS) Program and the Coastal Inlets Research Program (CIRP). The objective was to investigate capabilities of the model for waves propagating over fringing reefs at the Pacific islands of Guam and Hawaii and to validate the model with field data. The focus in model evaluation was on wave breaking, dissipation, wave setup, and wave runup capabilities of Boussinesq-type wave models. Field measurements were conducted along a complex reef system with steep frontal slopes in Guam and Hawaii. The data used in this study were obtained from Dr. Mark A. Merrifield, at the University of Hawaii, Manoa, under contract to the Pacific Islands Land Ocean Typhoon (PILOT) Experiment, which is an element of the U.S. Army Corps of Engineers (USACE), Coastal Field Data Collection (CFDC) Program.

The report is a joint product of collaborative research between SWIMS Program and CIRP. The lead program, SWIMS, is responsible for assembling a modeling system for prediction of flooding of Pacific islands. CIRP, in a supporting role, is responsible for developing, improving, and testing the BOUSS-2D wave model for USACE coastal applications. Both the SWIMS Program and CIRP are administered by Headquarters, USACE, and conducted at the U.S. Army Engineer Research and Development Center (ERDC), Coastal and Hydraulics Laboratory (CHL), Vicksburg, MS. Program Manager for SWIMS was William Birkemeier; Program Manager for CIRP was Dr. Nicholas C. Kraus. The study was performed by Dr. Zeki Demirbilek, Coastal Entrances and Structures Branch, Navigation Division, CHL, and Dr. Okey G. Nwogu of University of Michigan. Work at CHL was performed under the general supervision of Jose E. Sanchez, Chief of Coastal Entrances and Structures Branch; Dr. Rose M. Kress, Chief of Navigation Division; Dr. William D. Martin, Deputy Director, CHL; and Thomas W. Richardson, Director, CHL.

COL Richard B. Jenkins was Commander and Executive Director of ERDC. Dr. James R. Houston was Director.

## Unit Conversion Factors

Multiply	By	To Obtain
feet	0.3048	meters
knots	0.5144444	meters per second
miles (nautical)	1,852	meters
miles (U.S. statute)	1,609.347	meters
miles per hour	0.44704	meters per second

# 1 Introduction

## Background

Most of the Pacific islands are surrounded by fringing coral reefs that grow in shallow water close to the coastline. These reefs are characterized by wide-shallow platforms that sharply drop into deep water. In addition to providing habitat for a large variety of marine organisms, fringing reefs also protect coastal areas from wave action. Due to the shallow water on the reef flat, most of the incident wave energy is dissipated by waves breaking on the reef face. However, extensive damage has occasionally been reported in low-lying coastal areas fronted by coral reefs during typhoons (e.g., Ogg and Koslow 1978, Nakaza and Hino 1990, Jaffe and Richmond 1993). Damages occur during typhoons because of the surge (increased water level) over the reefs. Reliable estimates of waves over reefs are necessary as there may be a corresponding substantial increase in the wave runup on island shorelines at these increased water levels.

The U.S. Army Corps of Engineers (USACE) initiated the Surge and Wave Island Modeling Studies (SWIMS) Program in 2005 to develop improved methodologies for predicting coastal flooding associated with typhoons and hurricanes in the U.S. Pacific and Caribbean islands. Hurricanes are severe tropical cyclones with a sustained wind speed greater than 74 miles (119 km) per hour, according to the Saffir-Simpson scale. Hurricanes generally originate in the equatorial regions of the Atlantic Ocean or Caribbean Sea or eastern regions of the Pacific Ocean. The term hurricane is applied to storms which occur over the north Atlantic Ocean and, the northeast Pacific Ocean east of the dateline. The term typhoon is used in the northwest Pacific (west of the dateline). In the northern hemisphere, hurricane and typhoon winds rotate counterclockwise around a calm center, called the “eye.” In the south Pacific and Indian Oceans, the terms severe tropical cyclones or severe cyclonic storms are often used, and winds rotate clockwise. One of nature's most destructive forces, hurricanes and typhoons that reach the shore can cause enormous damage to life and property, precipitating mudslides, flash floods, storm surges, and wind and fire damage.

An understanding of the physics of wave inundation over reef systems is required to develop reliable predictive models for emergency planning and

the assessment of typhoon-induced erosion. The present methodology for predicting coastal inundation is based on empirical relationships presented in the *Shore Protection Manual* (SPM 1984) and *Coastal Engineering Manual* (CEM) (Headquarters, USACE 2002). The empirical relationships were derived from extensive series of laboratory experiments using both monotonic and composite slope structures. However, the relative berm widths (width of reef flat/incident wavelength) of fringing reefs are typically much wider than those of the structures used in the laboratory experiments to develop the CEM formulae. Nonlinear wave-wave interactions over wide reef flats lead to significant changes in the wave period. Hence, the empirical relationships in CEM may not be directly applicable to fringing-reef profiles and new relationships may be required. Seelig (1983) made an attempt in this regard by deriving a new set of empirical relations for the water level setup and runup over lagoon reefs. Demirbilek et al. (2007), however, noted differences between the wave setup over lagoon-reef tops and flat-reef tops. It is thus important to consider the exact profile of the reef in developing semi-empirical relationships for coastal flooding.

Spectral wave models could potentially be used to simulate wave transformation across reef profiles. Although linear spectral models can reasonably describe wave energy dissipation due to bottom friction and wave breaking, nonlinear wave-wave interactions over reefs lead to strong low-frequency (infragravity) oscillations of the water level near the shoreline. Runup limits associated with low-frequency oscillations over reef-type topographies can be significantly higher than those for planar beaches. Boussinesq-type water wave evolution models can describe the generation of infragravity waves by groups of short-period waves propagating from deep to shallow water (Nwogu 1993a). The parameterization of the effects of wave breaking and bottom friction in Boussinesq-type wave models represent simplifications of complex, turbulent nonlinear flows. Results of a systematic evaluation of a Boussinesq-type wave model are described in this report to determine the suitability of this technology for a tropical cyclone flooding simulation system.

## Literature review

A number of laboratory and field studies have been conducted since the 1970s to investigate wave transformation over coral reefs. One of the earliest field experiments was that by Lee and Black (1978). A linear array of seven gauges was deployed to measure the water surface elevation

time-histories across a fringing reef at Ala Moana Beach, Hawaii. The measured time records showed a significant change in the wave shape as the waves propagated over the reef. Waves breaking on the reef face reformed on the reef flat as steep asymmetric bore-like waves with multiple crests. The measurements also showed significant changes in the wave height probability distribution and wave energy spectra over the reef. Non-linear wave-wave interaction led to the cross-spectral transfer of energy from the spectral peak frequencies to lower and higher frequencies. The probability distribution of the sea surface elevation and wave heights over the reef flat also deviated from the theoretical Gaussian and Rayleigh distributions for linear waves.

Wave energy dissipation rates have also been found to be significantly higher over coral reef platforms than on sandy beaches. Several investigators (Roberts 1975, Lugo-Fernandez et al. 1998, Brander et al. 2004) have reported attenuation rates of 75-95 percent of the incident wave energy over reef flats. Although most of the wave energy dissipation is attributed to wave breaking, bottom friction and percolation also play an important role in the dissipation process. Coral reefs have rough and porous surfaces. Estimates of the bottom friction coefficient for coral reefs are considerably greater than those for sandy beaches (Gerritsen 1980, Nelson 1996, Lowe et al. 2005).

Laboratory investigations into the mean water level setup over reefs have been conducted by Gerritsen (1980), Seelig (1983), Gourlay (1996), and Demirbilek et al. (2007), among others. Seelig (1983) investigated a reef-lagoon profile that was characteristic of several sites along the Guam coast. He found that the mean water level setup in the lagoon increased with the wave power parameter  $H_0^2 T_p$ , where  $H_0$  is the deepwater significant wave height and  $T_p$  is the spectral peak period. The setup also increased as the still-water level over the reef flat decreased. Gerritsen (1980) and Gourlay (1996) both described the non-dimensional wave setup  $\bar{\eta} / H_0$  in terms of the relative water depth over the reef flat  $h_r / H_0$  and a wave steepness parameter  $H_0 / g T_p^2$ . Gourlay (1996) presented simplified expressions for the wave setup depending on whether the waves were breaking on the reef face or on the reef flat.

Numerical models have also been developed to predict wave setup over coral reefs. Most use the shallow-water equations with a forcing term produced by the gradient of the radiation stress (Longuet-Higgins and

Stewart 1964). Tait (1972) calculated the radiation stress gradient throughout the surf zone by assuming the post-breaking wave height to be a constant fraction of the water depth. The concept of a constant height to depth ratio becomes questionable for complex reef profiles given the large range of observed values of wave height to water depth ratio. Gerritsen (1980) improved upon this approach by solving the wave energy conservation equation with the wave breaking dissipation model of Battjes and Janssen (1978). Symonds et al. (1995) noted that cross-reef currents could affect the water level setup and derived an analytical solution for the wave setup and cross-reef current over an idealized atoll reef without a shoreward land boundary. Massel and Gourlay (2000) used the extended mild-slope equation to predict wave transformation across reef profiles. Wave breaking was parameterized with a modified form of the Battjes and Janssen (1978) breaking formulation.

There have been few laboratory or field studies of wave runup on beaches fronted by fringing coral reef systems. The laboratory study by Seelig (1983) presented results of wave runup height and reported differences between the runup characteristics of regular and irregular waves. Although regular waves induced a larger setup of the mean water level in the lagoon, the maximum runup values were much higher in irregular sea states due to strong low-frequency oscillations in the lagoon and near the shoreline. Demirbilek et al. (2007) conducted experiments for regular and irregular waves and developed a comprehensive data set of wave setup, wave runup, wave height, and wave spectra evolution with and without wind forcing. Their experiments showed infragravity waves developing over the reef flat and presence of both shore-ward and offshore-moving bores in the post wave breaking region on the reef top.

Infragravity wave oscillations have also been postulated to be responsible for the observed coastal damage along the reef coasts of Japan during typhoons (Nakaza and Hino 1990). Infragravity waves can be trapped and resonantly amplified over a reef flat if the wave period is close to one of the natural reef oscillation periods. It is necessary that predictive models for coastal flooding over reef-fronted coasts be capable of describing low-frequency (infragravity) oscillations over a reef in addition to other hydrodynamic processes such as wave breaking, wave setup, wave reflection, bottom friction, percolation, breaking-induced currents, and wave-current interaction.

Numerical models based on Boussinesq-type water wave evolution equations can describe the generation of low-frequency waves by groups of short-period waves propagating from deep to shallow water. Boussinesq models have also been extended to simulate wave runup and coastal flooding (e.g., Kennedy et al. 2005, Nwogu and Demirbilek 2007). However, the effects of wave breaking and bottom friction are still parameterized in Boussinesq models. Because the parameterizations represent simplifications of complex turbulent nonlinear processes, it is useful to evaluate the capability of the different parameterized wave models to describe the physics of wave energy dissipation, infragravity wave motions, and wave runup across wide fringing reefs characteristic of the Pacific islands.

This report documents preliminary comparison of Boussinesq model simulations with two laboratory and two field data sets to assess the model's suitability for predicting typhoon and hurricane induced flooding along the reef-fringed islands. The layout of this report is as follows. A brief description of Boussinesq-type wave theory and the numerical model BOUSS-2D is provided in Chapter 2. Model evaluation with data from a 1:36 laboratory model study conducted in 2005 at the U.S. Army Engineer Research and Development Center, Coastal and Hydraulics Laboratory (CHL), is described in Chapter 3. A detailed model evaluation is provided in Chapter 4 for a large set of test conditions from a 1:80 laboratory model study performed in 2006 at the University of Michigan Wind-Wave Facility. In Chapter 5, model evaluation is discussed for field data collected in 2004 at Mokuleia, Hawaii. Chapter 6 provides model evaluation with data obtained in 2005 at Ipan, Guam, as part of the Pacific Islands Land-Ocean Typhoon (PILOT) experiment. Overall conclusions are provided in Chapter 7. Supporting material is provided in Appendices A through C for model-data comparisons as well as a comparison to the empirical wave runup formula of the CEM.

## 2 Description of Boussinesq Model

The numerical model investigated in the present study is BOUSS-2D, and it is based on a fully nonlinear variant of the set of Boussinesq equations derived by Nwogu (1993b). Additional information on Boussinesq equations and BOUSS-2D can be found in Nwogu and Demirbilek (2007), Nwogu and Demirbilek (2006), Asmar and Nwogu (2006), Nwogu (1996), Demirbilek et al. (2005a and 2005b), and Nwogu and Demirbilek (2001). The depth-integrated mass and momentum equations can be written in terms of the free surface elevation  $\eta(\mathbf{x},t)$  (where  $\mathbf{x}$  denotes the two horizontal directions and  $t$  is time), the depth-averaged horizontal velocities  $\bar{\mathbf{u}}$ , and the horizontal velocity at elevation  $z = z_\alpha$  below the still-water level,  $\mathbf{u}_\alpha(\mathbf{x},t)$ , as

$$\eta_t + \nabla \cdot [(h + \eta)\bar{\mathbf{u}}] = 0 \quad (1)$$

$$\begin{aligned} \mathbf{u}_{\alpha,t} &+ g\nabla\eta + (\mathbf{u}_\eta \cdot \nabla)\mathbf{u}_\eta + w_\eta \nabla w_\eta \\ &+ (z_\alpha - \eta)[\nabla(\mathbf{u}_{\alpha,t} \cdot \nabla h) + (\nabla \cdot \mathbf{u}_{\alpha,t})\nabla h] \\ &+ \frac{1}{2}[(z_\alpha + h)^2 - (h + \eta)^2]\nabla(\nabla \cdot \mathbf{u}_{\alpha,t}) \\ &- [(\mathbf{u}_{\alpha,t} \cdot \nabla h) + (h + \eta)\nabla \cdot \mathbf{u}_{\alpha,t}]\nabla\eta \\ &+ \frac{1}{h + \eta}\nabla[\nu(h + \eta)\nabla \cdot \mathbf{u}_\alpha] + \frac{f_w}{2(h + \eta)}\mathbf{u}_b|\mathbf{u}_b| = 0 \end{aligned} \quad (2)$$

where  $g$  is the gravitational acceleration,  $h$  is the seabed elevation (defined as positive downwards from the still-water level),  $f_w$  is a bottom friction coefficient,  $\nu(\mathbf{x},t)$  is an eddy viscosity coefficient,  $\mathbf{u}_\eta$  and  $w_\eta$  are the horizontal and vertical velocities at the free surface ( $z = \eta$ ),  $\mathbf{u}_b$  is the horizontal velocity at the seabed ( $z = -h$ ), and the subscript  $t$  indicates a time derivative. The horizontal and vertical velocities required to close the system of equations are obtained from a second-order Taylor series expansion of the velocity field about  $z = z_\alpha$ :

$$w_\eta = -[\mathbf{u}_\alpha \cdot \nabla h + (h + \eta)\nabla \cdot \mathbf{u}_\alpha] \quad (3)$$



$$\begin{aligned} \mathbf{u}_\eta = \mathbf{u}_\alpha + (z_\alpha - \eta) [\nabla(\mathbf{u}_\alpha \cdot \nabla h) + (\nabla \cdot \mathbf{u}_\alpha) \nabla h] \\ + \frac{1}{2} [(z_\alpha + h)^2 - (h + \eta)^2] \nabla(\nabla \cdot \mathbf{u}_\alpha) \end{aligned} \quad (4)$$

$$\begin{aligned} \mathbf{u}_b = \mathbf{u}_\alpha + (z_\alpha + h) [\nabla(\mathbf{u}_\alpha \cdot \nabla h) + (\nabla \cdot \mathbf{u}_\alpha) \nabla h] \\ + \frac{1}{2} (z_\alpha + h)^2 \nabla(\nabla \cdot \mathbf{u}_\alpha) \end{aligned} \quad (5)$$

$$\begin{aligned} \bar{\mathbf{u}} = \mathbf{u}_\alpha + \left[ (z_\alpha + h) - \frac{(h + \eta)}{2} \right] [\nabla(\mathbf{u}_\alpha \cdot \nabla h) + (\nabla \cdot \mathbf{u}_\alpha) \nabla h] \\ + \left[ \frac{(z_\alpha + h)^2}{2} - \frac{(h + \eta)^2}{6} \right] \nabla(\nabla \cdot \mathbf{u}_\alpha) \end{aligned} \quad (6)$$

The elevation of the velocity variable is chosen to be  $z_\alpha = -0.535h$  (for  $h > 0$ ) to minimize differences between the linear dispersion characteristics of the Boussinesq model and the exact dispersion relation for small amplitude waves (Nwogu and Demirbilek 2006 and 2007). To ensure that the velocity variable remains in the water column during wave propagation over initially dry land, the location of the velocity variable is switched to the seabed for land regions, i.e.,  $z_\alpha = -h$  for  $h < 0$ .

The effect of wave breaking has been parameterized in the momentum equation (Equation 2) with an artificial eddy viscosity term. This term is designed to reproduce the overall wave energy dissipation due to wave breaking, but it does not produce the details of the turbulent motion. A conceptual breaking model is still required to define the onset of breaking and the post-breaking evolution of the eddy viscosity in space and time. We tested two formulations for describing the spatial and temporal evolution of the eddy viscosity after the onset of breaking. The first approach is the one currently implemented in BOUSS-2D (Nwogu and Demirbilek 2001) and is based on the formulation of Nwogu (1996) for spilling breakers. Unless otherwise stated, all simulations in this report are based on that approach. We also developed and tested a new formulation that might be more applicable to plunging breakers that occur on the faces of reefs with steep slopes. These formulations are described next.

## Spilling wave breaking formulation (SBF)

The spilling breaker formulation is based on an analogy with the one-equation turbulence closure model used for the Navier-Stokes equations. The eddy viscosity coefficient  $\nu$  is related to the kinetic energy of the large-scale eddy motions,  $k$ , and an eddy length scale,  $l$ , by

$$\nu = \sqrt{k}l \quad (7)$$

A one-dimensional (1D) transport equation describes the production, advection, diffusion, and dissipation of the eddy kinetic energy:

$$k_t + \mathbf{u}_\eta \cdot \nabla k = P - D + \sigma \nu \nabla^2 k \quad (8)$$

where  $\sigma$  is an empirical diffusion coefficient, and  $P$  and  $D$  are terms representing the production and dissipation of eddy kinetic energy, respectively. The breaking model assumes that eddies are generated in the near-surface region and primarily advected with the horizontal velocity at the free surface. The rate of production of the eddy kinetic energy is assumed to be proportional to the vertical gradient of the velocity at the free surface:

$$P = B \frac{l^2}{\sqrt{C_D}} [\mathbf{u}_{z,\eta} \cdot \mathbf{u}_{z,\eta}]^{3/2} \quad (9)$$

where  $C_D$  is an empirical coefficient, and the velocity gradient  $\mathbf{u}_{z,\eta}$  is given by

$$\mathbf{u}_{z,\eta} = -[\nabla(\mathbf{u}_\alpha \cdot \nabla h) + (\nabla \cdot \mathbf{u}_\alpha) \nabla h] - (h + \eta) \nabla(\nabla \cdot \mathbf{u}_\alpha) \quad (10)$$

The parameter  $B$  is introduced in Equation 9 to ensure that eddy generation occurs after the waves break. The waves are assumed to start breaking if the horizontal component of the orbital velocity at the free surface,  $\mathbf{u}_\eta$ , exceeds 80 percent of the phase velocity of the waves,  $C$ :

$$B = \begin{cases} 0 & |\mathbf{u}_\eta| < 0.8C \\ 1 & |\mathbf{u}_\eta| \geq 0.8C \end{cases} \quad (11)$$

The last unknown term in the breaking model is the rate of dissipation of eddy kinetic energy. We assume that it follows the standard 3/2 decay law:

$$D = C_D \frac{k^{3/2}}{l} \quad (12)$$

The following values were adopted for the empirical constants:  $C_D = 0.08$  and  $\sigma = 0.2$ , as recommended by Nwogu (1996). The eddy length scale,  $l$ , remains the only free parameter in the SBF and is typically chosen to be on the order of the wave height (Demirbilek et al. 2005a and 2005b, Nwogu and Demirbilek 2001).

### Plunging wave breaking formulation (PBF)

A wave breaking formulation that is more applicable to plunging wave breakers is based on the concept of localized energy dissipation at the front of a shock or discontinuity with the eddy viscosity proportional to the velocity gradient at the wave front (e.g., Smagorinsky 1963). In BOUSS-2D notation, this may be written as

$$\nu(\mathbf{x}, t) = B(\mathbf{x}, t) l^2 [u_{s,x}^2 + v_{s,y}^2]^{1/2} \quad (13)$$

where  $l$  is a characteristic length scale that is related to the wave height,  $B(\mathbf{x}, t)$  is a breaking wave factor that ranges from 0 to 1, and  $\mathbf{u}_s$  is the tangential velocity at the free surface:

$$\mathbf{u}_s(\mathbf{x}, t) = \mathbf{u}_\eta + w_\eta \nabla \eta \quad (14)$$

An advection-diffusion equation is solved for the spatial and temporal evolution of the wave breaking factor:

$$\frac{\partial B}{\partial t} + u_\eta \frac{\partial B}{\partial x} + v_\eta \frac{\partial B}{\partial y} = -\frac{\pi}{T_v} B + \sigma \nu \left( \frac{\partial^2 B}{\partial x^2} + \frac{\partial^2 B}{\partial y^2} \right) \quad (15)$$

where  $\sigma$  is an empirical diffusion constant,  $T_v$  denotes a characteristic time scale over which the breaking factor decays to 4 percent of its initial value, and the value of  $B$  is initially set to 1 if a wave is classified as breaking according to Equation 11. The values of  $l$ ,  $T_v$ , and  $\sigma$  may be chosen by users on the basis of guidance given in BOUSS-2D model references (e.g., see

Demirbilek et al. 2005a and 2005b, and Nwogu and Demirbilek 2001). For the simulations in this report, unless otherwise noted, the following values have been used:  $l = H_s$ ,  $T_v = 5T_p$ , and  $\sigma = 0.2$ .

## Numerical solution

The governing equations, Equations 1-6, are integrated in time using a finite-difference method. The computational domain is discretized as a rectangular grid with the prognostic variables  $\eta$  and  $\mathbf{u}_\alpha$  defined at the grid points in a staggered manner. The surface elevation is defined at the grid nodes, and the velocities are defined half a grid point on either side of the elevation grid points. A modified third-order accurate Crank-Nicholson scheme is used to integrate the equations (Nwogu and Demirbilek 2001). A simple but robust scheme (Nwogu and Demirbilek 2007) is used to simulate the flooding and drying of computational cells. A Smagorinsky-type artificial viscosity term smoothes out spurious numerical oscillations at the front of moving boundaries:

$$\nu = C_v^2 \Delta x \Delta y \left[ (u_{\alpha,x})^2 + (v_{\alpha,y})^2 + \frac{1}{2} (u_{\alpha,y} + v_{\alpha,x})^2 \right]^{1/2} \quad (16)$$

where  $C_v$  is an empirical coefficient that is related to the width of the shock or discontinuity, and  $\Delta x$  and  $\Delta y$  are the grid sizes along the x and y axes.

## Critical model parameters for runup modeling

Several BOUSS-2D model parameters can influence the runup estimates (Demirbilek et al. 2005a and b; Nwogu and Demirbilek 2001) including the following:

1. *Minimum flooding depth,  $\delta_{min}$* : To avoid instability associated with evaluating the bottom friction term in cells with extremely small water depths, a minimum depth criterion is applied to flooded cells. If the calculated water depth in any cell is less than a specified threshold, the cell is considered to be dry and excluded from the computations. The recommended default value is  $\delta_{min} = H/1000$ , where  $H$  is the average zero-crossing incident wave height used as input in a BOUSS-2D simulation.
2. *Smagorinsky eddy viscosity coefficient,  $C_v$* : The Smagorinsky coefficient stabilizes the runup computations but can also cause excessive numerical dissipation if the coefficient is too large. The typical range for  $C_v$  is from 0 to 1, with a recommended default value  $C_v = 0.2$ .

3. *Wave-breaking turbulent length scale,  $l$* : The eddy length scale parameter controls the rate of wave energy dissipation for breaking waves. The greater the value of  $l$ , the stronger is the rate of wave energy dissipation. The recommended default value for  $l$  is the offshore significant wave height, i.e.,  $l = H_s$  for irregular waves.
4. *Bottom friction coefficient,  $f_w$* : Wave energy dissipation due to the turbulent boundary at the seabed has been parameterized in Equation 2 as a quadratic drag term with a wave friction factor  $f_w$  or Chezy coefficient,  $C_f = \sqrt{2g / f_w}$ , where  $g = 9.81 \text{ m/sec}^2$ . The friction factor can vary over a large range (0.001 to 1.0), depending on the Reynolds number and relative roughness of the seabed. For smooth impermeable slopes, the friction factor is given by (Fredsoe and Deigard 1992)

$$f_w = \begin{cases} \frac{2}{R_b} & \text{for laminar boundary layers } (R_b < 2 \times 10^5) \\ \frac{0.035}{R_b^{0.16}} & \text{for turbulent boundary layers } (R_b > 2 \times 10^5) \end{cases} \quad (17)$$

where  $R_b$  is the Reynolds number based on the bottom velocity and amplitude of the orbital motion at the seabed ( $R_b = \frac{u_b a_b}{\nu}$ ). Figure 1 shows a plot of the wave friction factor versus Reynolds number for smooth slopes. For rough impermeable slopes, the wave friction factor is independent of the Reynolds number and is a function of the relative roughness (e.g., Kamphuis 1975):

$$\left. \begin{aligned} f_w &= 0.025 \left( \frac{k_e}{a_b} \right)^{3/4} \text{ for } k_e / a_b > 0.02 \\ \frac{1}{4\sqrt{f_w}} + \ln \frac{1}{4\sqrt{f_w}} &= -0.35 - \frac{4}{3} \ln \frac{k_e}{a_b} \text{ for } k_e / a_b < 0.02 \end{aligned} \right\} \quad (18)$$

where  $k_e = 2d_{90}$  is the bottom roughness and  $a_b$  is amplitude of the wave orbital motion at the seabed. The default value for  $f_w$  in BOUSS-2D is 0.02 or  $C_f = 30 \text{ m}^{1/2}/\text{sec}$  (Demirbilek et al. 2005a and b; Nwogu and Demirbilek 2001). *For convenience, the units of Chezy coefficient will be henceforth omitted, but it is understood that stated values of the parameter are dimensional.*

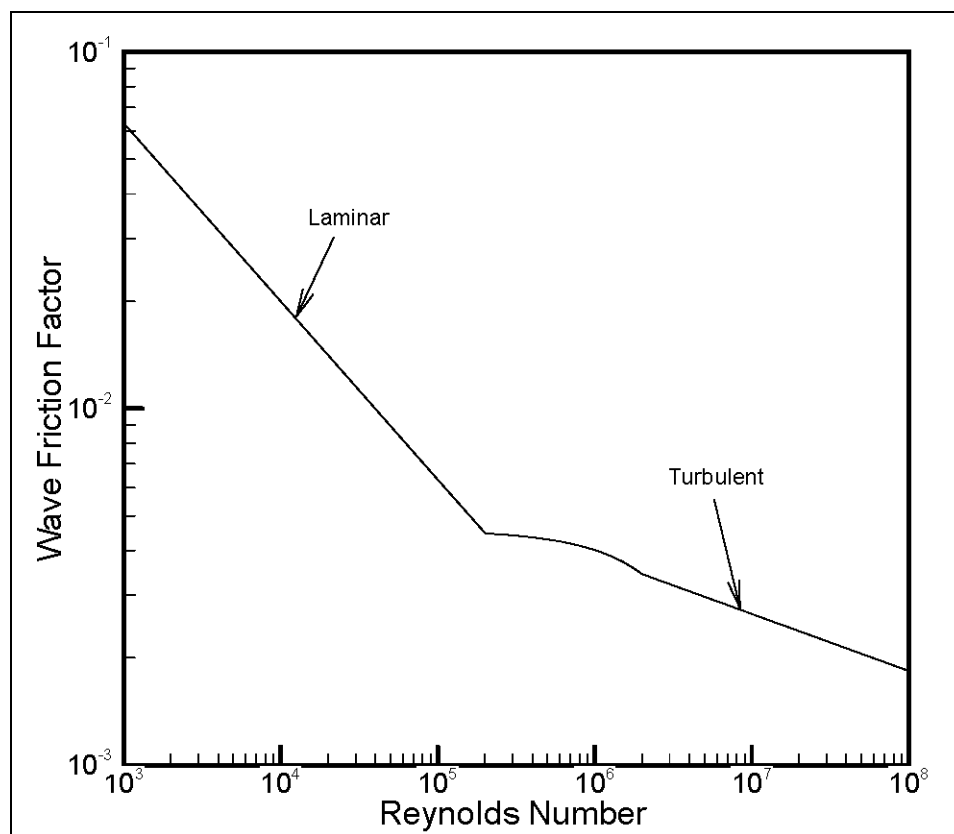


Figure 1. Variation of wave friction factor with Reynolds number for smooth impermeable slopes.

The key elements of the approach used in this research can be summarized as follows:

1. Evaluate model against laboratory and field data to determine suitability for reef applications by investigating the sensitivity of model predictions to parameterized wave processes (breaking and dissipation).
2. Determine appropriate values for adjustable model parameters including wave friction factor, wave breaking dissipation parameter (turbulent-length scale), Smagorinsky eddy-viscosity coefficient (sub-grid processes), and minimum flooding depth.
3. Investigate universal parameterization for plunging/spilling breakers, generation of nonlinear waves in shallow depths, and details of wave runup/rundown on steep slopes.

Investigation of these objectives is described in the following chapters of this report where BOUSS-2D model has been evaluated with two laboratory and two field data sets.

### 3 Laboratory Experiments at ERDC-CHL

#### Description of experiments

Thompson (2005) conducted two-dimensional (2D) laboratory experiments in the 29-m-wide by 52-m-long directional wave basin of CHL to investigate wave transformation across fringing reefs. An 18-m-long by 2.44-m-wide slope-reef bathymetry was built in the middle of the basin as shown in Figures 2 and 3. The cross-sectional profile of the reef face is similar to the one used in previous hydraulic model tests by Seelig (1983). However, a fringing reef configuration with a flat reef top was set up in these experiments instead of the barrier reef configuration with a lagoon as reported by Seelig (1983). The flat reef top is more typical of conditions along the southeast coast of Guam. These experiments were also conducted at a much larger model scale (1:36) compared to the Seelig experiments (1:64).

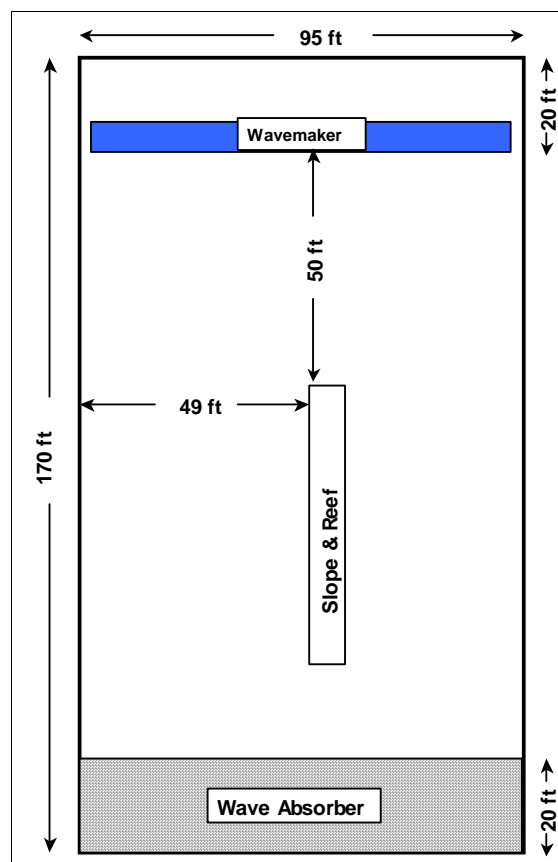


Figure 2. Basin layout for laboratory experiments of Thompson (2005).



Figure 3. Photograph of reef being built in CHL directional wave basin.

Nine wave gauges were deployed to measure the water surface elevation at different locations in the flume as shown in Figure 4. The wave gauges were installed at distances of -21.4, -21.08, -20.49, -9.13, -6.09, -4.59, -2.45, and -1.84 m from the toe of the beach. The experiments were conducted at two water levels (Elev. = 0.0 m and Elev. = +0.056 m), corresponding to still-water depths of 0.744 and 0.8 m, respectively, in the constant-depth offshore section of the flume. The still-water depth of 0.744 m corresponds to an initially dry reef top.

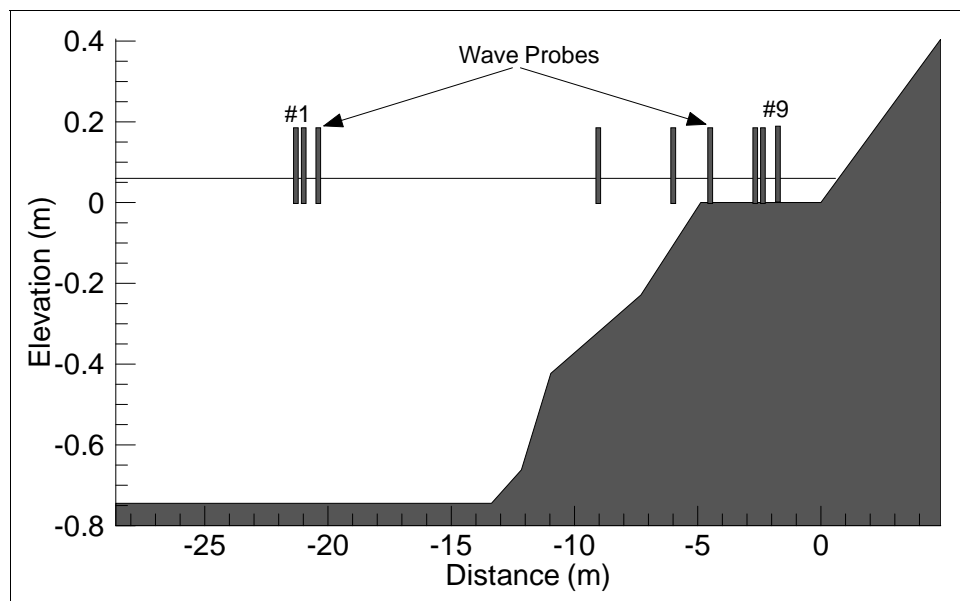


Figure 4. Cross-sectional view of laboratory setup of Thompson (2005).



## Test conditions

These experiments were conducted with 19 test conditions consisting of different combinations of significant wave height, peak period, and water level. Wave parameters at Gauge 1 (Figure 4) represent the incident waves. The test conditions consisted of two spectral peak periods (1.67 sec, 2.5 sec), two water levels (0.0 m, 0.056 m), and a range of incident wave heights (from 0.094 to 0.217 m).

Four tests were selected for model-data comparisons in this report (see Table 1). The selected test conditions represent sea states with two different peak periods and two water levels, and an incident wave height of  $H_s \approx 0.1$  m. The corresponding prototype sea states in the GUAM01 and GUAM02 tests had peak periods of 10 sec and 15 sec, respectively, wave height of approximately 3.6 m, and water level of 2 m on the reef. The GUAM12 and GUAM13 tests used equivalent conditions with an initially dry reef.

Table 1. Summary of simulated test conditions for laboratory experiments of Thompson (2005).

Test ID	Water Level (m)	$H_s$ (at Gauge 1) (m)	Target $T_p$ (sec)
GUAM01	0.056	0.094	1.67
GUAM02	0.056	0.101	2.5
GUAM12	0.0	0.104	1.67
GUAM13	0.0	0.094	2.5

## Validation of Boussinesq model

The 1-D Boussinesq model BOUSS-1D (Nwogu and Demirbilek 2001; Demirbilek et al. 2005a and 2005b) was set up to reproduce the laboratory experiments of Thompson (2005). The measured water surface elevation time series at Gauge 1 was used to derive velocity boundary conditions for the numerical model. The simulations were initially performed with  $\Delta x = 0.1$  m,  $\Delta t = 0.02$  sec, and default values for other parameters ( $l = H_s$ ,  $C_f = 30$ ,  $\delta_{min} = H_s/1,000$ ,  $C_v = 0.2$ ). The maximum water depth in the offshore section was set to 0.6 m to minimize the amount of wave energy that is truncated in the numerical model due to the deepwater (high-frequency) cutoff limit inherent in the Boussinesq equations.

The measured and calculated significant wave height variations across the reef-slope topography are compared in Figures 5 to 8 for the four selected test conditions. For the GUAM01 test, the waves shoal before breaking just offshore of the reef crest. The simulation with the default model parameters captures the overall wave height variation with slight discrepancies at Gauge 4 on the slope and Gauges 7 and 8 on the reef.

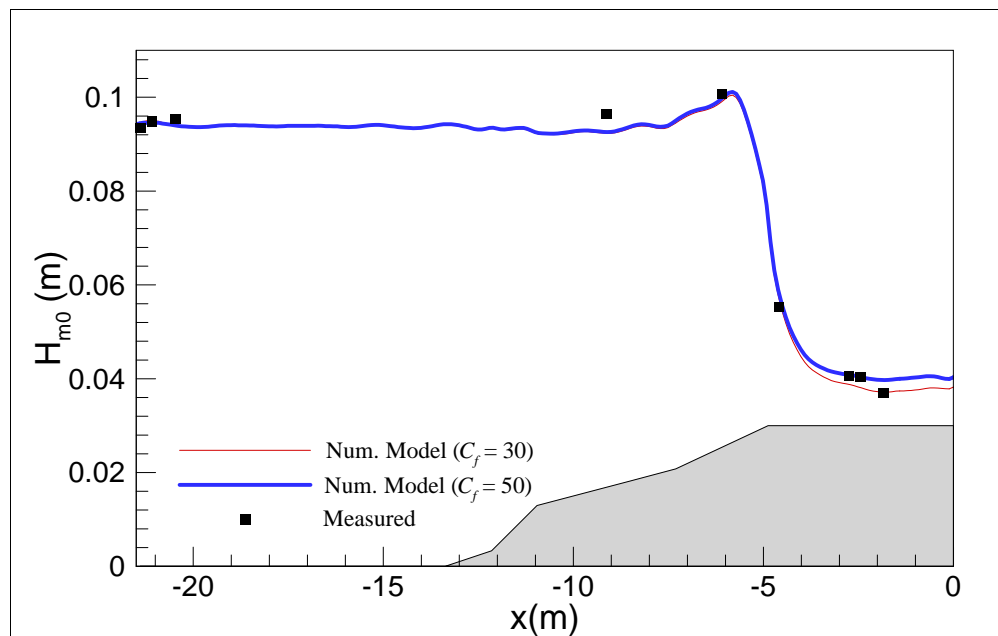


Figure 5. Measured and calculated significant wave height distribution for GUAM01 test.

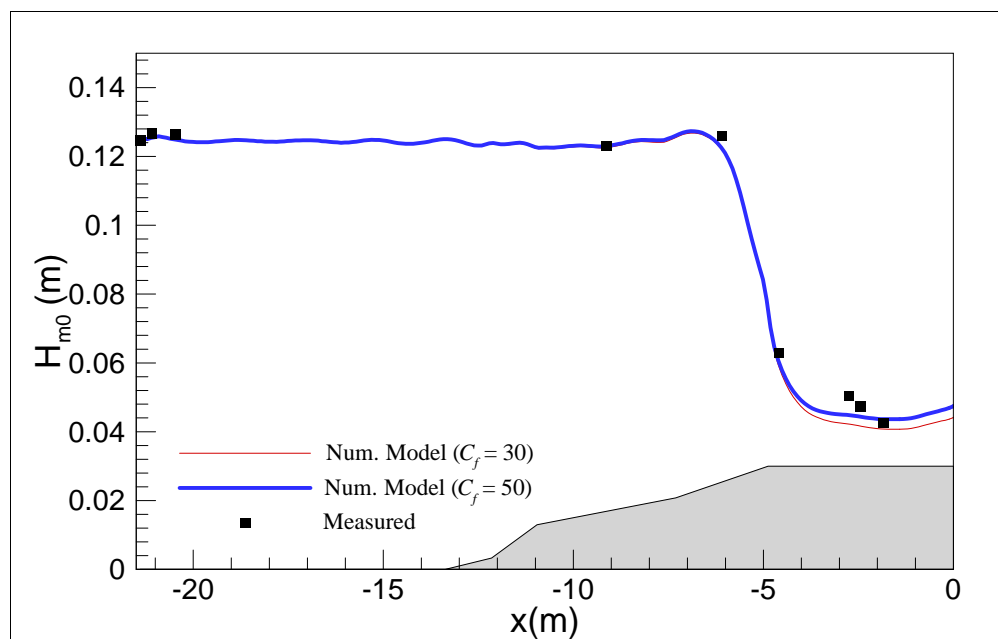


Figure 6. Measured and calculated significant wave height distribution for GUAM02 test.

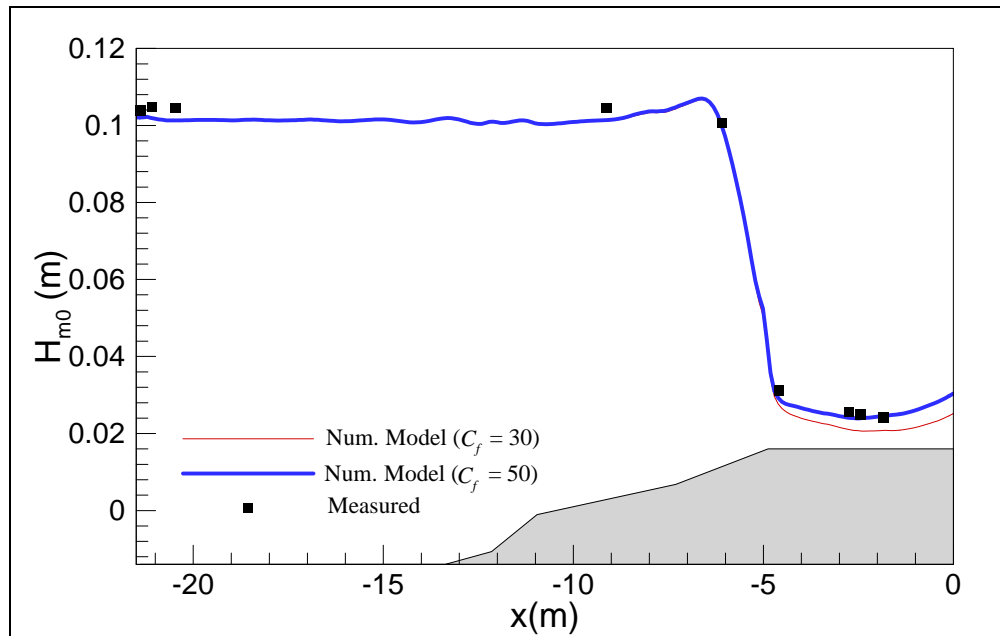


Figure 7. Measured and calculated significant wave height distribution for GUAM12 test.

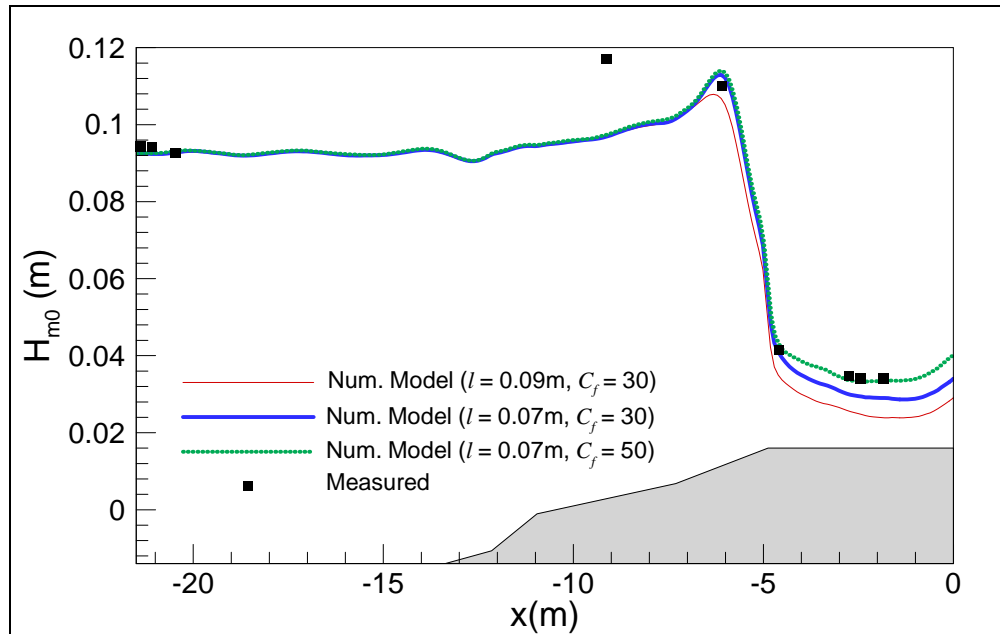


Figure 8. Measured and calculated significant wave height distribution for GUAM13 test.

Given the shallow water on the reef, we expect bottom friction to play an important role in the wave energy dissipation process. The simulation was repeated with a lower value of the friction coefficient ( $f_w = 0.004$  or  $C_f = 50$ ) as opposed to the default values:  $f_w = 0.01$  or  $C_f = 30$ . The different friction coefficient value did not alter the wave height in the deeper sections seaward of the reef, but it led to an 8 percent increase in wave height on the reef. This improved the match at Gauges 7 and 8 but

worsened the match at Gauge 9. The use of a Chezy friction coefficient  $C_f = 50$  did significantly improve the model-data match on the reef for the GUAM12 test (Figure 7).

For the GUAM13 test with longer-period waves, the model slightly underestimated the wave height at Gauge 5 just seaward of the reef crest where the waves are starting to break. Decreasing the turbulent length scale  $l$  from the default value of 0.094 m to 0.07 m improved the match at Gauge 5 but still underestimated the wave height on the reef. The best match on the reef was obtained by changing the bottom friction coefficient to  $C_f = 50$ . We note that the measured wave height at Gauge 4 was much higher than the model-predicted values (see Figure 8). The reason for this discrepancy is unclear at this time.

Plots of the significant wave height distribution give an overall view of the wave energy transformation across the reef but do not describe how the wave energy is redistributed in the frequency domain due to nonlinear wave-wave interactions. Hence, the spectral densities of the measured and predicted surface elevation time-histories were also compared. Spectral densities of the water surface elevation time-histories were obtained by Fourier transforming the data and band-averaging over 31 frequency components, resulting in 62 deg of freedom and a frequency resolution of 0.056 Hz. The record length of the analyzed segment was 820 sec from  $t = 50$  sec to  $t = 870$  sec.

Figures 9 to 12 show a comparison of the measured and calculated wave spectra at Gauges 3, 5, 7, and 9 for the GUAM01, GUAM02, GUAM12, and GUAM13 tests for simulations with the best-fit bottom friction coefficient and turbulent length scale. The corresponding time series are plotted in Figures 13 to 16. The wave spectra on the reef (Gauges 7 and 9) consist entirely of low-frequency motions with the wave energy at the incident wave frequencies completely dissipated and/or transferred by nonlinear interactions. The Boussinesq model is able to reproduce the nonlinear energy transfer to the low-frequency modes although there are some differences between the measured and predicted wave spectra. At Gauge 5 just offshore of the reef crest, there is a distinct low-frequency peak ( $f \approx 0.064$  Hz) in the measured spectra that is underpredicted by the numerical model. This peak is also present in the measured spectra at Gauges 4 and 6 (not shown) but not at the other gauge locations.

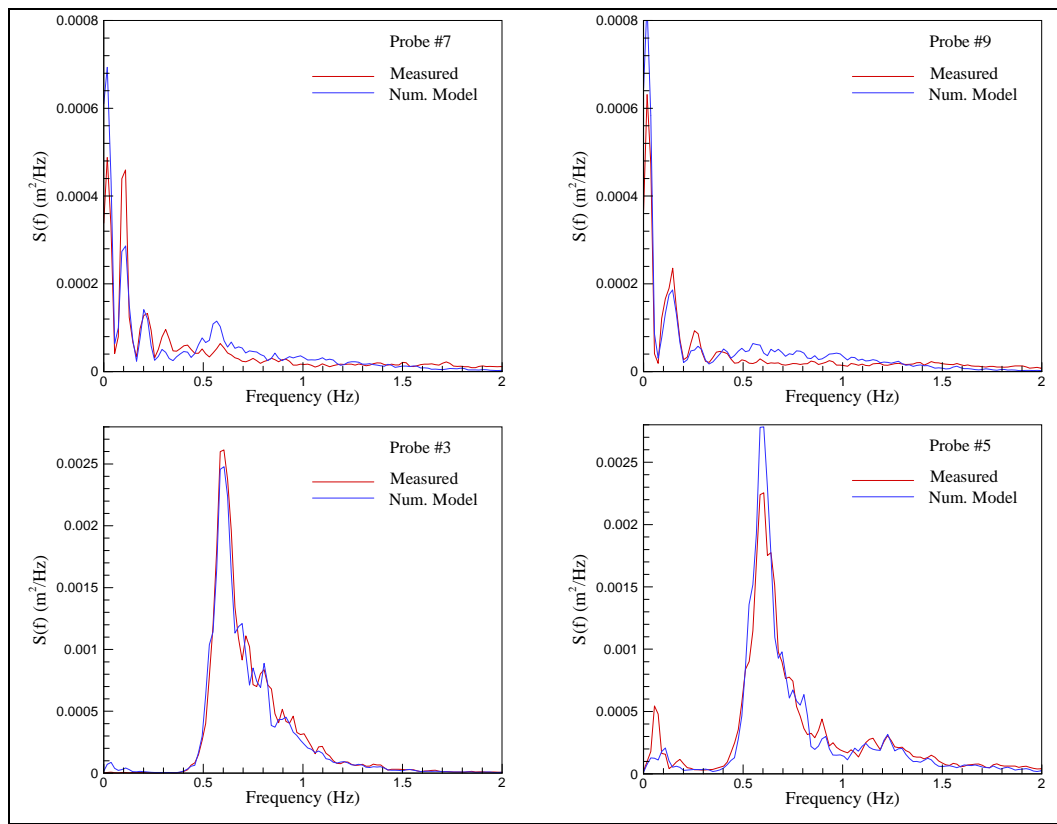


Figure 9. Measured and calculated wave spectra for GUAM01 test.

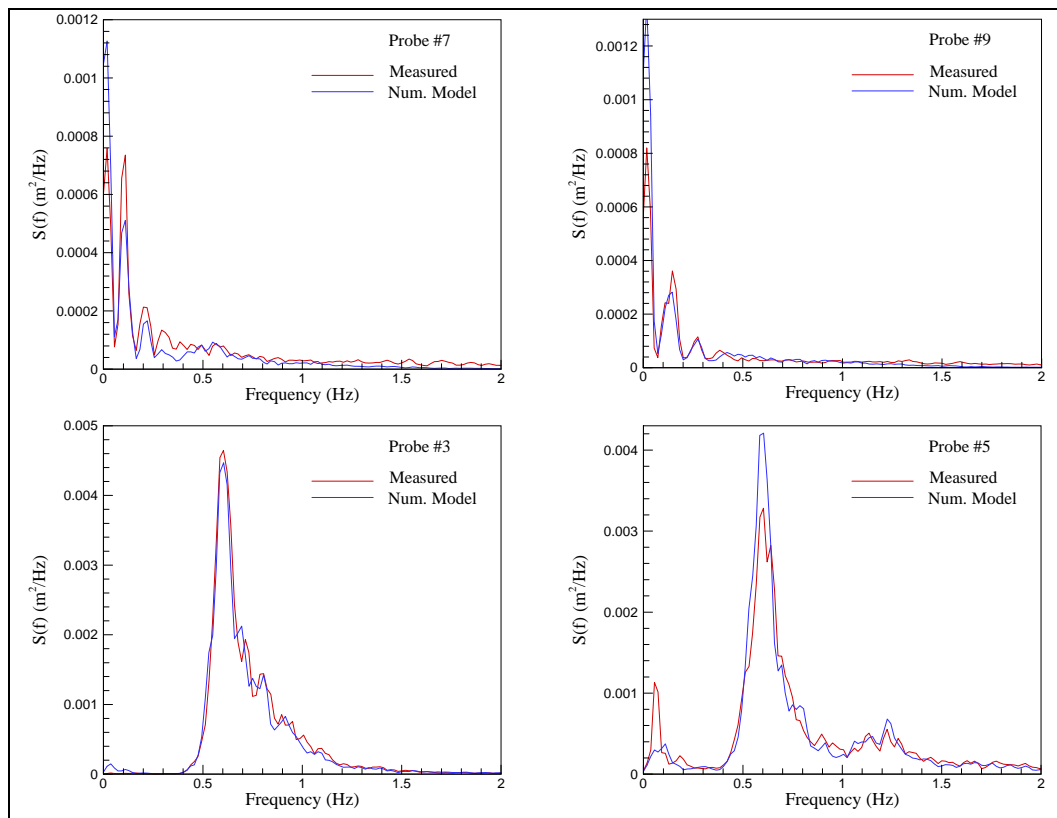


Figure 10. Measured and calculated wave spectra for GUAM02 test.

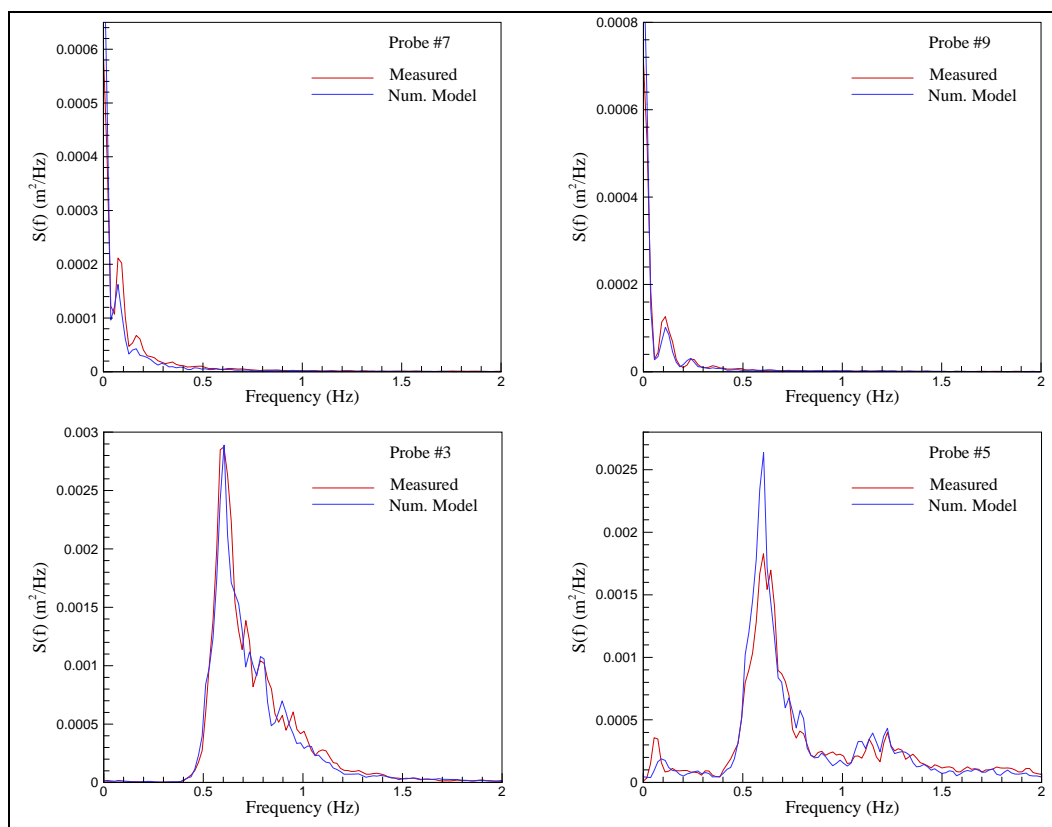


Figure 11. Measured and calculated wave spectra for GUAM12 test.

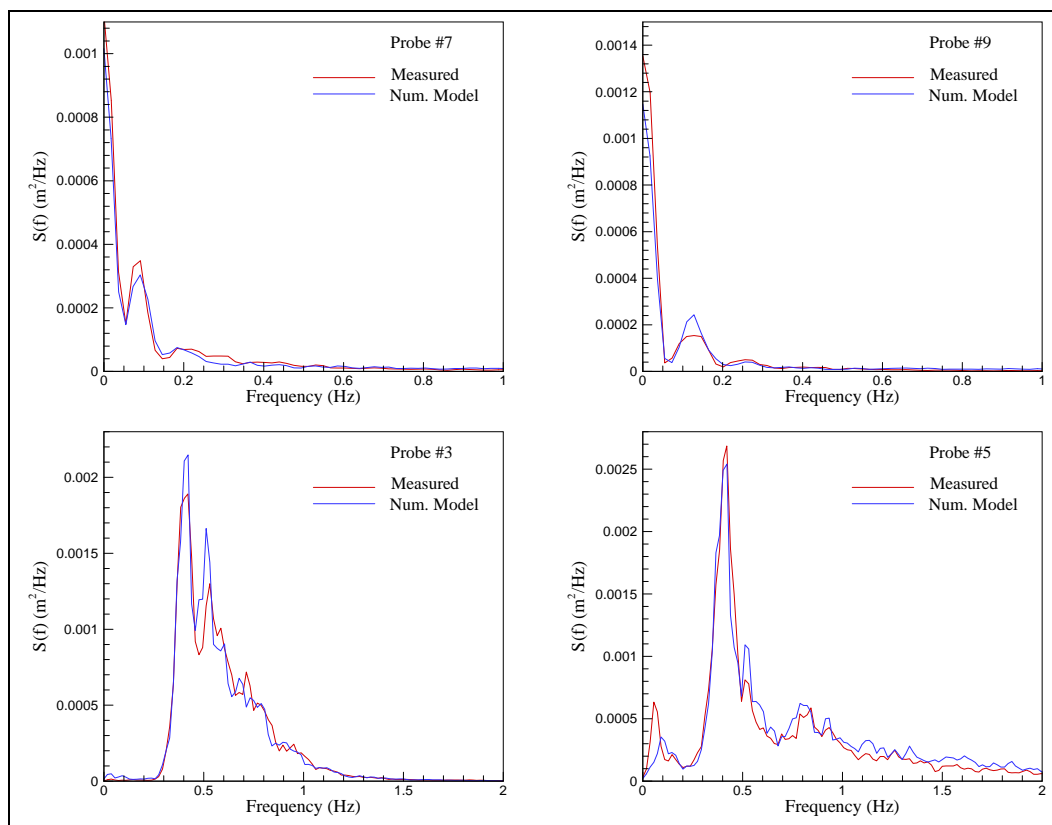


Figure 12. Measured and calculated wave spectra for GUAM13 test.

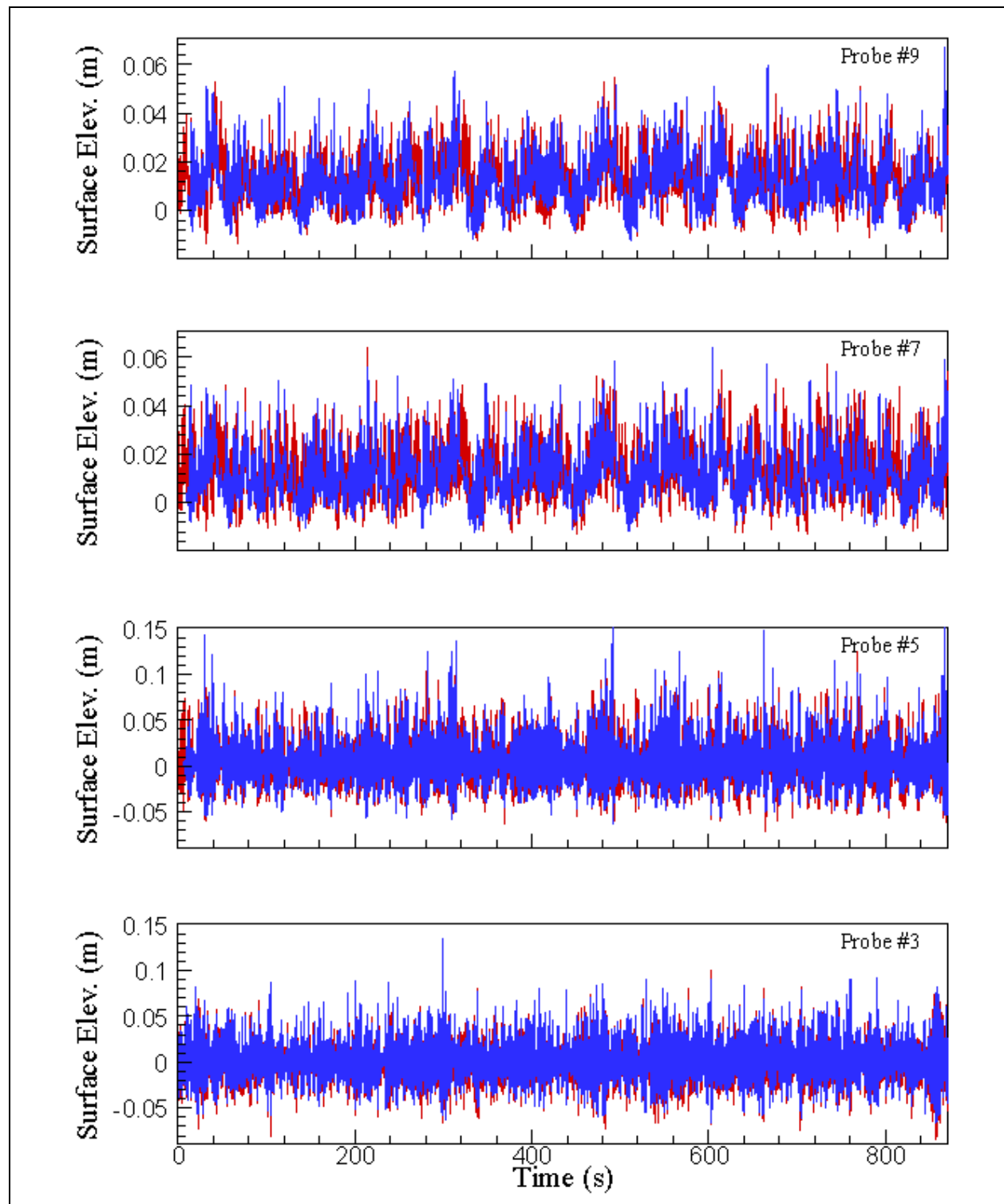


Figure 13. Measured and calculated surface elevation time series for GUAM01 test; measured (red), numerical model output (blue).

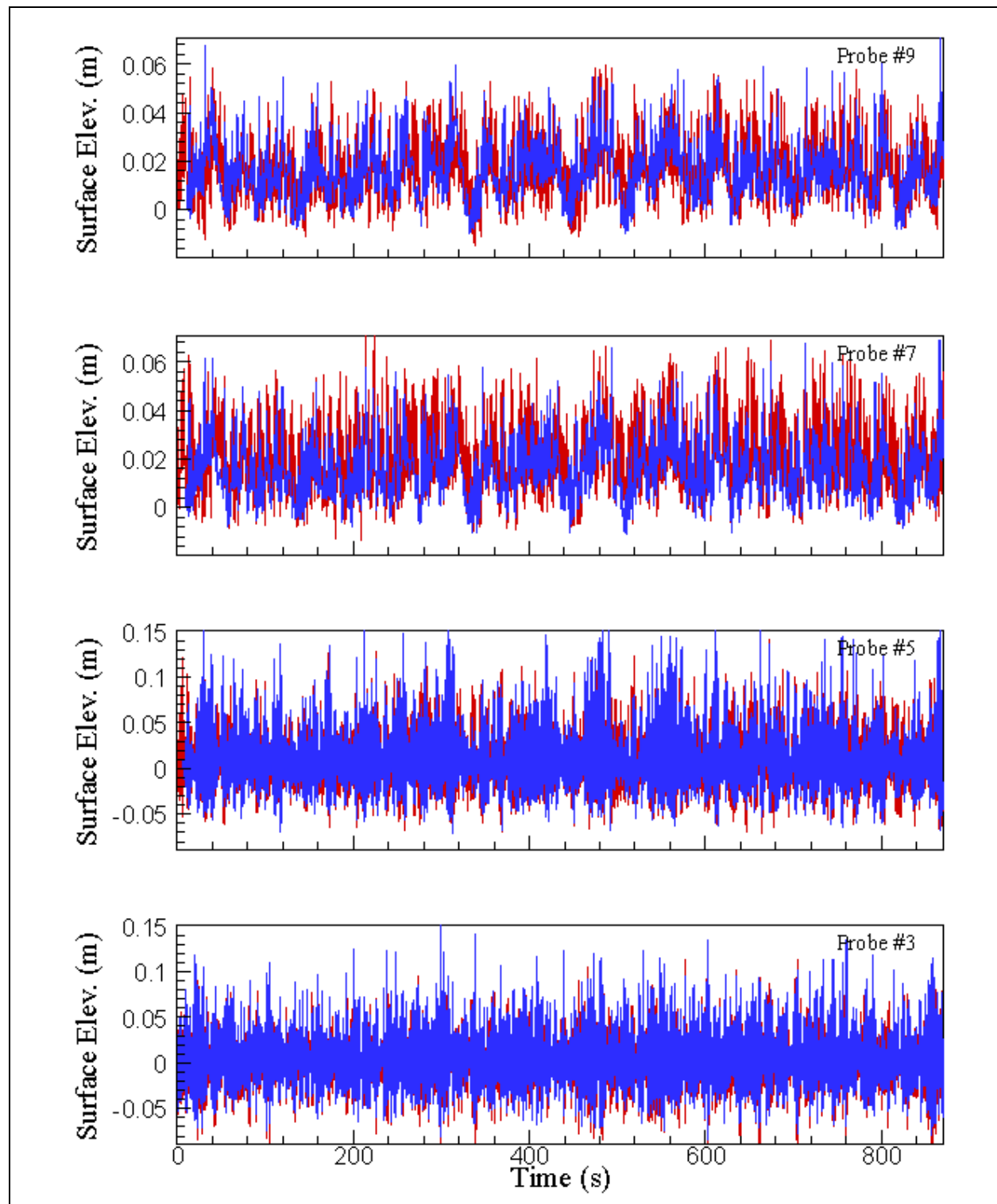


Figure 14. Measured and calculated surface elevation time series for GUAM02 test; measured (red), numerical model output (blue).



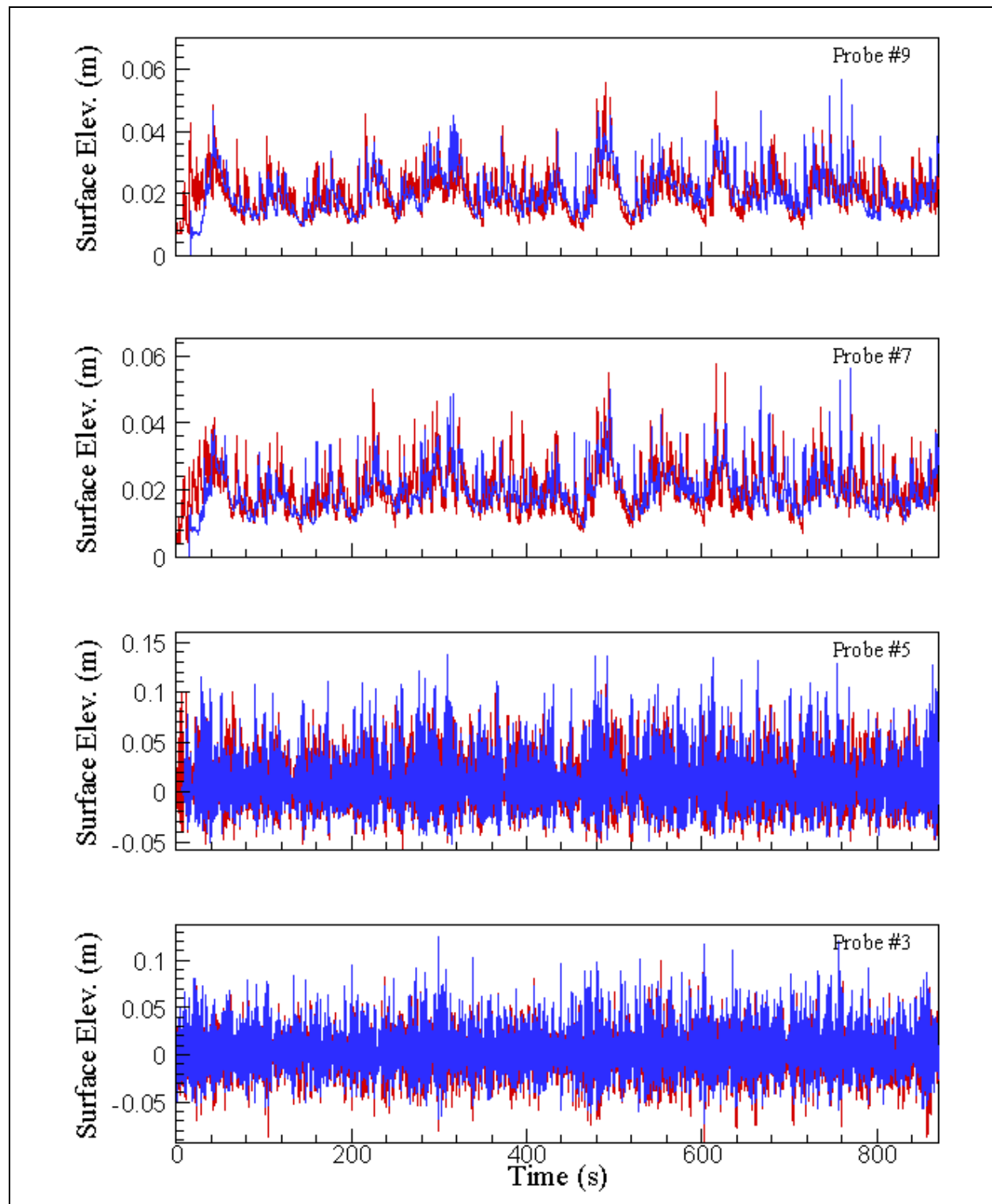


Figure 15. Measured and calculated surface elevation time series for GUAM12 test; measured (red), numerical model output (blue).

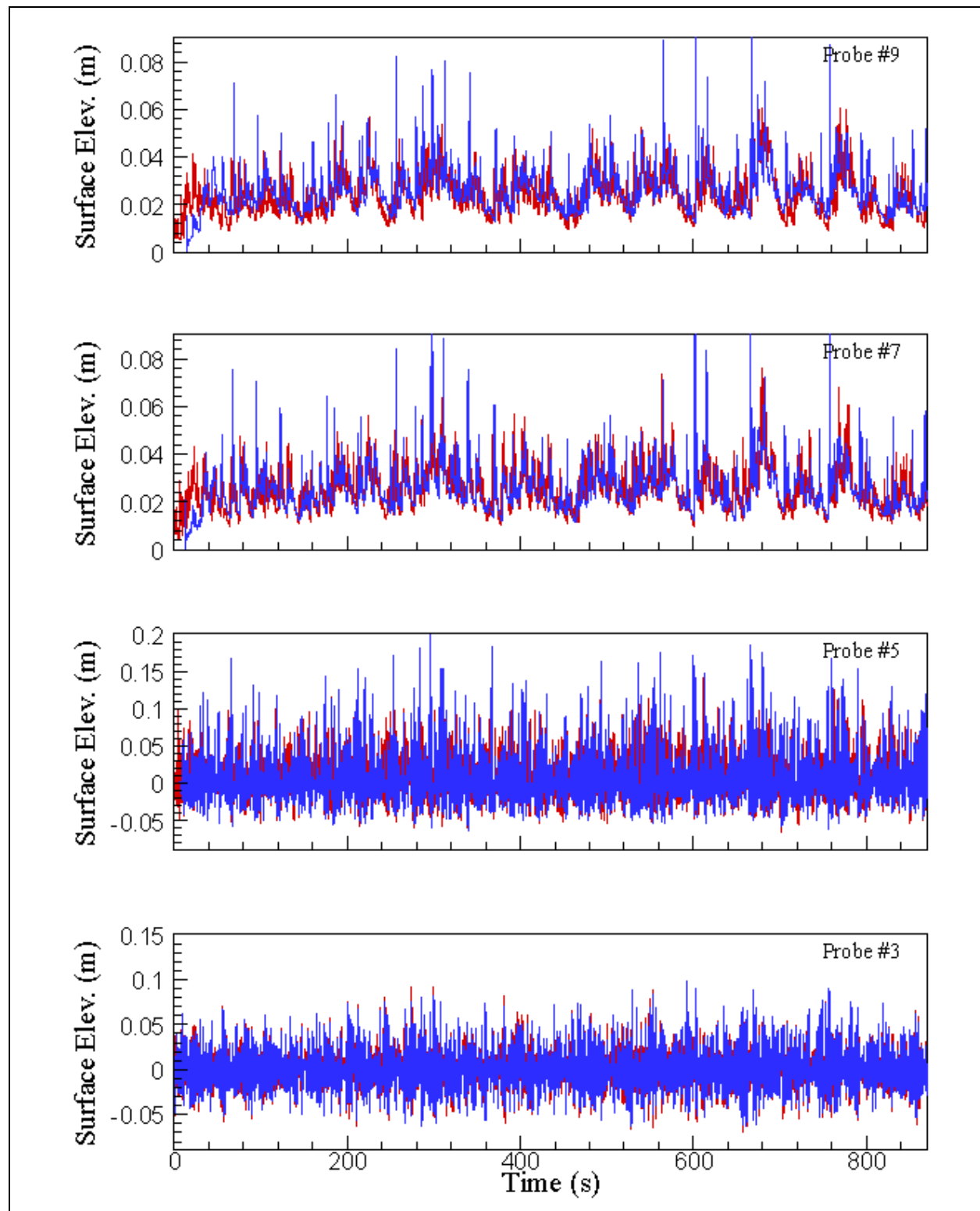


Figure 16. Measured and calculated surface elevation time series for GUAM13 test; measured (red), numerical model output (blue).

We suspect that it might be a local standing wave due to the steep slope on the reef face which cannot be simulated in the Boussinesq model. The wave spectra on the reef flat (Gauges 7 and 9) had several distinct low-frequency oscillation peaks. The numerical model tended to overestimate the lowest peak and underestimate the second peak. Overall, comparisons are quite good.

The water surface elevation time series comparison plots shown in Figures 13 to 16 provide further evidence that the Boussinesq model is capable of reproducing the overall trends in the data including the phasing of the low-frequency motions on the reef. The low-frequency motions are more visible for the lower water level tests (Figure 15 for GUAM12 and Figure 16 for GUAM13 tests) where the flat reef section was initially dry. A closeup view of the measured and predicted surface elevation time series at Gauge 9 is shown in Figure 17 for the GUAM12 test, showing a remarkable agreement between measurements and calculations. The numerical model describes the nonlinear steepening and highly asymmetric profile of post-breaking waves on the shallow reef. There are some discrepancies in these detailed time-domain characteristics. However, given that the wave breaking process is parameterized in the Boussinesq model, one cannot expect the model to capture fine details of post-breaking waves on a wave-by-wave basis. The adopted breaking criterion, for example, is based on the ratio of the water particle velocity at the crest to the phase velocity. The phase velocity is computed using linear theory and the average zero-crossing period of the incident wave train. This might lead to an earlier or later initiation of breaking for individual waves, depending on the individual wave frequencies and amplitudes.

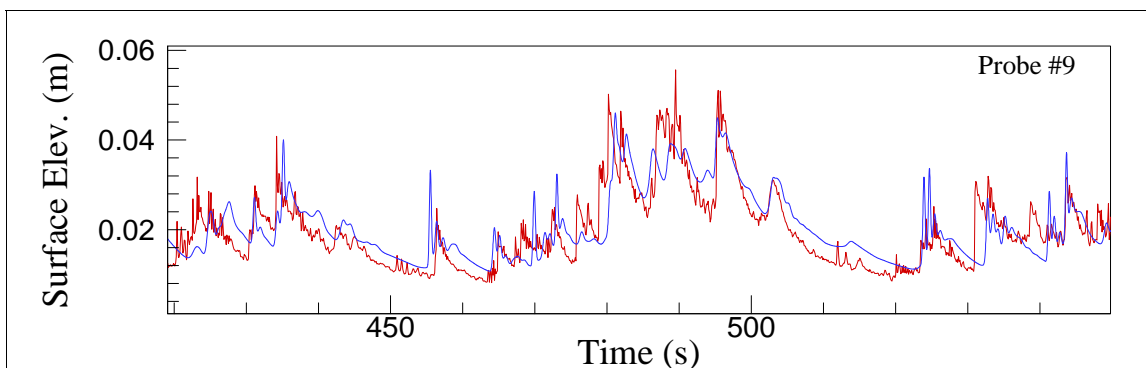


Figure 17. Closeup view of measured and calculated surface elevation time series at Gauge 9 for GUAM12 test; measured (red), numerical model output (blue).

Capacitance-wire wave gauges were deployed to measure runup height during these experiments, and the output from those could not be directly compared to the numerical model predictions because of jumps in the data. Runup peak elevations were alternatively obtained by digitizing video recordings of the runup process. The maximum runup heights are summarized in Table 2. In general, the magnitudes of the calculated runup peaks are similar to the measured peaks with differences of the order of 10 percent.

Table 2. Summary of measured and calculated maximum runup heights.

Test ID	Maximum Runup Height (m)		% Difference
	Measured	Calculated	
GUAM01	0.13	0.14	8
GUAM02	0.18	0.16	11
GUAM12	0.08	0.07	13
GUAM13	0.13	0.13	0

## 4 Laboratory Experiments at University of Michigan

### Description of experiments

A smaller scale (1:80) model of a 2-D fringing reef was built in the 35-m-long by 0.7-m-wide wind-wave flume at the University of Michigan (UM). The first report in this series (Demirbilek et al. 2007) provides information about the UM study. The cross-sectional profile of the reef-beach system is shown in Figure 18. It consists of a 1:12 beach preceded by a 4.8-m-wide reef flat and a composite slope reef face. The cross section of the reef face is identical to the one used in the hydraulic model tests performed by Seelig (1983) and Thompson (2005). However, a fringing reef profile with a flat reef top was used in these experiments instead of the barrier reef profile with a lagoon in Seelig (1983). The reef top used in the UM experiments was also wider (~1,260-ft-wide prototype scale) than that used in the Thompson experiments (~575-ft-wide prototype scale).

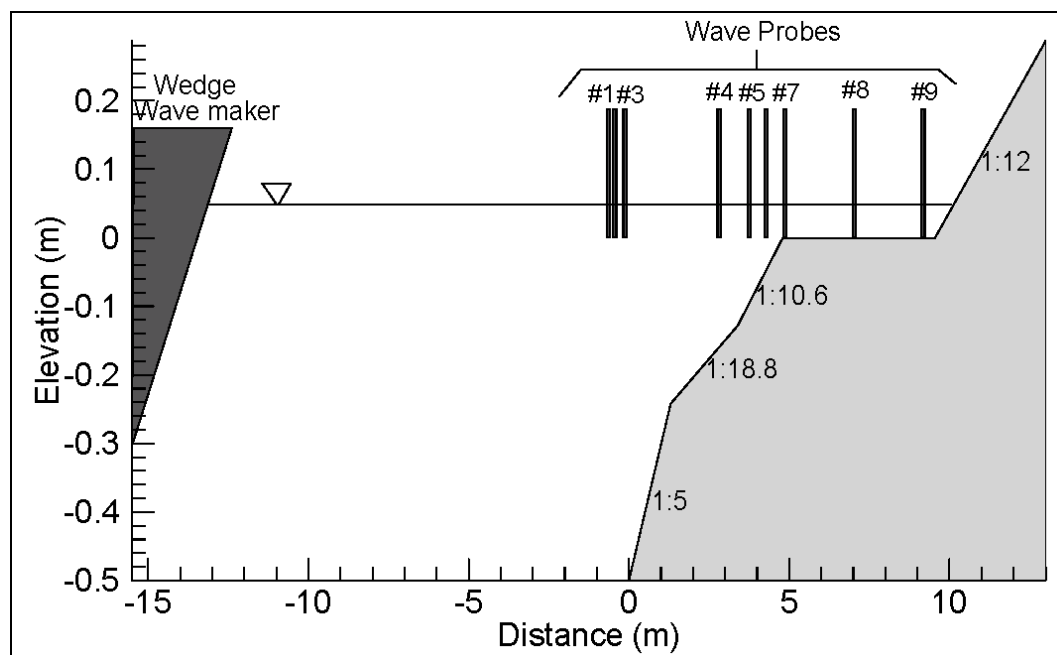


Figure 18. Experimental setup for UM fringing reef experiments.

The reef surface was built using polyvinyl chloride (PVC) plastic, a relatively smooth and impervious material. Although most natural coral reefs are composed of hard calcium carbonate skeletal material and covered by a wide variety of benthic organisms, it is difficult to reproduce the hydraulic roughness and porosity of natural coral reefs in a laboratory setting. The experiments were designed to provide insight into the physics of non-linear wave transformation and runup on fringing reef profiles with known bottom friction properties as opposed to exact model scale reproduction of hydrodynamic processes over natural coral reefs.

A computer-controlled plunger-type wave maker generated irregular waves in the tank. The toe of the reef slope was located at a distance of approximately 15.5 m from the wave maker. Due to concern about the influence of re-reflected waves from the wave maker, three capacitance-wire wave gauges were installed in the constant-depth section of the flume to quantify the amount of wave reflection. Six additional capacitance-wire wave gauges measured the wave conditions across the reef profile as shown in Figure 18.

Wave gauge locations relative to the toe of the reef slope are provided in Table 3. The wave gauges over the reef flat were designed to provide accurate measurements of wave setup over the reef flat. The bottom ends of the gauges were inserted into holes drilled into the reef surface, allowing the gauges to record water level changes over the reef flat from an initially dry reef surface. Wave runup on the beach was recorded by a 1-m-long capacitance-wire runup gauge installed on the beach face.

**Table 3. Wave gauge coordinates.**

Sensor	X (cm)
Gauge 1	-0.69
Gauge 2	-0.49
Gauge 3	-0.18
Gauge 4	2.75
Gauge 5	3.68
Gauge 6	4.23
Gauge 7	4.84
Gauge 8	6.99
Gauge 9	9.13

## Test conditions

Tests were run for a wide variety of irregular sea states, summarized in Table 4. The tests consisted of irregular sea states with significant wave heights ranging from 3 to 8.5 cm, spectral peak periods from 1 to 2.5 sec, water levels  $h_r$  of 0 to 5.1 cm above the reef flat (or 50 to 55 cm above the flume floor), and no wind. The 50-cm water depth ( $h_r = 0$  cm) corresponds to an initially dry reef flat, similar to conditions when a reef flat is exposed at low tide. Time-histories of the water surface elevation were synthesized from JONSWAP spectral shapes with peak enhancement factor  $\gamma = 3.3$  using the random phase method. Linear theory was used to convert the water surface elevation to control signals for the wave maker.

The gauges were sampled for 15 min at 20 Hz. The gauges were zeroed before each test to minimize drift. Data collection was initiated shortly after the wave maker was started from initially calm water.

Table 4. Summary of test conditions.

Test ID	$H_s$ (cm)	$T_p$ (sec)	$h_r$ (cm)
Test-20	6.1	1.25	5.1
Test-17	7.8	1.50	5.1
Test-21	8.2	1.75	5.1
Test-18	8.5	2.00	5.1
Test-46	5.9	1.25	3.1
Test-48	7.5	1.50	3.1
Test-57	7.7	1.75	3.1
Test-58	8.5	2.00	3.1
Test-27	5.5	1.25	1.6
Test-29	7.1	1.50	1.6
Test-30	7.6	1.75	1.6
Test-31	8.5	2.00	1.6
Test-36	6.8	1.50	0.0
Test-37	7.6	1.75	0.0
Test-38	8.4	2.00	0.0

Given the steep slope of the reef face, most the waves broke violently on the reef face in a plunging manner with a big slash-up as shown in Figure 19. This photograph was taken in the vicinity of the Gauge 6 (see Figure 18), located just offshore of the reef crest. After breaking, the waves reformed as bores and propagated across the reef flats to the beach. Several types of bores were observed during the tests ranging from undular bores (without visible breaking at its front) to fully turbulent bores with a turbulent roller region at its front. These bores evolved significantly as they traveled over the flat reef section.



Figure 19. Plunging breaking waves for Test-18 near the reef crest.

## Validation of Boussinesq model

Based on the observed violent plunging nature of the wave breaking in these laboratory experiments, we initially investigated the sensitivity of the Boussinesq model predictions to the parameterization of the wave breaking process. The numerical model was initially run for one of the test conditions (Test-29) with  $H_s = 7.1$  cm,  $T_p = 1.5$  sec, and  $h_r = 1.6$  cm. The measured water surface elevation time series at Gauge 1 was used to derive velocity boundary conditions for the numerical model. The simulations were performed with  $\Delta x = 5$  cm,  $\Delta t = 0.01$  sec, and default values for other parameters ( $l = H_s$ ,  $C_f = 30$ ,  $\delta_{min} = H_s/1000$ ,  $C_v = 0.2$ ). Three wave breaking formulations were investigated (refer to Chapter 2): the spilling breaking formulation (SBF), the plunging wave breaking formulation (PBF-1),



and a modified plunging breaking formulation with the wave breaking factor in Equation 15 advected with the phase velocity instead of the orbital velocity at the wave crest (PBF-2).

The measured and calculated significant wave height and mean water level variation across the reef are compared in Figure 20 for the different wave breaking formulations. Although both the spilling breaking formulation (SBF) currently implemented in BOUSS-2D and the new plunging breaking formulation (PBF-1) predicted fairly similar post-breaking wave heights, the SBF formulation underestimated the wave setup over the reef flat. The PBF-2 formulation, in which the breaking factor is advected with the wave celerity, overpredicts the wave height near the break point and thus produces a higher setup over the reef. The comparisons show how sensitive the wave setup over the reef is to the spatial distribution of the eddy viscosity. We note that the decrease in the mean water level offshore of the reef in the measurements was due to the use of a closed laboratory flume for the experiments with no replenishment of water pumped onto the reef.

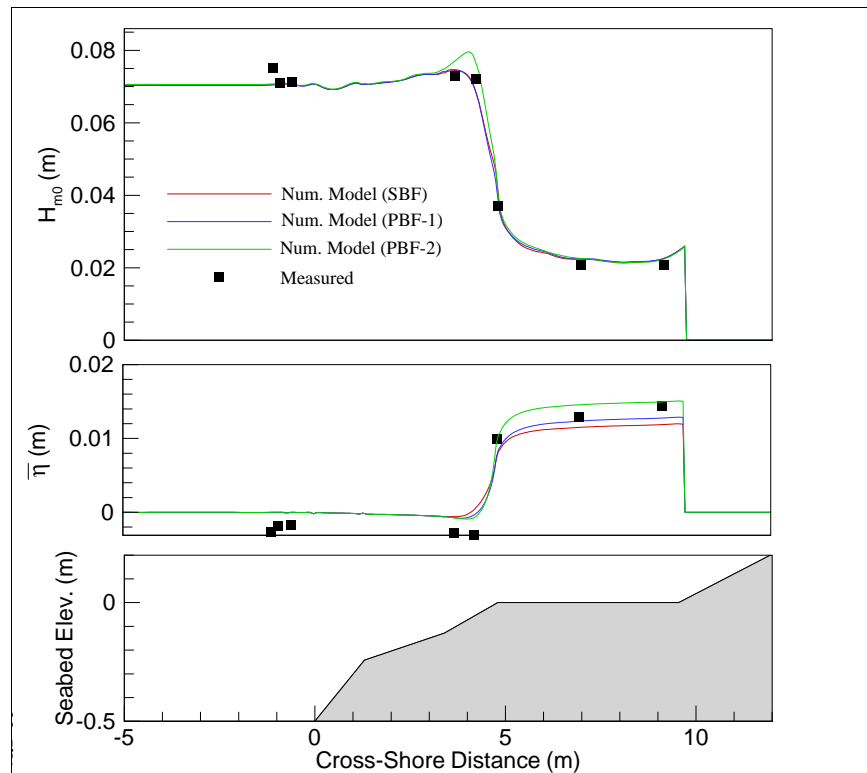


Figure 20. Measured and predicted significant wave height and mean water level variation for different wave breaking formulations (Test-29).

Sensitivity of the model predictions to the parameterized bottom friction coefficient is investigated next. For this purpose, four tests were selected with  $H_s \approx 0.07$  m,  $T_p = 1.5$  sec, and different water levels  $h_r = 0.0$  cm (Test-36),  $h_r = 1.6$  cm (Test-29),  $h_r = 3.1$  cm (Test-48), and  $h_r = 5.1$  m (Test-17). Figures 21 to 24 show a plot of the measured and predicted significant wave height and mean water level variations across the reef for two friction coefficients ( $C_f = 30$  and  $C_f = 24$ ). The use of  $C_f = 24$  led to good matches of the post-breaking wave height for the lower water level cases ( $h_r = 0.0$  cm and 1.6 cm) but not the higher water cases ( $h_r = 3.1$  cm and 5.1 cm). This suggests the need to use a depth-dependent value of the bottom friction coefficient for waves propagating over shallow reefs. This conclusion is consistent with parameterization of the friction factor in Equation 17 for smooth impermeable slopes where the bottom friction coefficient depends on the inverse of the Reynolds number of the flow. Over shallow reef flats, larger water depths ( $h_r$ ) support larger wave heights which produce larger bottom velocities and larger Reynolds numbers. Therefore,  $C_f$  should be larger for higher water levels according to Equation 17. One simple way to incorporate a depth-dependent bottom friction coefficient in the Boussinesq model is to use the Manning formulation where the friction coefficient varies as the sixth root of the water depth.

Spectral densities of the water surface elevation time-histories were obtained by Fourier transforming an 800-sec segment of the measured/predicted time series from  $t = 100$  sec to  $t = 900$  sec. The Fourier amplitudes were then band-averaged over 30 frequency components, resulting in 60 spectral degrees of freedom (DOF) at a frequency resolution of 0.02 Hz. Figures 25 to 28 show a plot of the measured and predicted wave spectra at an offshore gauge (Gauge 3), a reef-face gauge (Gauge 6), the mid-reef flat gauge (Gauge 8), and the nearshore gauge (Gauge 9) for Test-36 ( $h_r = 0.0$  cm), Test-29 ( $h_r = 1.6$  cm), Test-48 ( $h_r = 3.1$  cm), and Test-17 ( $h_r = 5.1$  cm), respectively. The corresponding time-series are plotted in Figures 29 to 32.

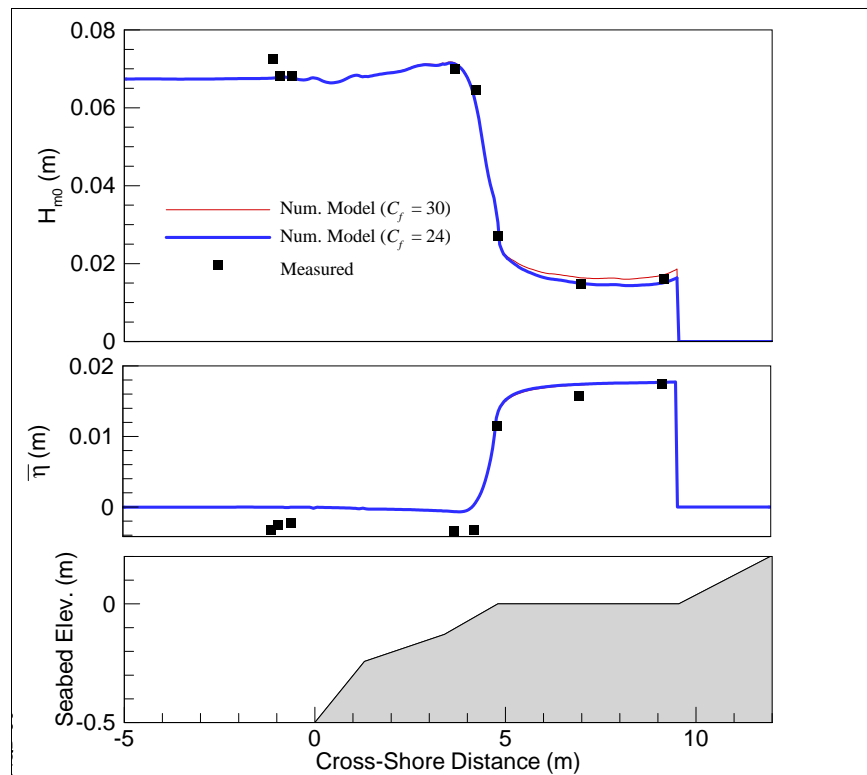


Figure 21. Measured and predicted significant wave height and mean water level variation for Test-36 ( $H_s = 0.07$  m,  $T_p = 1.5$  sec,  $h_r = 0.0$  cm).

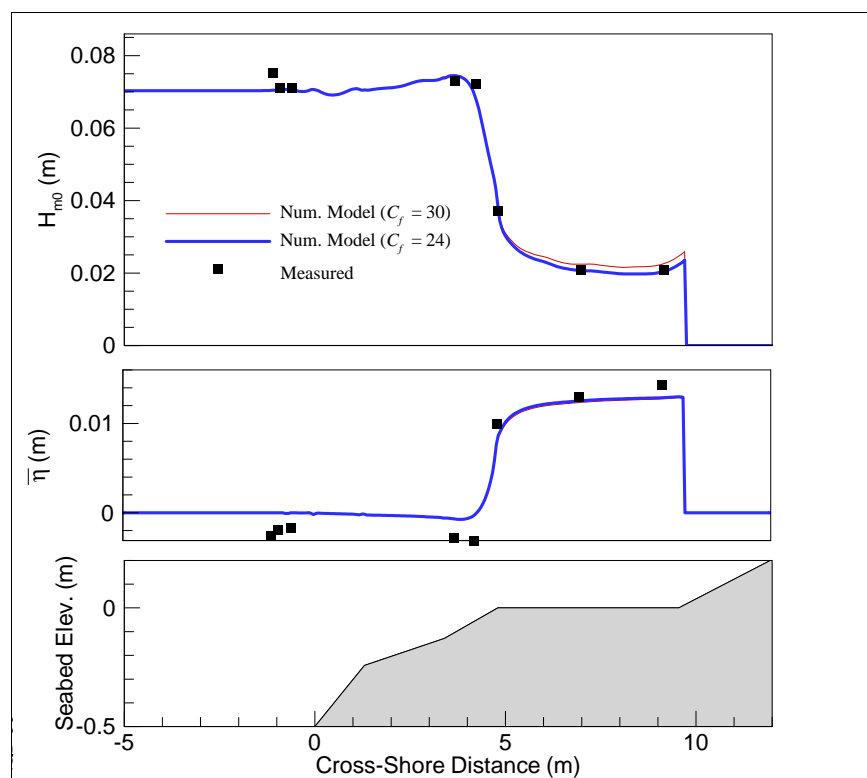


Figure 22. Measured and predicted significant wave height and mean water level variation for Test-29 ( $H_s = 0.07$  m,  $T_p = 1.5$  sec,  $h_r = 1.6$  cm).

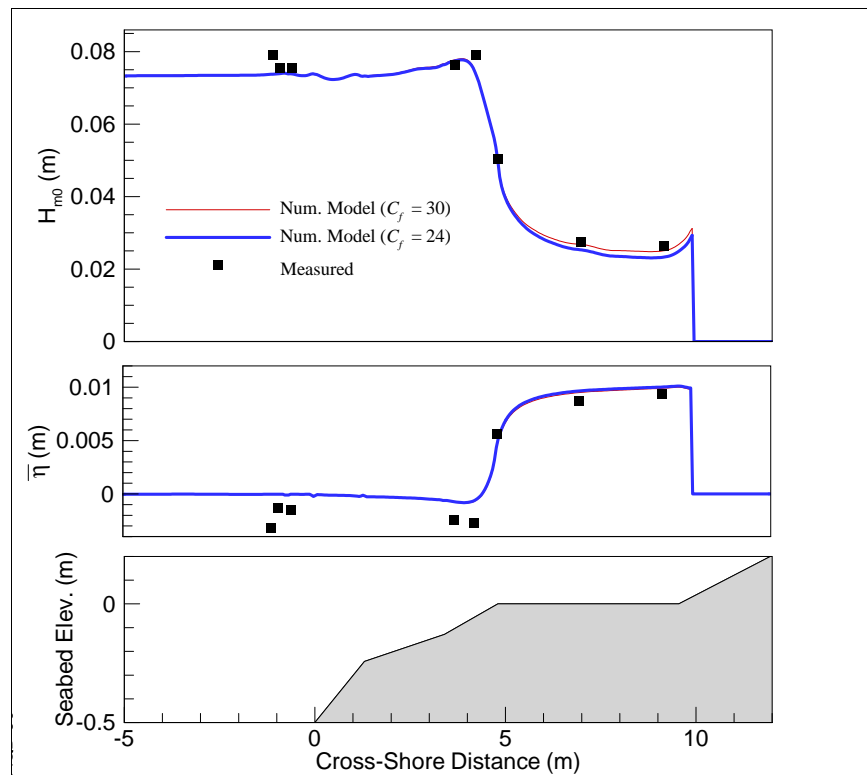


Figure 23. Measured and predicted significant wave height and mean water level variation for Test-48 ( $H_s = 0.075$  m,  $T_p = 1.5$  sec,  $h_r = 3.1$  cm).

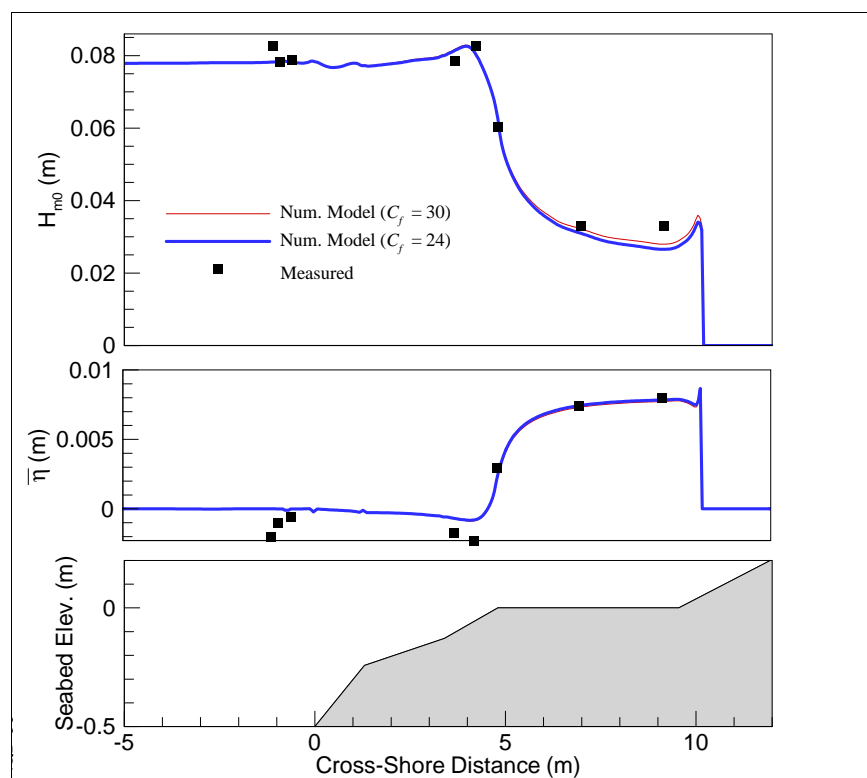


Figure 24. Measured and predicted significant wave height and mean water level variation for Test-17 ( $H_s = 0.08$  m,  $T_p = 1.5$  sec,  $h_r = 5.1$  cm).

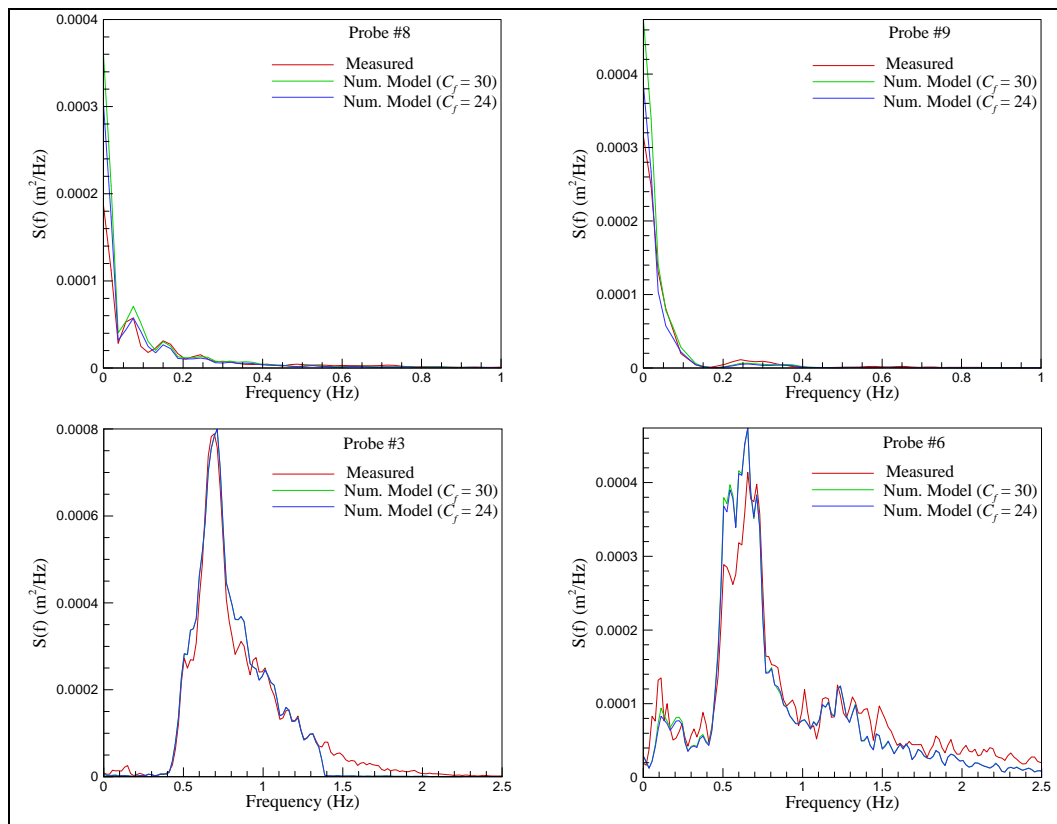


Figure 25. Measured and predicted wave spectra for Test-36.

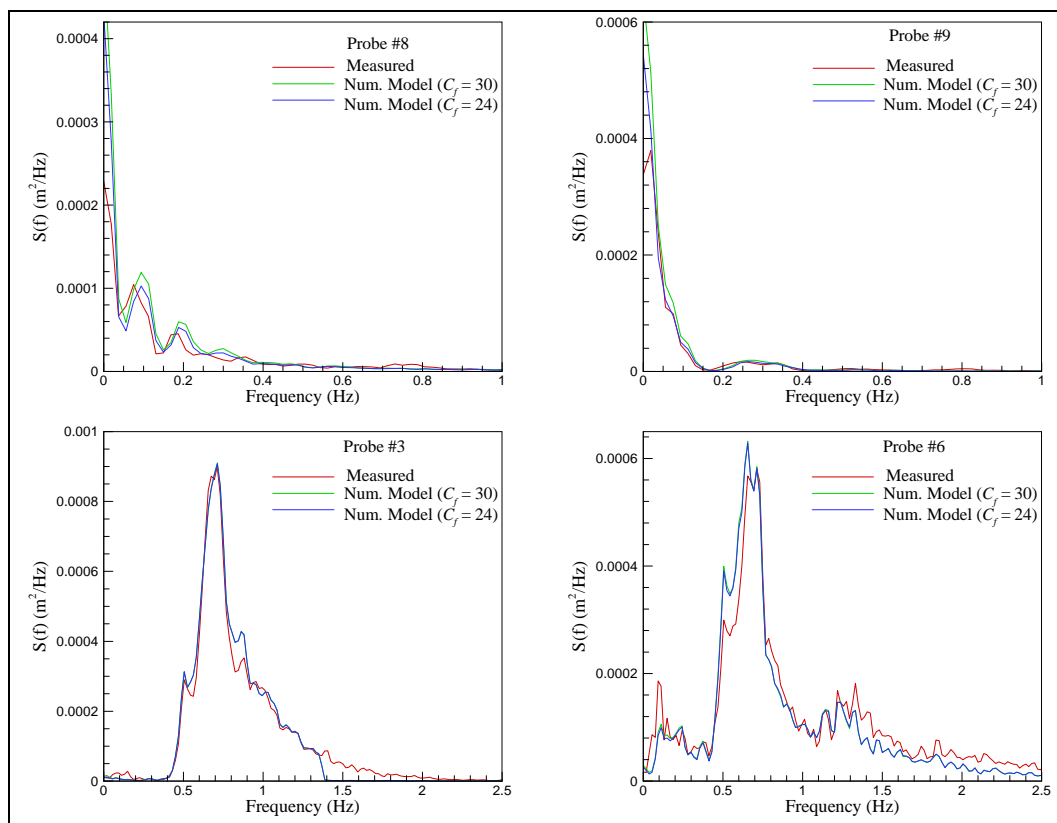


Figure 26. Measured and predicted wave spectra for Test-29.

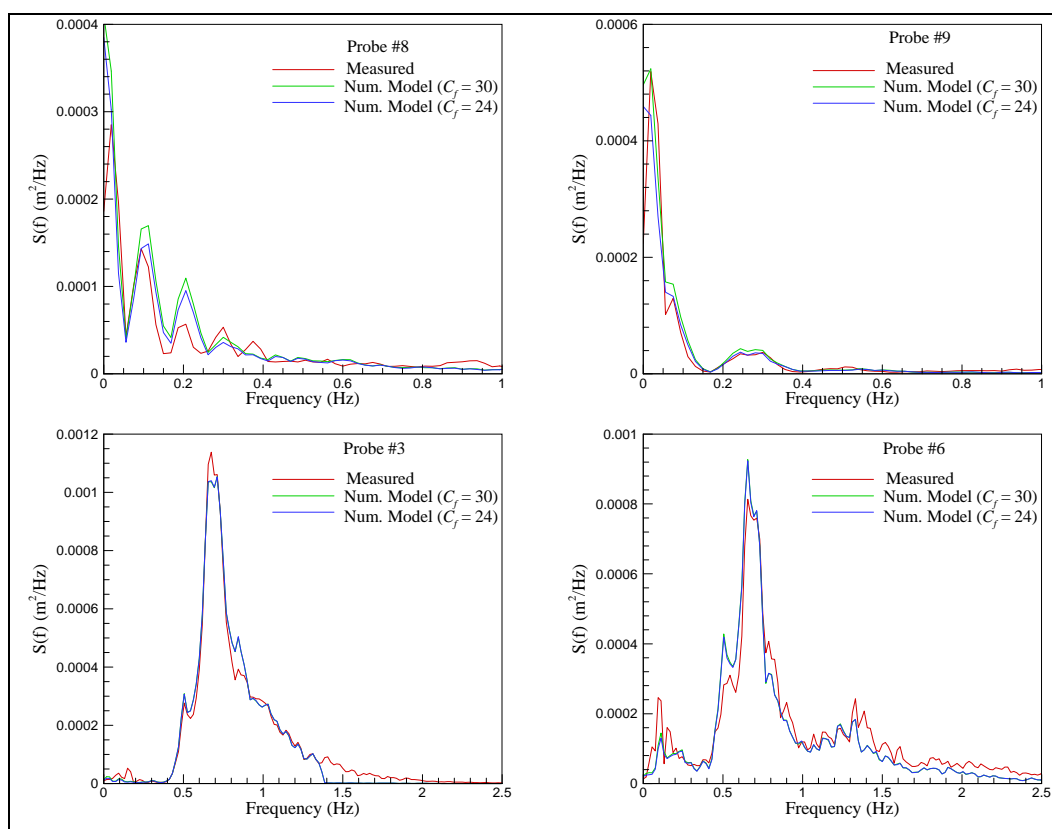


Figure 27. Measured and predicted wave spectra for Test-48.

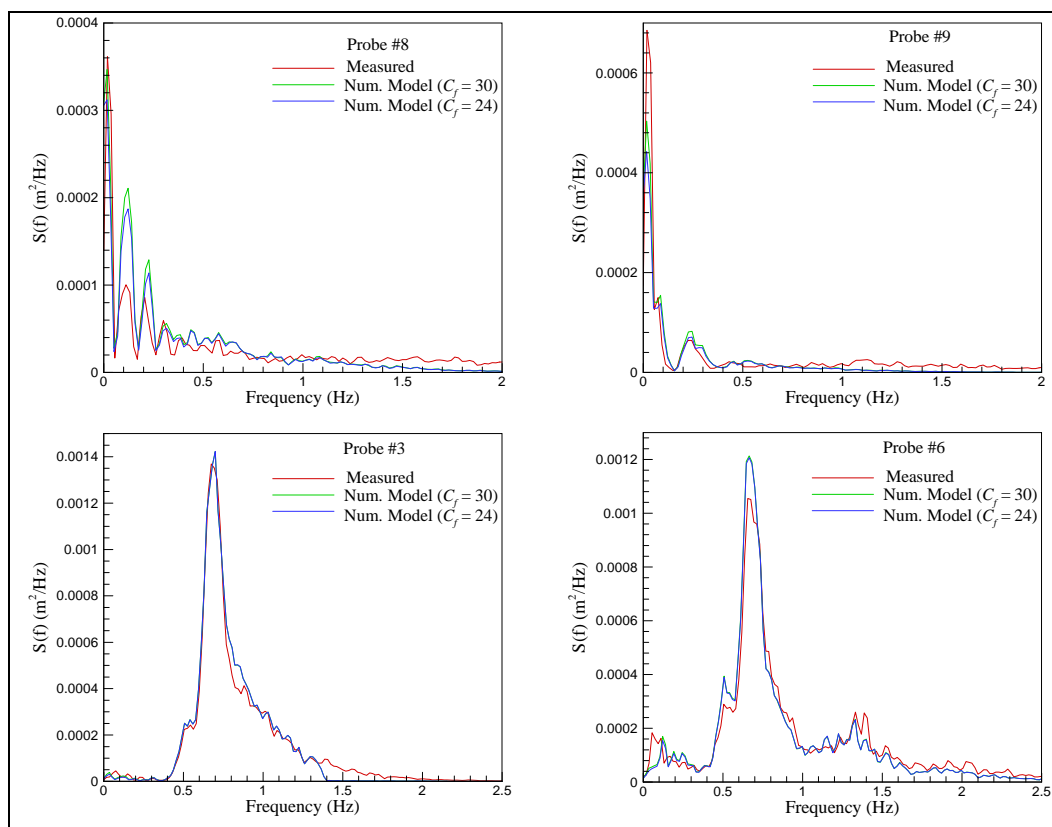


Figure 28. Measured and predicted wave spectra for Test-17.

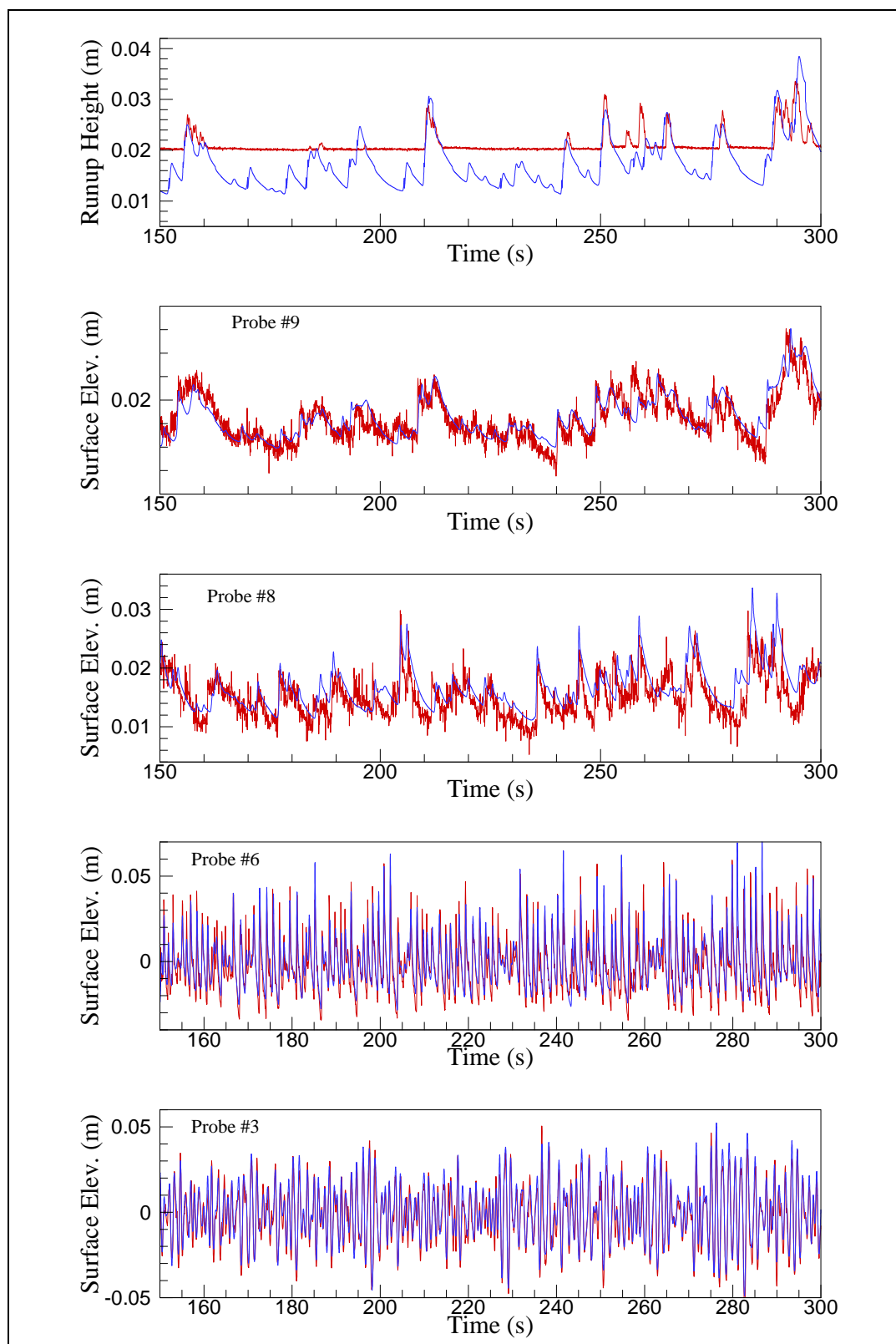


Figure 29. Measured and predicted surface elevation time series for Test-36; measured (red), numerical model prediction (blue).

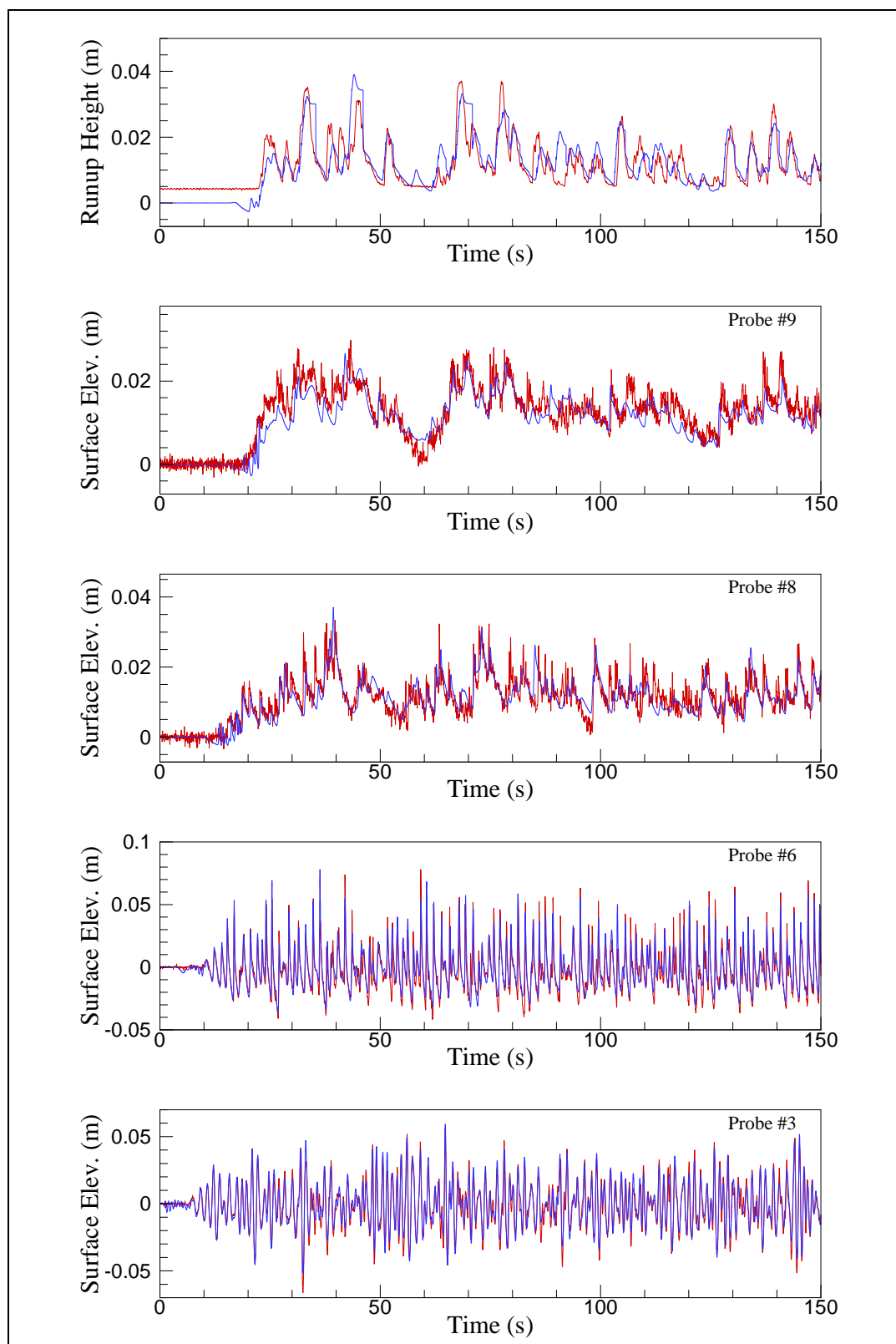


Figure 30. Measured and predicted surface elevation time series for Test-29; measured (red), numerical model prediction (blue).



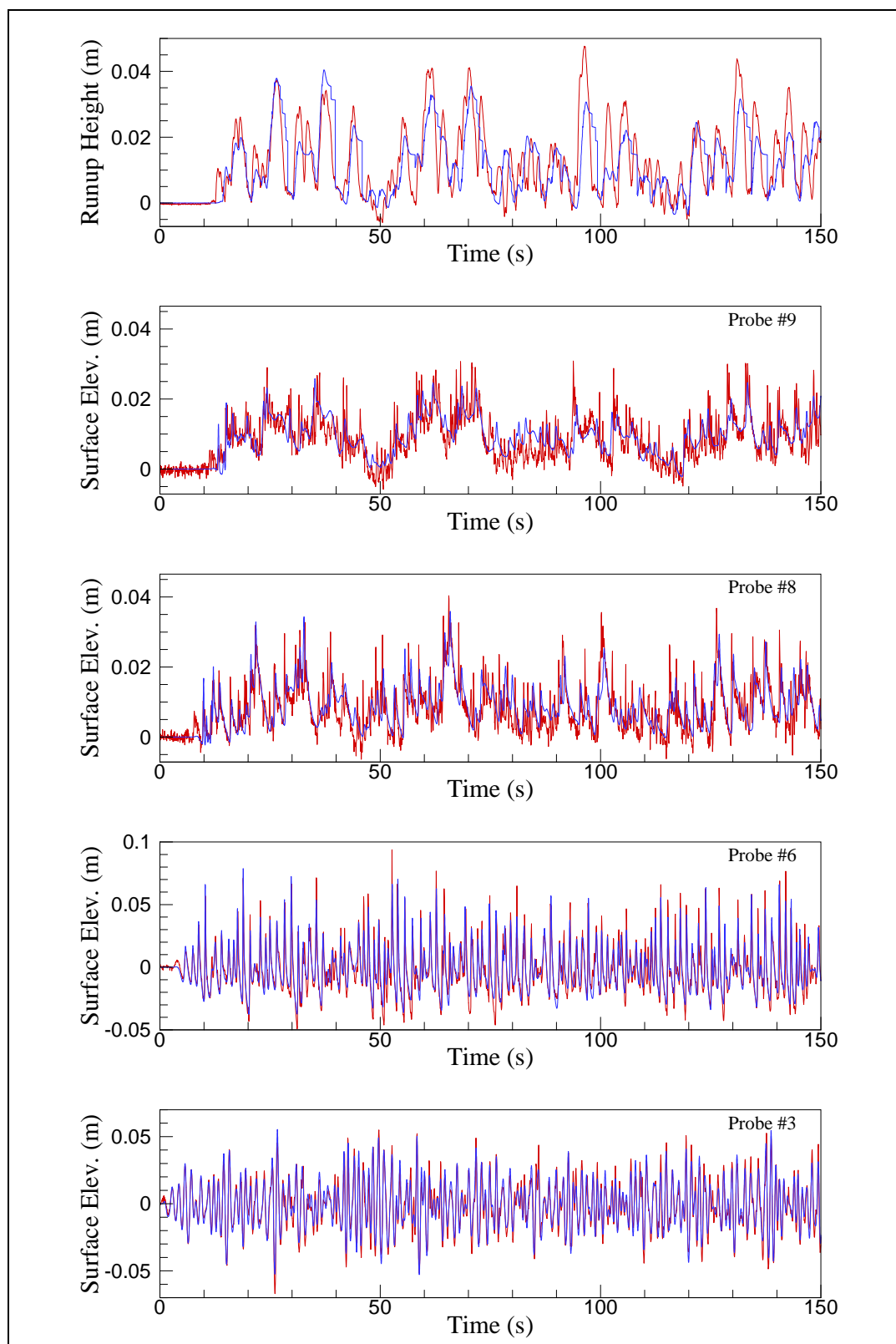


Figure 31. Measured and predicted surface elevation time series for Test-48; measured (red), numerical model prediction (blue).

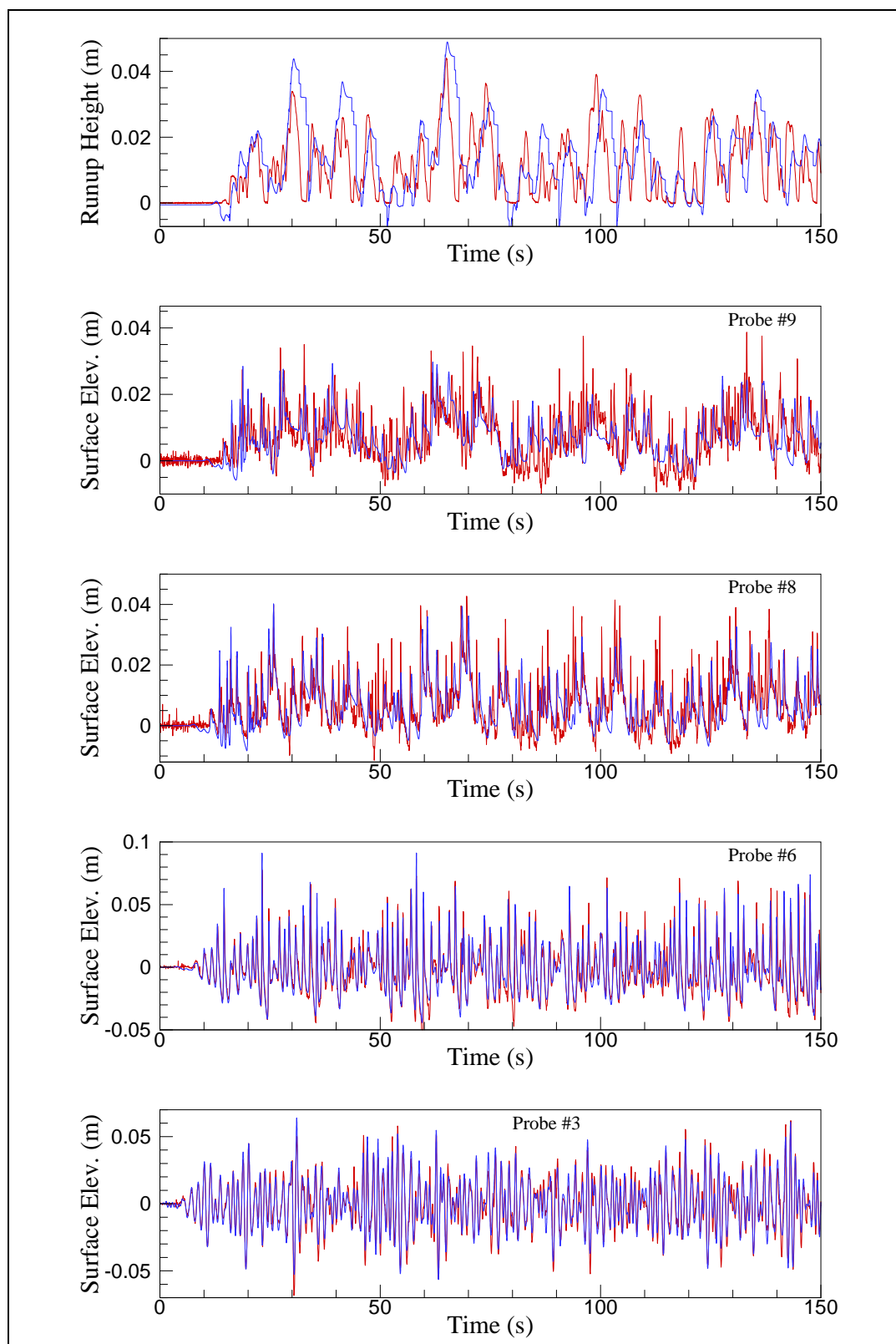


Figure 32. Measured and predicted surface elevation time series for Test-17; measured (red), numerical model prediction (blue).

The wave spectra plots clearly show the nonlinear transformation of the wave energy spectra from incident-wave frequencies in deep water to infragravity (low-frequency) motions over the reef flat. The Boussinesq model is able to reproduce the nonlinear energy transfer to the low frequency modes although there are differences in the detailed characteristics of the spectral densities (underprediction in some cases and overprediction in other cases). The wave spectra at the nearshore gauge (Gauge 9) had a predominant low-frequency peak, while the wave spectra at the mid-reef flat gauge (Gauge 8) had several distinct low-frequency peaks.

We also investigated the nonlinear evolution of the spectrum over the reef flat. The spectral densities were reanalyzed at a finer frequency resolution of 0.0025 Hz corresponding to 10 DOF. Figure 33 shows a detailed view of the spectrum in the low-frequency region (0 – 0.25 Hz) for Test-48.

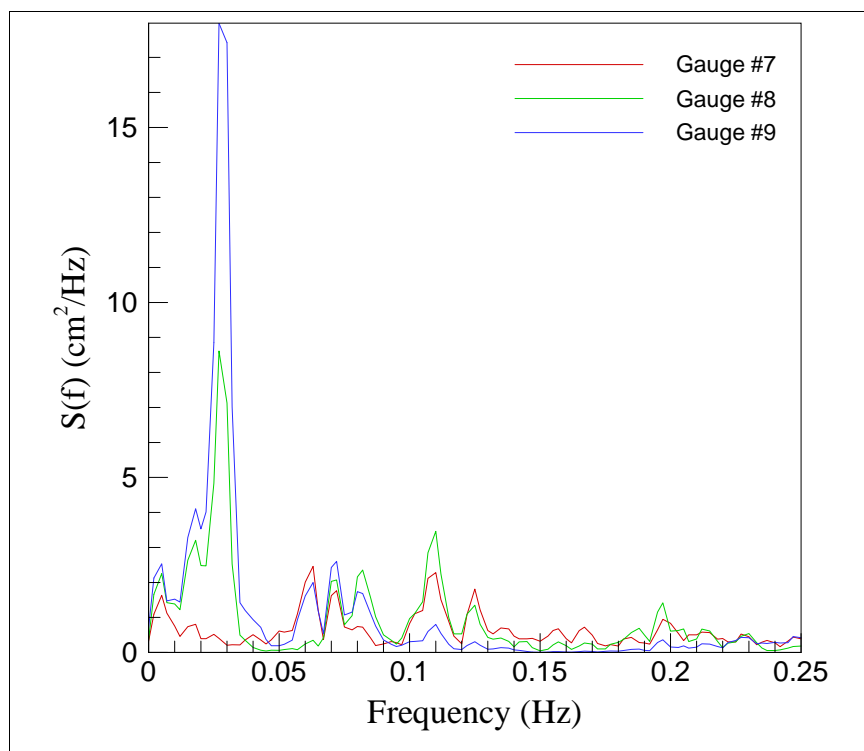


Figure 33. Low-frequency wave energy spectra for Test-48 at Gauges 7-9.

Gauges 8 and 9, located respectively at the middle and end of the reef flat, had spectral peak periods of approximately 35 sec. There is, however, very little energy at the 35 sec period (0.029 Hz) at the reef crest gauge (Gauge 7). The reef-beach system can be considered as an open basin with natural oscillation periods given by

$$T_n = \frac{4l_r}{(2n-1)\sqrt{gh_r}} \quad (19)$$

where  $l_r = 4.8$  m is the width of the reef top and  $h_r$  is still-water depth over the reef flat. The 35 sec period corresponds to the first reef oscillation mode ( $n = 1$ ) with a wavelength approximately equal to four times the width of the reef flat. The first mode has a node at the reef crest and an anti-node at the shoreline. The trapped waves would thus be resonantly amplified at the shoreline relative to the incident energy at the reef crest.

The water surface elevation time-series plots shown in Figures 29 to 32 provide further evidence that the Boussinesq model is able to reproduce the overall trends in the nonlinear wave transformation over fringing reefs. The numerical model is able to describe the nonlinear steepening and highly asymmetric profile of post-breaking waves in relatively shallow depths and the amplitude and phasing of the low-frequency motions over the reef flat. The low-frequency motions are stronger for the lower water level tests. The runup predictions are also reasonable, although there are slight discrepancies in details of the fluctuations. Given that the wave breaking process is parameterized in the Boussinesq model, one cannot expect the model to capture fine details of post-breaking waves on a wave-by-wave basis.

The predicted and measured maximum runup heights are summarized in Table 5. In general, the magnitudes of the model-predicted runup peaks are similar to the observed peaks with differences of the order of 10 percent.

Table 5. Summary of measured and calculated maximum runup heights.

Test ID	Maximum Runup Height (m)		% Difference
	MEASURED	PREDICTED	
Test-17	0.055	0.062	13
Test-18	0.084	0.090	6
Test-20	0.032	0.036	13
Test-21	0.072	0.075	4
Test-27	0.030	0.025	-16
Test-29	0.045	0.049	9
Test-30	0.060	0.064	7
Test-31	0.094	0.110	16
Test-36	0.040	0.042	6
Test-37	0.061	0.048	-21
Test-38	0.075	0.071	-5

Test ID	Maximum Runup Height (m)		% Difference
	MEASURED	PREDICTED	
Test-46	0.043	0.031	-29
Test-48	0.048	0.058	21
Test-57	0.075	0.066	-13
Test-58	0.083	0.083	0

Measured and calculated wave parameters are compared in Appendix A for fifteen tests (see Table 5). Since Gauge 4 appeared to be faulty (Demirbilek et al. 2007), data from this gauge were not included for comparisons presented in Appendices A and B. Tables A1-A8 provide measured and predicted significant wave height and wave setup for 15 tests at Gauges 1-3 and 5-9. Correlations between these are shown in Figures A1-A11. Overall, the comparison between measured and calculated (BOUSS-2D) wave heights is good at all gauges for all tests; the maximum difference is less than 15 percent, and values of correlation coefficient ( $R^2$ ) ranging from 0.87 to 0.99 for all 15 tests. Measured and predicted wave setup values on reef top at Gauges 8 and 9 are also in good agreement (less than 25 percent difference, with  $R^2$  of 0.94 and 0.9, respectively). Measured and calculated maximum runup heights in Table A9 and Figure A12 are also in good agreement (less than 30 percent difference and  $R^2$  of 0.88).

The CEM provides a formula (Equation VI-5-7) for determining irregular wave runup at the 2 percent exceedance probability level for a composite slope. This formula is used in Appendix B to compare measured runup values with the CEM empirical formulae. Measured and calculated runup estimates are summarized in Table B1. Figures B1 through B3 show a weak correlation ( $R^2 = 0.20$  to  $0.38$ ) between measured and CEM-based calculated maximum and 2 percent runup estimates with deepwater wave parameters used in the CEM empirical formulae. An improved correlation ( $R^2 = 0.78$ ) was obtained by using the measured significant wave height at the toe of beach slope (Figure B4). In contrast, BOUSS-2D-based maximum runup values in Table 5 for 15 test conditions agreed better to data than the empirical results. The average difference between measured and calculated (with BOUSS-2D) maximum runup is 7 percent, and the largest observed difference is less than 30 percent.

## 5 Field Experiments at Mokuleia, Hawaii

### Description of experiments

Field experiments were conducted over a 2-week period from 27 March to 9 April 2004 to measure wave propagation and dissipation over a reef on the Hawaiian coast by the University of Hawaii. The field site is located on the North Shore of Oahu, near Aweoweo Beach Park (Figure 34). This area is subject to north and northwest swells. A shore-perpendicular transect of three Seabird Electronics (SBE) pressure gauges was installed on the reef. A directional Waverider buoy in 198-m depth at Waimea Bay provided data on the incident wave conditions (Figure 34).



Figure 34. Overview map of field site for Hawaii PILOT experiments.

The bathymetry for the numerical model study was created using LIDAR survey data retrieved from [http://shoals.sam.usace.army.mil/Hawaii/pages/Hawaii\\_Data.htm](http://shoals.sam.usace.army.mil/Hawaii/pages/Hawaii_Data.htm).

The bathymetric data were interpolated onto a rectangular grid with uniform grid spacing of 10 m. The grid covers a 3,600- by 2,300-m area bounded by UTM Coordinates 585,080 to 588,680 m east and 2,386,430

to 2,388,730 m north as shown in Figure 35. The maximum depth in the offshore region was 32 m. The pressure sensor locations are also shown in Figure 35 with the outer reef gauge (SB-59) located in about 10 m of water, a mid-depth gauge (SB-55) in about 5 m of water, and a nearshore gauge (SB-57) in about 1 m of water. The water depths are relative to the mean sea level.

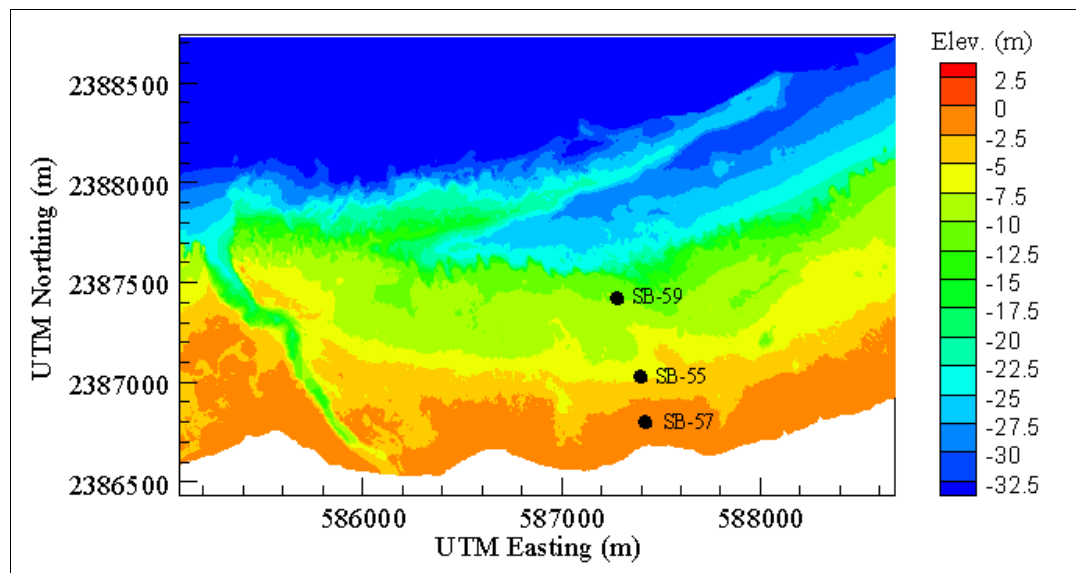


Figure 35. 2D map of bathymetry near Mokuleia Beach used for Boussinesq model simulations (times UTC).

A plot of the wave climate recorded at the Waimea Bay buoy over the 2-week period from 27 March to 10 April 2004 is shown in Figure 36. A number of distinctive wind-wave and swell events can be seen in the figure. Nine storm events representing different combinations of significant wave height, peak period, wave direction, and water levels were selected for detailed model-data comparisons. A summary of those events is presented in Table 6.

## Evaluation of Boussinesq model

Numerical simulations were carried out to predict wave transformation over the reef for the nine storm events listed in Table 6. The simulations were performed with time step size  $\Delta t = 0.10$  sec and grid spacing  $\Delta x = \Delta y = 10$  m. The directional wave spectra recorded at the buoy were used to generate boundary conditions for the Boussinesq model.

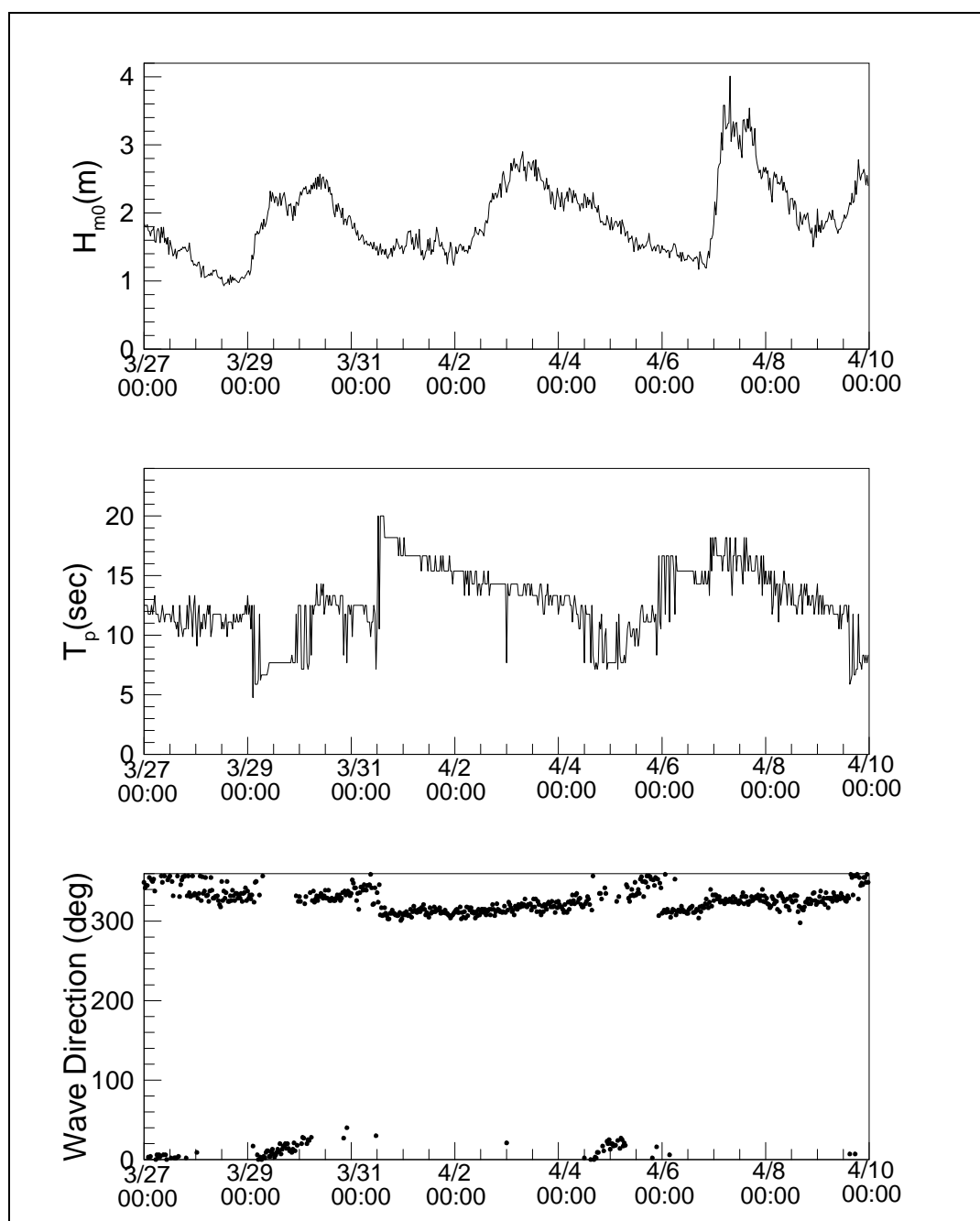


Figure 36. Wave climate recorded at Waimea Bay buoy in April 2004 (times UTC).

The spectral data from the buoy were stored in terms of frequency-dependent directional Fourier coefficients. An algorithm was developed to convert the Fourier coefficients to directional spectra using the Maximum Entropy Method of Nwogu (1989). The BOUSS-2D code was also modified to read in raw directional spectra files. No transformation from the 200-m depth to the 32-m depth at the model boundary was performed.



Table 6. Summary of selected storm events used in Boussinesq simulations for Mokuleia.

Storm Event	Day	Time (UTC)	$H_s$ (m)	$T_p$ (sec)	$D_p$ (deg)	Water Level (m)
1	3/30/2004	10:00	2.57	12.50	331	0.512
2	4/01/2004	10:00	1.31	16.67	321	0.610
3	4/03/2004	04:00	2.80	14.29	308	0.107
4	4/03/2004	10:00	2.64	14.29	318	0.630
5	4/03/2004	17:00	2.47	13.33	319	0.216
6	4/07/2004	01:00	2.16	18.18	333	0.604
7	4/07/2004	06:30	3.25	18.18	325	0.256
8	4/07/2004	12:00	2.96	16.67	322	0.450
9	4/07/2004	18:00	3.26	15.38	331	0.027

The buoy-recorded directional wave spectra for two selected events, Storm Event 3, on 3 April 2004, at 04:00 UTC, and Storm Event 7, on 7 April 2004, at 06:30 UTC, are plotted in Figures 37 and 38, respectively. The corresponding frequency spectra are respectively plotted in Figures 39 and 40. In general, the sea states were bimodal with long-period swell and local wind-generated sea state components.

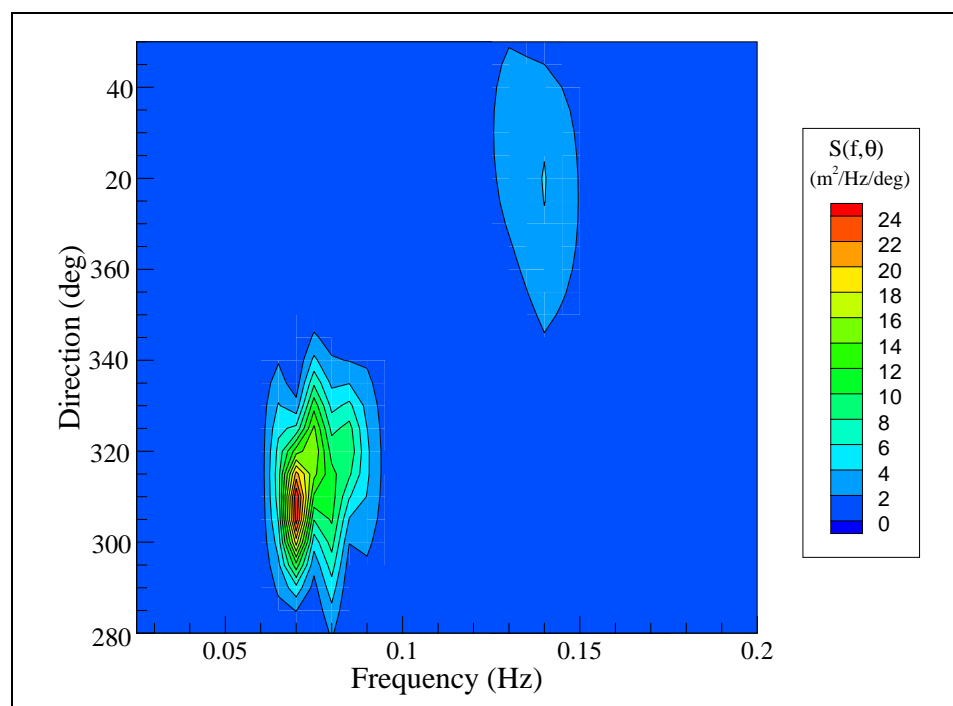


Figure 37. Measured directional wave spectrum at Waimea Bay buoy on 3 April 2004 at 04:00 UTC.

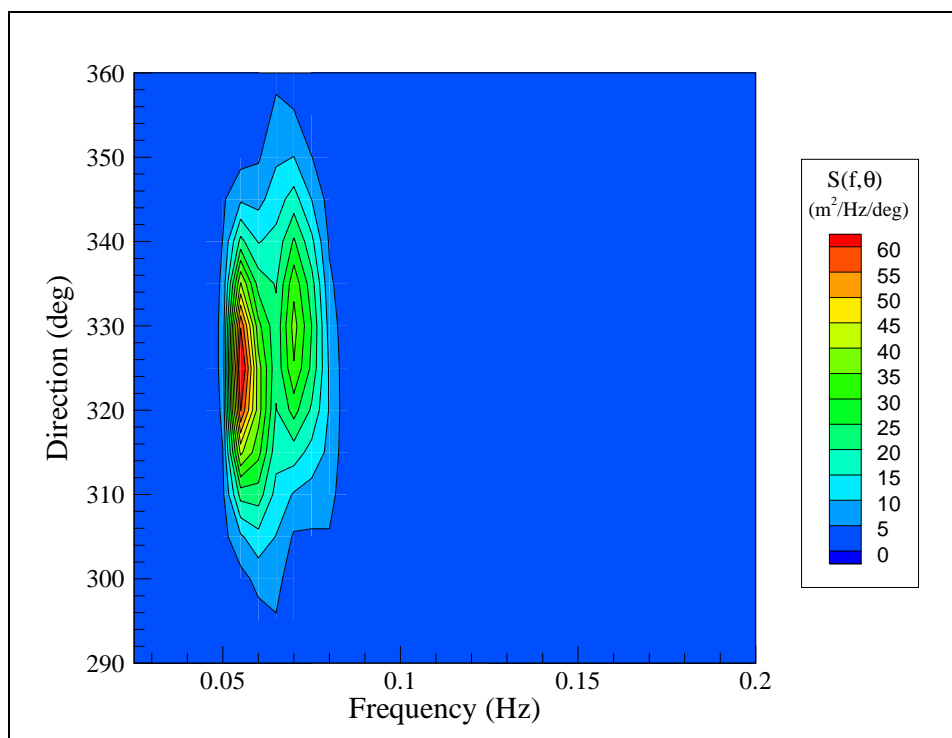


Figure 38. Measured directional wave spectrum at Waimea Bay buoy on 7 April 2004 at 06:30 UTC.

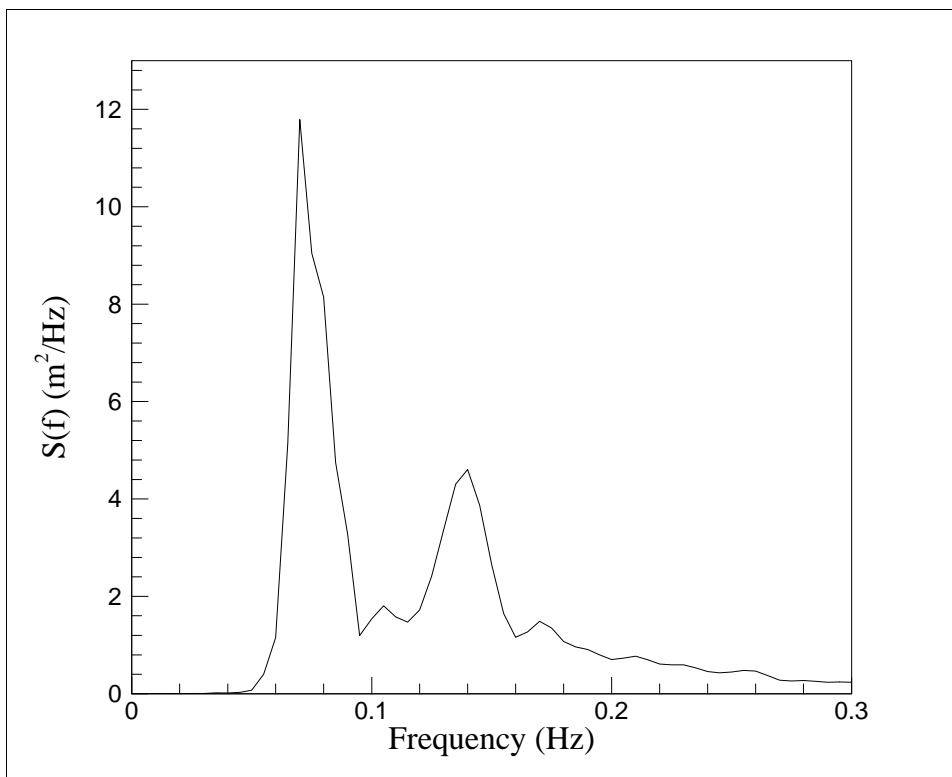


Figure 39. Measured wave spectrum at Waimea Bay buoy on 3 April 2004 at 04:00 UTC.

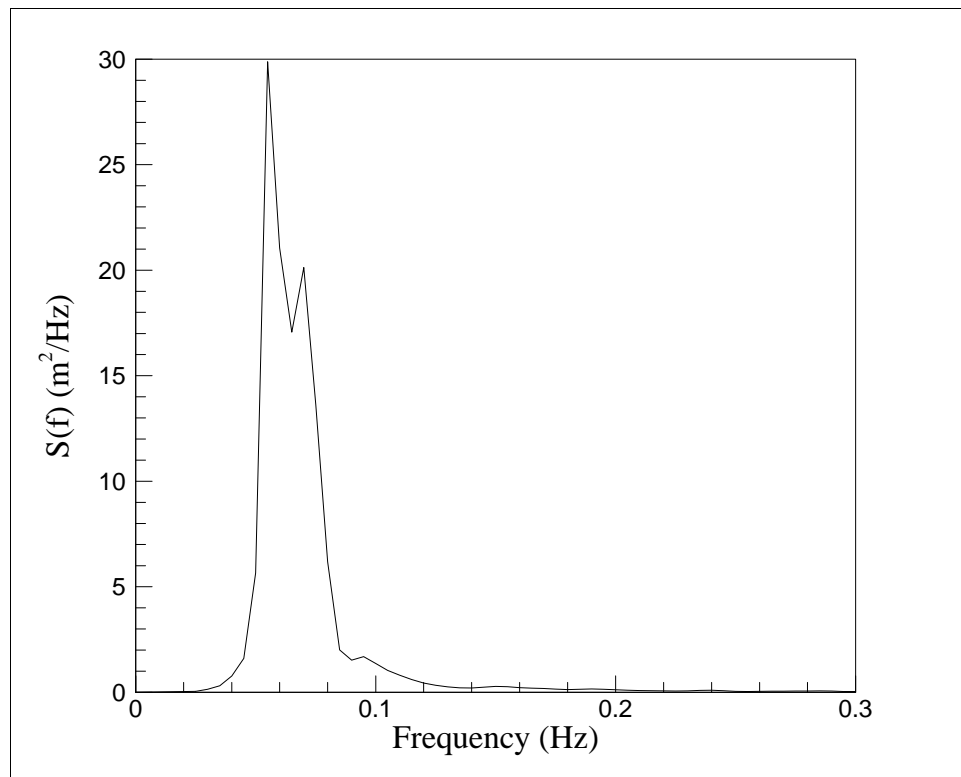


Figure 40. Measured wave spectrum at Waimea Bay buoy on 7 April 2004 at 06:30 UTC.

A 3D view of the simulated waves propagating and breaking on the reef is shown in Figure 41 for Storm Event 7. A Google satellite image of wave transformation over the field site is shown in Figure 42. Extensive wave breaking can be seen over the reef. The predicted significant wave height distributions for Storm Events 3 and 7 are plotted in Figures 43 and 44, respectively. The variability in the wave height plots near the offshore boundary is due to the diffraction of waves that propagate into the computational domain at oblique angles. Storm Event 3, for example, consisted of a northwesterly swell with a peak direction of 310 deg and a north-easterly local sea with a peak direction of 20 deg. Both systems propagate into the North-South oriented grid at significant oblique angles.

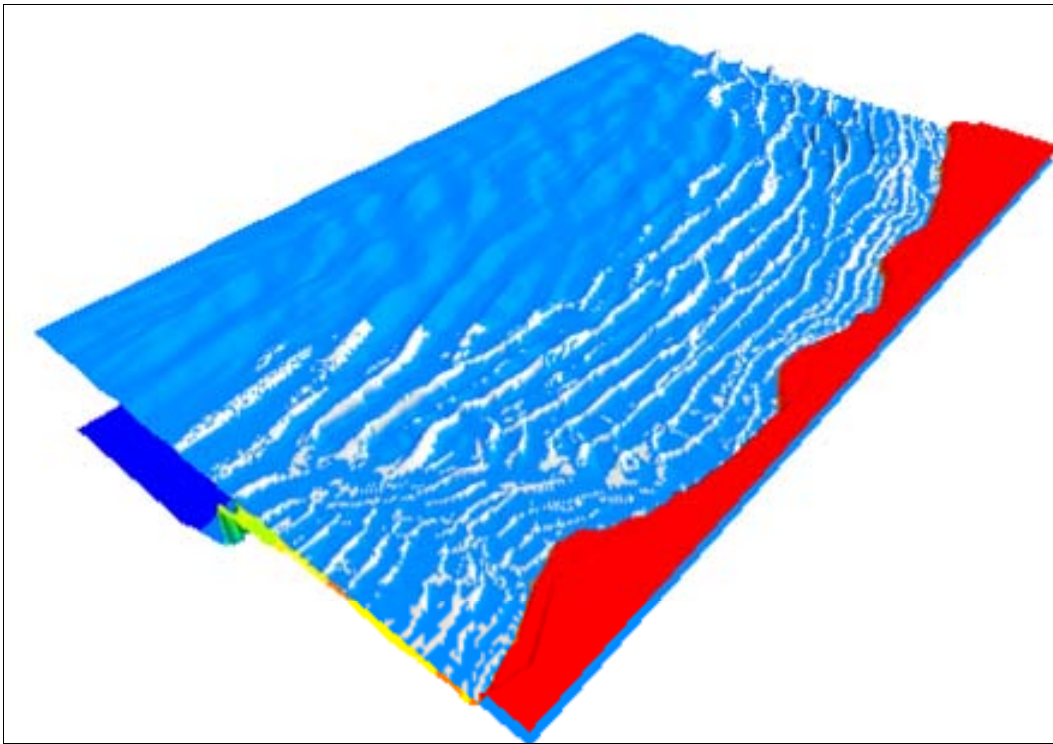


Figure 41. Three-dimensional view of waves propagating over Mokuleia reef (Storm Event 7 on 7 April 2004 at 06:30 UTC).



Figure 42. Google satellite image of waves propagating over Mokuleia reef (instrumentation transect location shown in white).

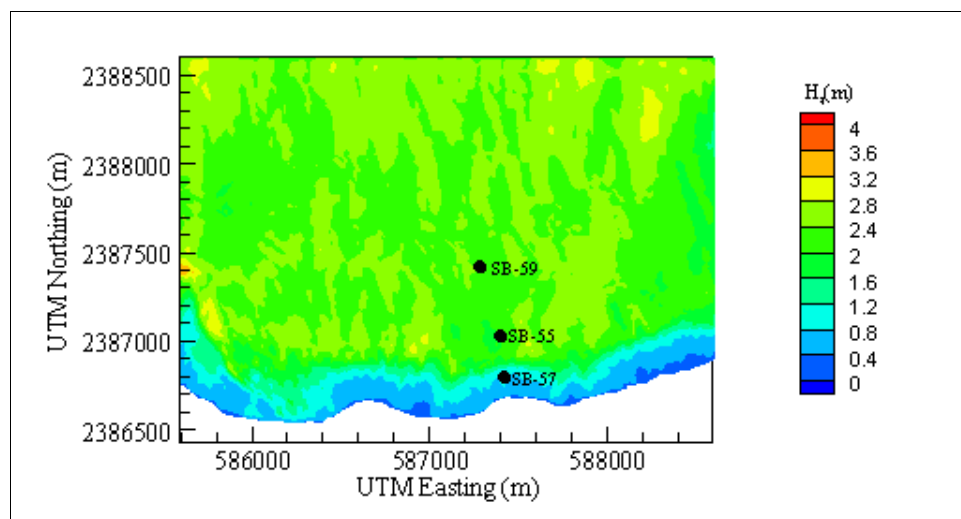


Figure 43. Predicted significant wave height distribution for Storm Event 3 ( $H_s = 2.8$  m,  $T_p = 14.3$  sec).

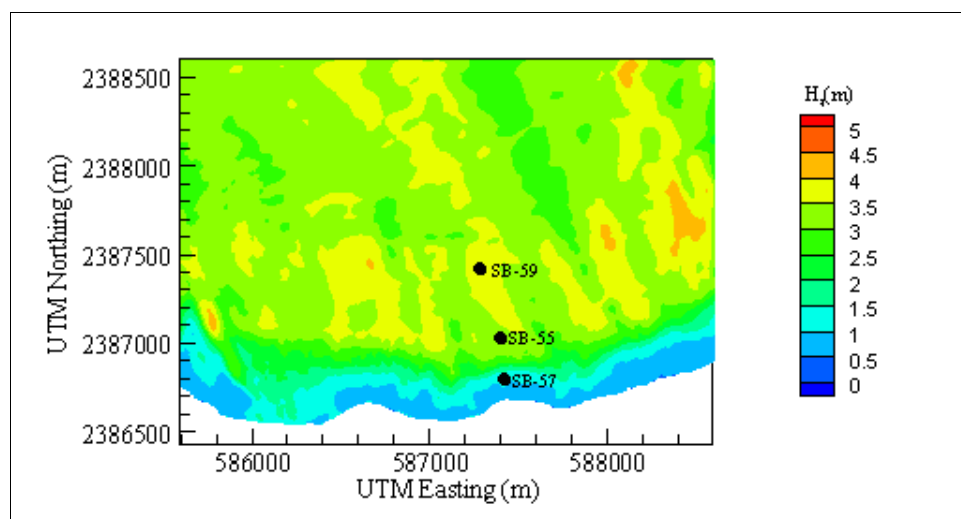


Figure 44. Predicted significant wave height distribution for Storm Event 7 ( $H_s = 3.25$  m,  $T_p = 18.2$  sec).

The measured and predicted wave spectra at the different gauge locations are plotted in Figures 45 to 50. The numerical model tended to slightly overestimate the wave energy at the outer and mid-depth gauges. The authors suspect that this is due to the fact that the wave buoy used to drive the numerical model was located approximately 11 km away from offshore boundary of the numerical model in about 200 m of water. The directional wave spectrum for swell events could have significantly evolved between the 200-m-contour buoy location and the 35-m contour offshore boundary of the numerical model.

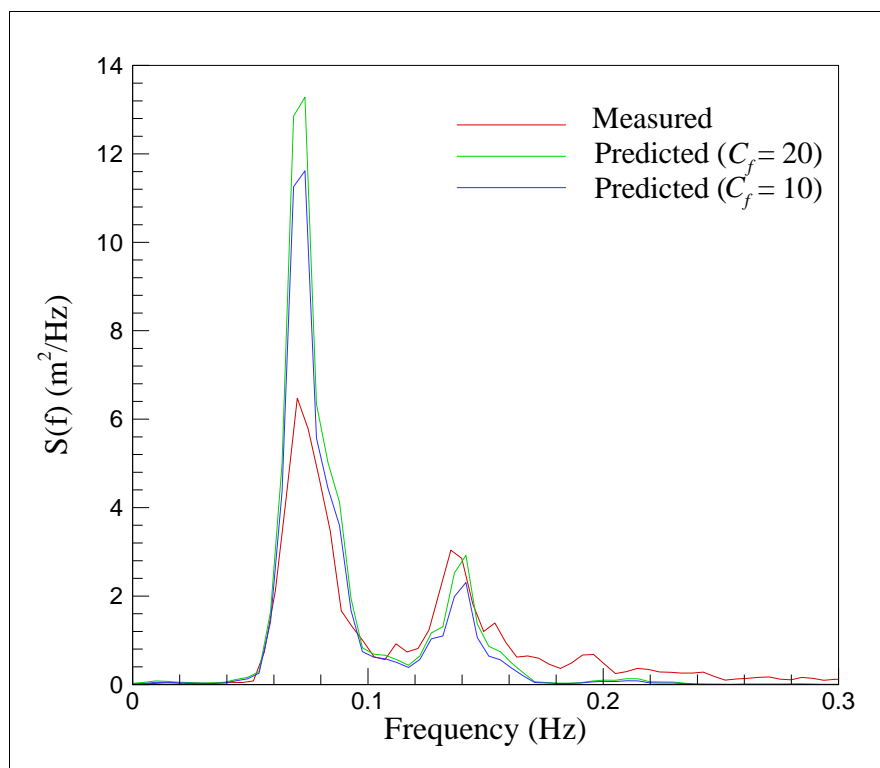


Figure 45. Measured and predicted wave spectra at outer reef gauge (SB-59) for Storm Event 3.

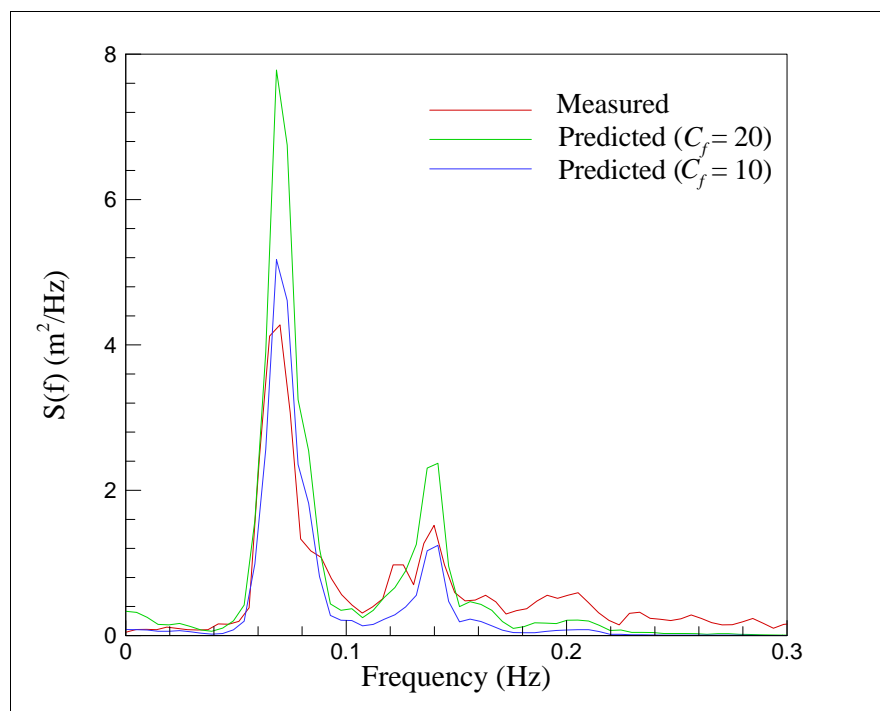


Figure 46. Measured and predicted wave spectra at mid-depth gauge (SB-55) for Storm Event 3.

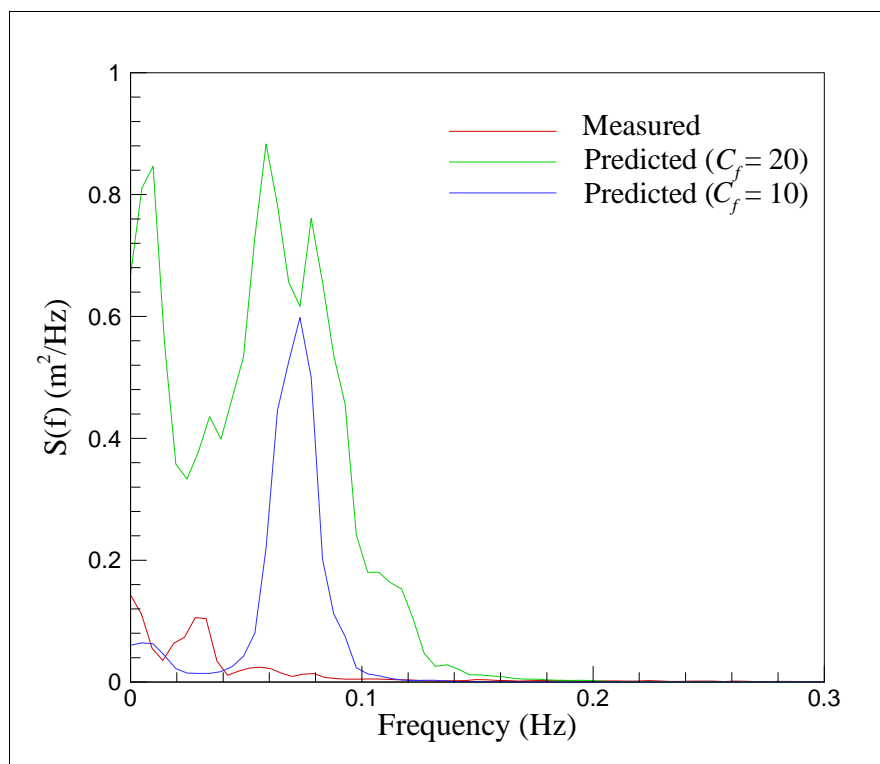


Figure 47. Measured and predicted wave spectra at nearshore gauge (SB-57) for Storm Event 3.

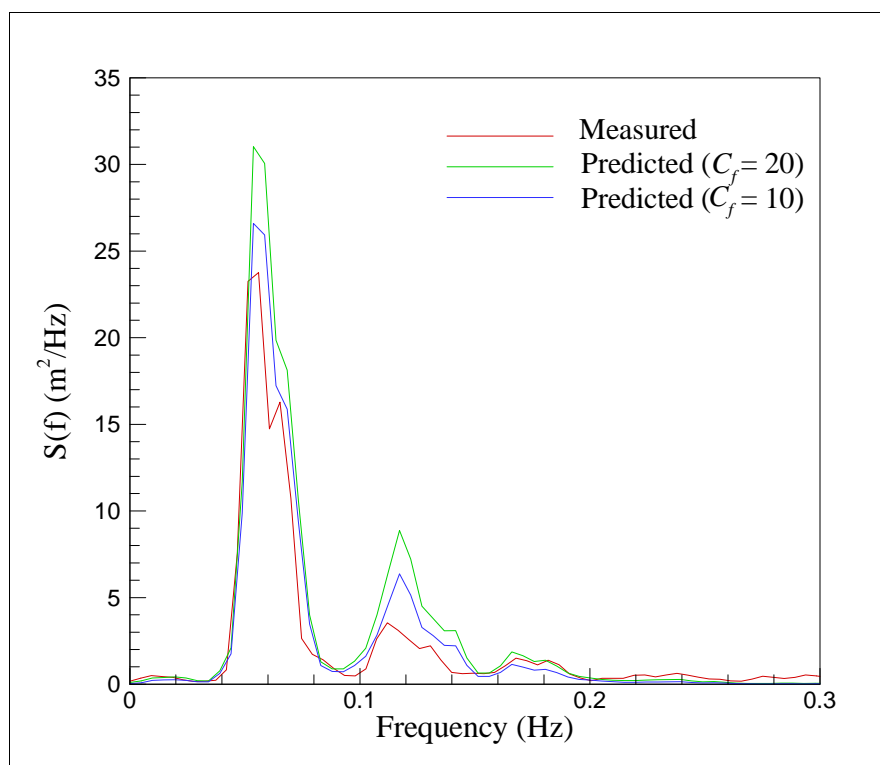


Figure 48. Measured and predicted wave spectra at outer reef gauge for Storm Event 7.

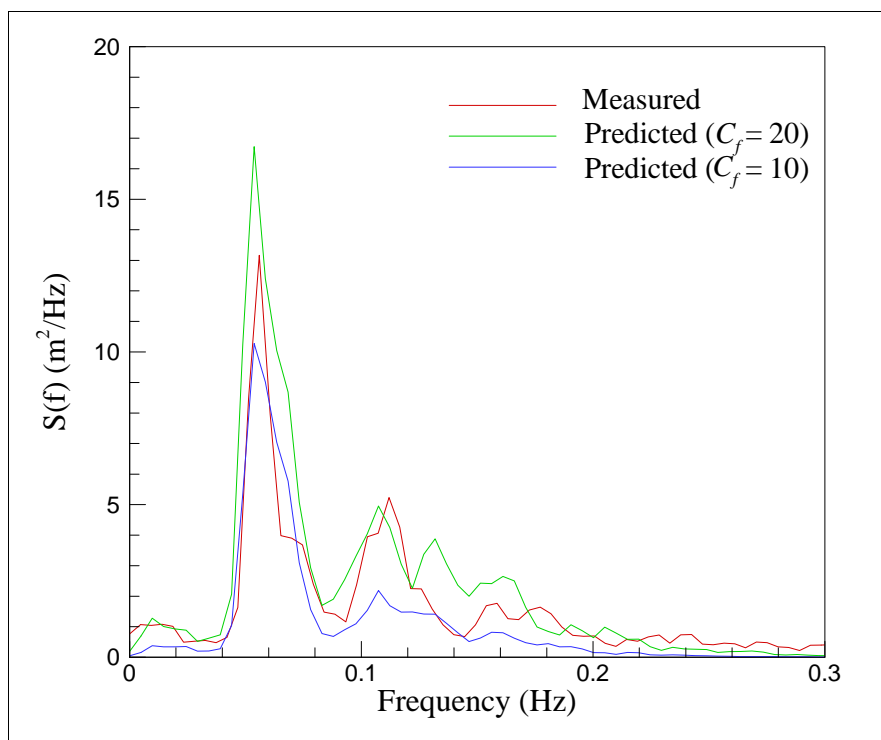


Figure 49. Measured and predicted wave spectra at mid-depth gauge for Storm Event 7.

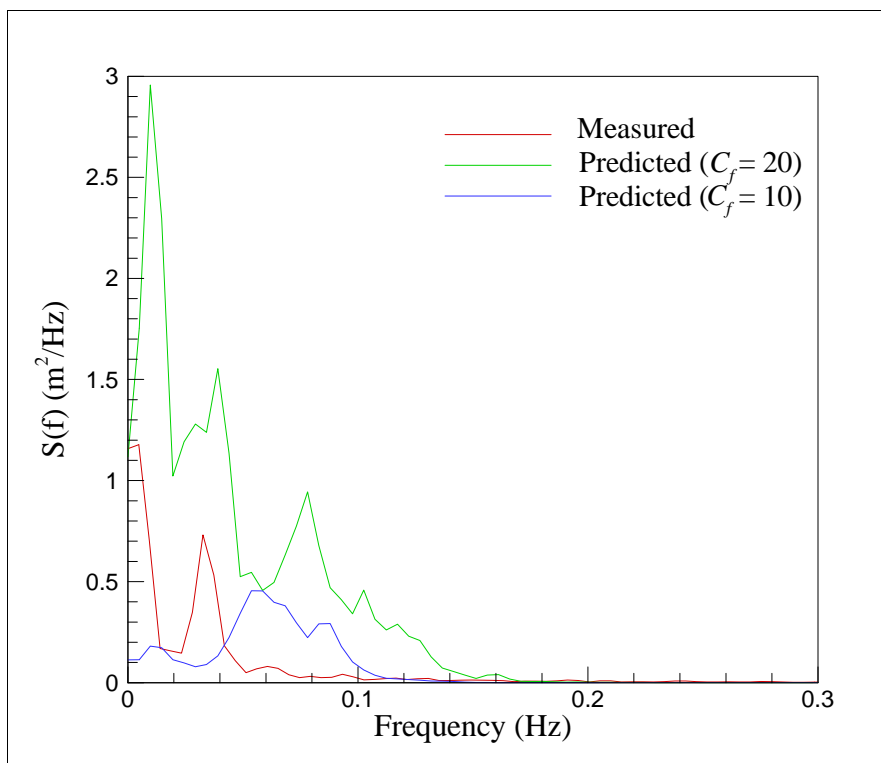


Figure 50. Measured and predicted wave spectra at nearshore gauge for Storm Event 7.



Comparatively larger differences between the numerical model predictions and the measured wave spectra occurred at the nearshore (SB-57) gauge location. The measured data indicated extensive dissipation of wave energy between the mid-depth gauge (SB-55) and nearshore gauge (SB-57) which are located a distance of approximately 250 m apart. For Storm Event 3, the measured significant wave height decreased from 1.74 m at SB-55 to 0.29 m at SB-57, while the numerical model predicted an  $H_s$  value of 0.58 m at SB-57 location.

We attempted to improve the model-data match by increasing the bottom friction coefficient. Several field experiments have shown that the rate of wave energy dissipation over reefs is significantly higher than sandy beaches (see Lowe et al. (2005) and references therein). Lowe et al. (2005) estimated the magnitude of the wave friction factor  $f_w$  at barrier reef in Kaneohe Bay, Hawaii, to be of the order of 0.28, much larger than the 0 [0.01] magnitude used for sandy beaches. The characteristic bottom roughness length scale at the site was of the order of 0.2 m. The Boussinesq model simulations were repeated with a larger wave friction factor  $f_w = 0.2$  ( $C_f = 10$ ). The results are also shown in Figures 45 to 50. Although the higher wave friction factor led to a decrease in the overall wave energy, it did not improve the frequency-domain spectral comparisons at the nearshore gauge (see Figures 47 and 50). The quadratic drag law parameterization dissipates wave energy across a broad range of frequencies including the infragravity band, in contrast to the field data that showed a preferential dissipation of the wave energy in the incident wind-wave frequency band.

One hypothesis for wave energy dissipation over rough surfaces with the characteristic roughness scales of the order of 10 percent of the water depth is that the turbulent boundary layer is no longer restricted to a thin layer near the bottom but rather permeates the entire water column. This would lead to an eddy-viscosity type formulation for energy dissipation due to bottom roughness as opposed to the quadratic shear stress formulation. Garnier and Nachbin (2006) derived from first principles a formulation for the eddy viscosity due to the interaction of long waves with rough surfaces. The eddy viscosity represents a parameterization of the transfer of energy from coherent wave motions to non-coherent turbulent motions. In general, the eddy viscosity depends on the characteristic height and length scale of the bottom surface roughness. Since most of the studies in the literature on wave energy dissipation in the marine

environment are based on the drag-law parameterization, additional laboratory and field experiments are required to investigate the potential use of the eddy-viscosity formulation for coral reefs.

We investigated the potential application of the eddy-viscosity based formulation of frictional dissipation by using the Smagorinsky formulation in the BOUSS-2D model where the eddy viscosity is related to the grid size and velocity gradients (see Equation 16). Figures 51 to 53 show the results obtained using two values of the Smagorinsky coefficient,  $C_v = 0.5$  and  $1.0$ , with  $C_f = 20$ . The eddy-viscosity formulation preferentially dissipates the higher frequency energy and matches the measured data much better. However, the model still overestimated the wave energy nearshore at the mid-reef gauge (see Figure 53). Based on field data obtained from the Guam field experiments (see Chapter 6) using both Aquadopp (AQD) current profilers and SBE pressure gauges, we concluded that the performance of the SBE pressure gauges was questionable at low water levels under breaking waves. Hence, we did not conduct detailed model-data comparisons for the rest of the Mokuleia field data.

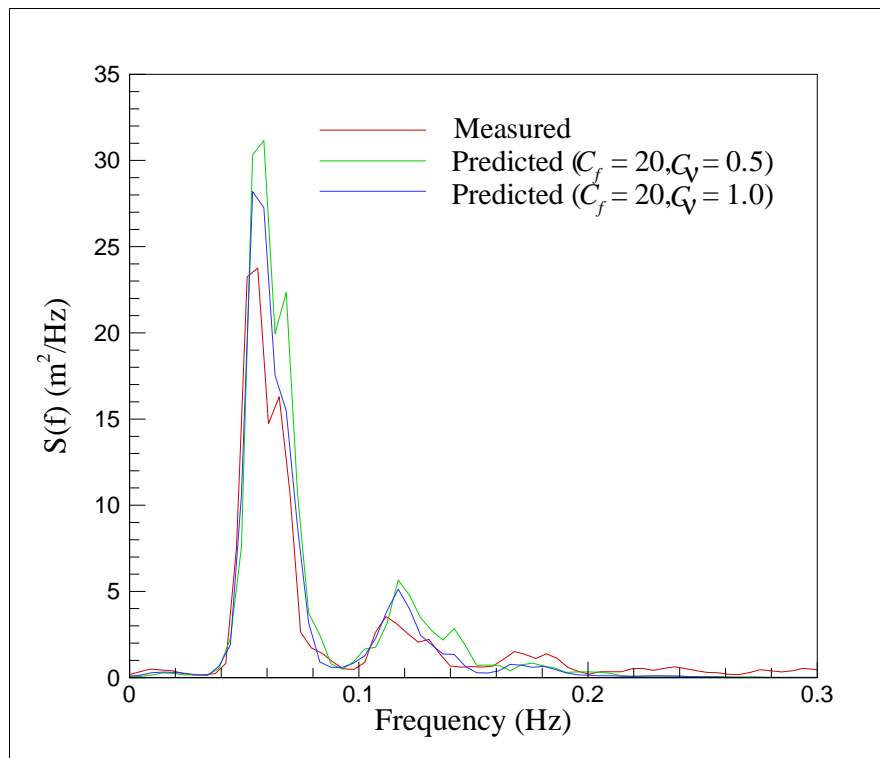


Figure 51. Measured and predicted wave spectra at outer reef gauge for Storm Event 7 obtained with two different values of Smagorinsky coefficient.

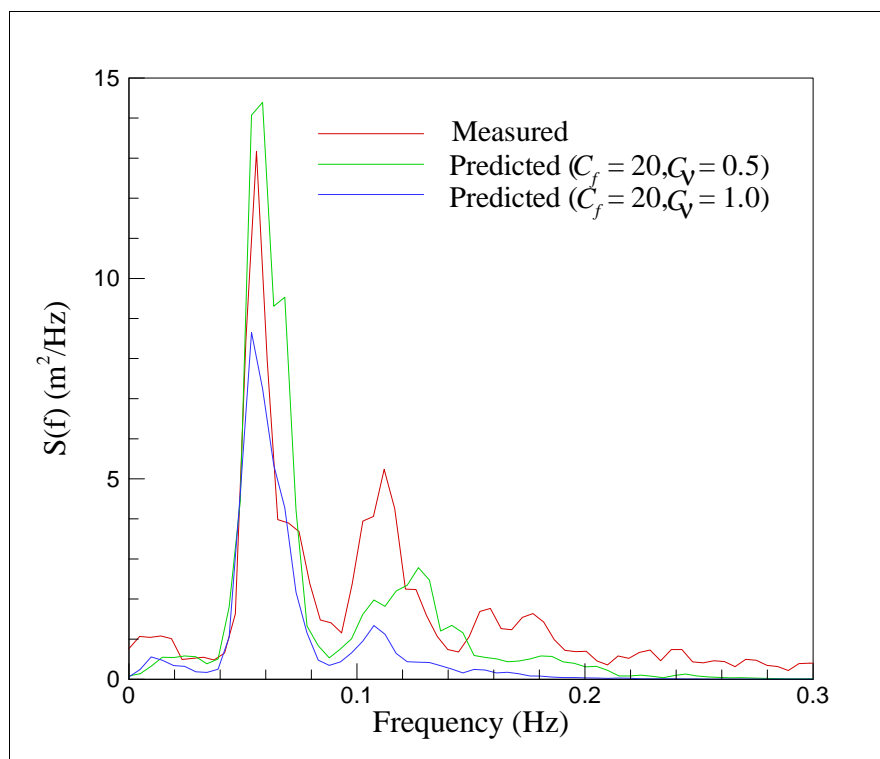


Figure 52. Measured and predicted wave spectra at mid-reef gauge for Storm Event 7 obtained with two different values of Smagorinsky coefficient.

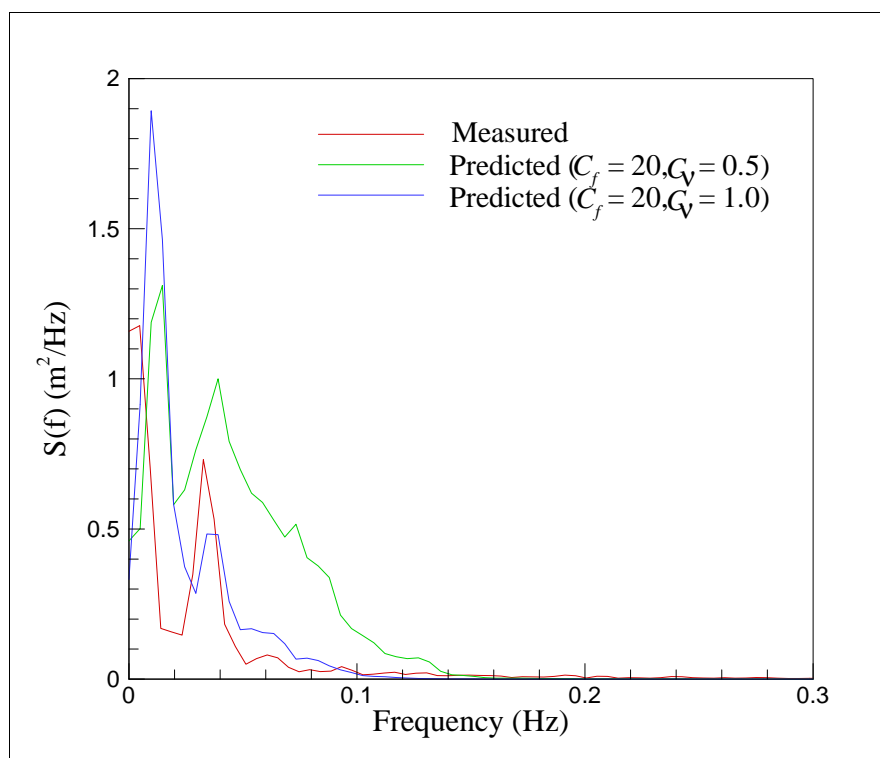


Figure 53. Measured and predicted wave spectra nearshore at mid-reef gauge for Storm Event 7 obtained with two different values of Smagorinsky coefficient.

## 6 Field Experiments at Ipan, Guam

### Description of experiments

The Island of Guam, located in the Western Pacific Ocean, is surrounded by shallow fringing coral reefs. Field experiments were conducted to investigate wave energy transformation at a site along Guam's southeast coast near Ipan. The geomorphological structure of the reef near the field site is shown in Figure 54. The reef flat is classified as pavement (solid carbonate rock) structure while the reef face is classified as an aggregate structure. The reef flat is occasionally exposed at low tide and is covered with algae as shown in Figure 55.

Four Aquadopp AQD current profilers and three SBE pressure transducers were installed along a cross-shore transect over the reef as shown in Figure 56. The UTM gauge coordinates for these instruments are provided in Table 7. A photograph of an AQD placed on the reef crest is shown in Figure 57. The AQD profiler collected data for a duration of 1,024 sec at a sampling frequency of 1 Hz every 20 min, while the SBE gauges collected data every hour at a sampling frequency of 4 Hz for 885 sec. A Datawell directional wave buoy installed by the Coastal Data Information Program (CDIP) of Scripps Institution of Oceanography provided data on the incident wave conditions. The buoy (CDIP Sta 121) is located in 200 m of water at 13.3542°N, 144.7883°E, approximately 2.4 km southeast of the instrumentation transect.

The University of Hawaii provided data over a 9-day period from 16-24 October 2005. The offshore wave climate recorded by the CDIP buoy during the time frame is shown in Figure 58. A storm event occurred on 20 October with a significant wave height of 2.3 m and spectral peak period of 12 sec. The predominant wave direction during the storm was 70° (ENE).

Information on water level changes was obtained from a NOAA tide gauge located in Pago Bay, Guam (13.4283°N, 144.7967°E). The tidal water level variation during the 9-day field experiment period is shown in Figure 59. The water levels are relative to the Mean Lower Low Water (MLLW) tidal datum. The tide is semi-diurnal with pronounced diurnal inequalities. The maximum tidal range was 0.7 m (2.3 ft).

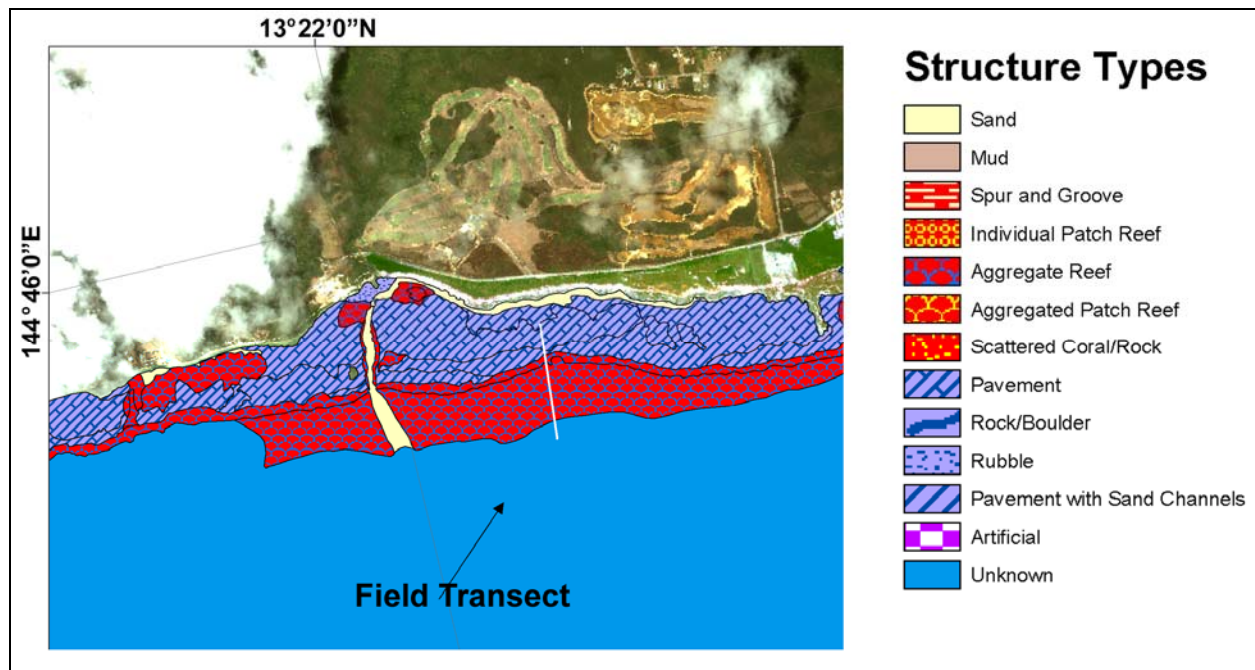


Figure 54. Map showing geomorphological reef structure types near field site (produced by NOAA Biogeography program).



Figure 55. Photograph of reef flat exposed at low tide (courtesy of U Hawaii).



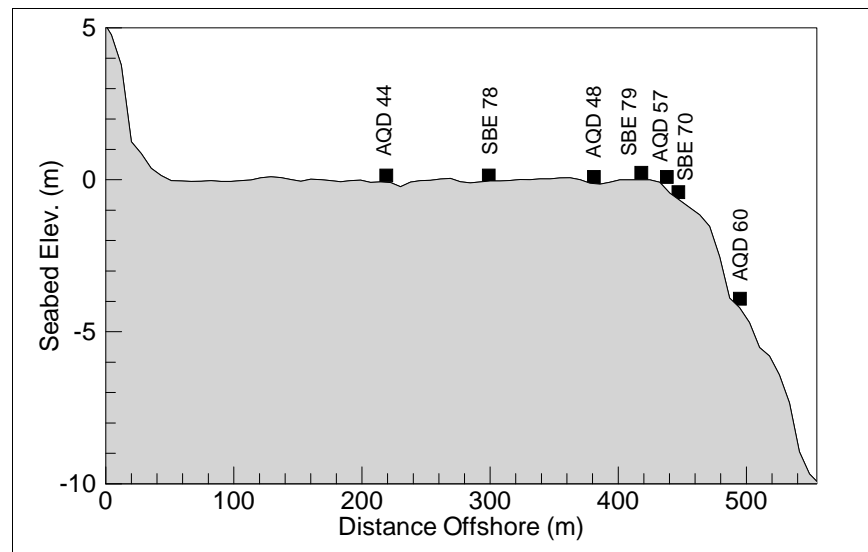


Figure 56. Cross-shore profile of reef along instrumentation transect.

Table 7. Gauge locations in UTM coordinates.

Gauge ID	UTM Easting (m)	UTM Northing (m)
AQD 44	258929	1479426
SBE-78	259009	1479402
AQD 48	259091	1479392
SBE-79	259128	1479392
AQD 57	259148	1479387
SBE-80	259157	1479390
AQD 60	259206	1479376



Figure 57. Aquadopp profiler installed on reef crest (photograph courtesy of U Hawaii).

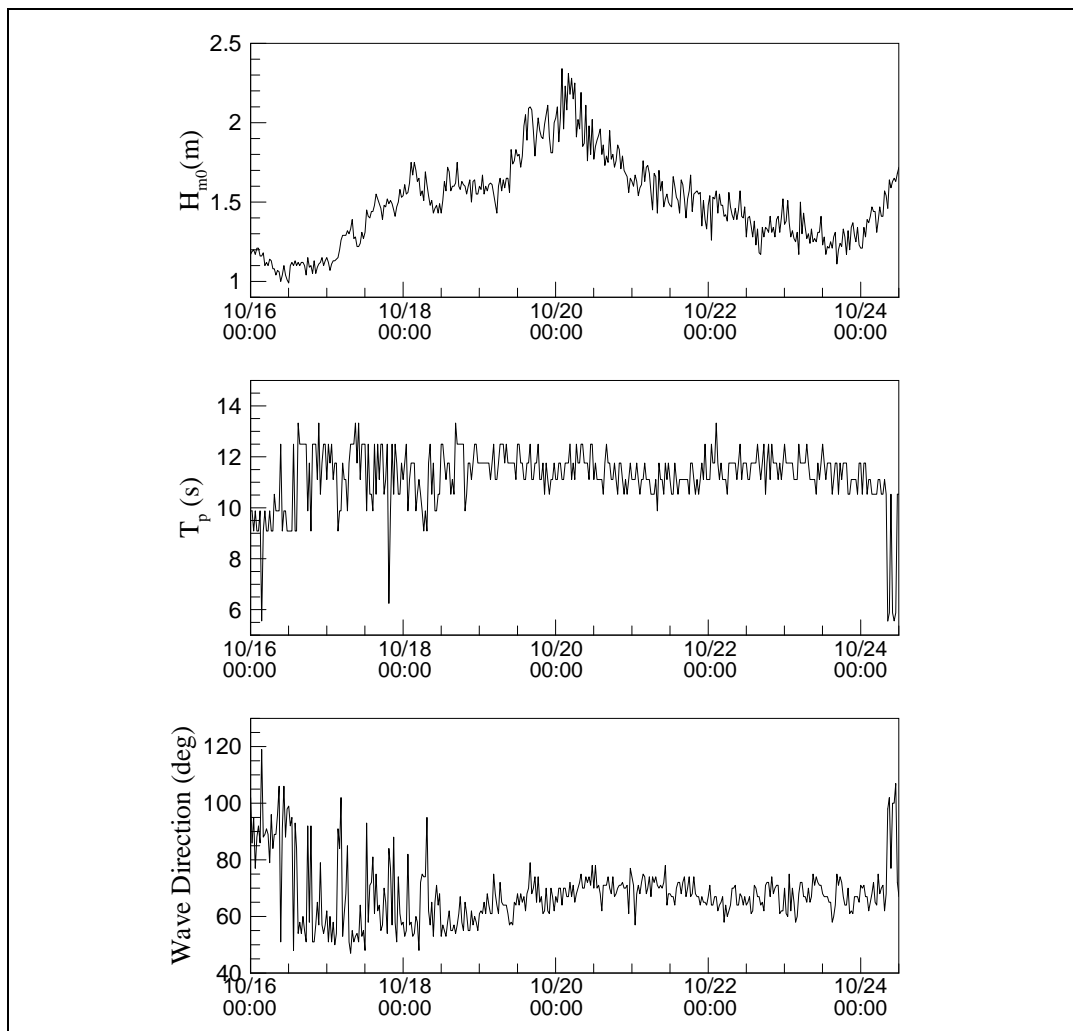


Figure 58. Wave climate recorded by CDIP Sta 121 at Ipan in October 2005.

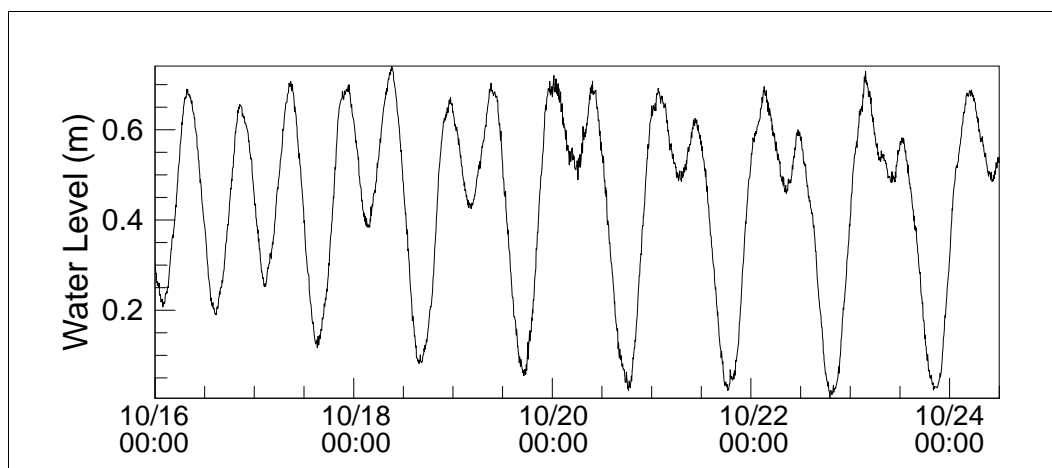


Figure 59. Water level variation recorded at Pago Bay tide gauge in October 2005 (MLLW Datum).

Data from the Aquadopp profilers were analyzed to obtain the significant wave heights and spectral peak periods. The spectral analysis was performed with 10 DOF, resulting in a frequency resolution of 0.002 Hz. The significant wave height and spectral peak periods are plotted in Figure 60 for the entire 9-day duration of the field experiment. The wave heights and periods on the reef face (AQD 60) are close to the buoy values, indicating very little modification to the overall wave energy as the waves propagate in deep water to the reef.

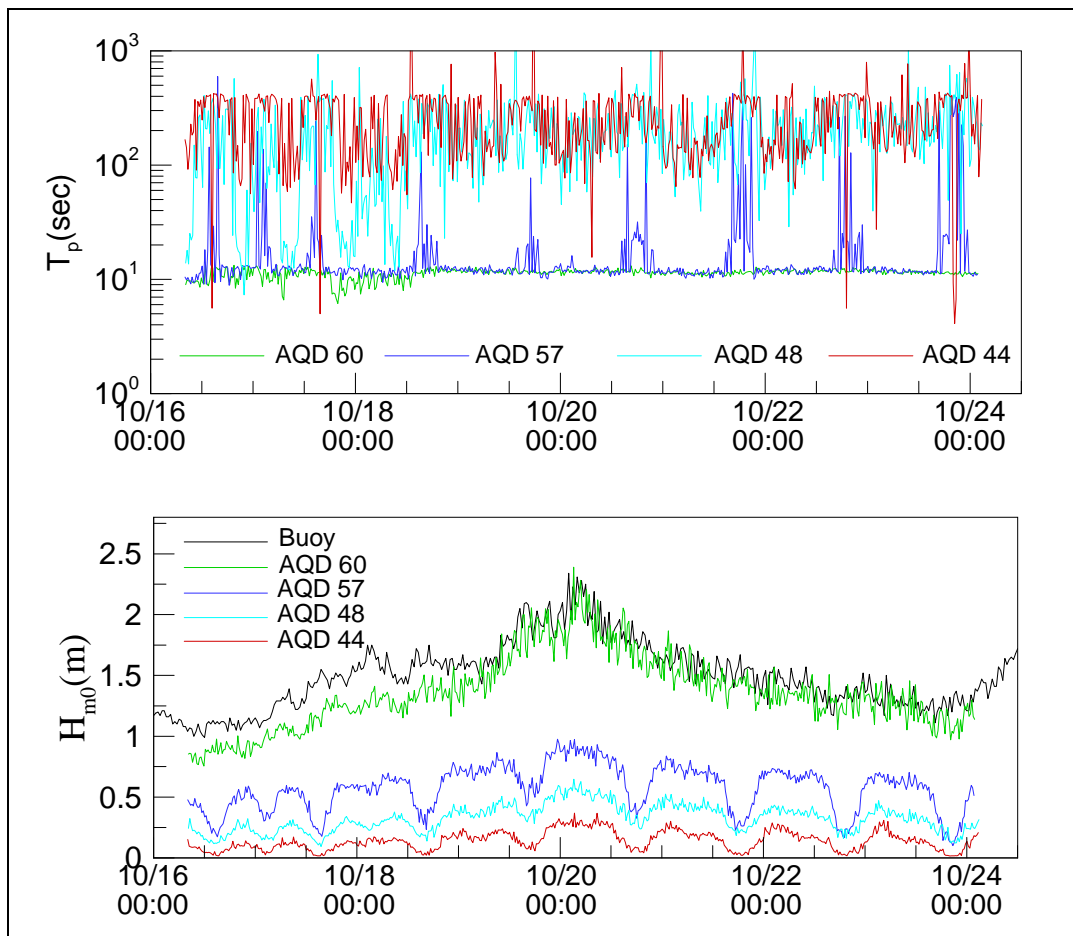


Figure 60. Significant wave heights and spectral peak periods recorded by Ipan reef gauges in October 2005.

Since the maximum water level on the reef flat is 0.7 m at high tide, waves were breaking on the reef face for the entire 9-day field experiment. The post-breaking wave heights on the reef crest gauge (AQD 57) and reef flat gauges (AQD 48, AQD 44) are strongly modulated by water level with dips in the  $H_{m0}$  values occurring during low water level periods. We also note that nonlinear cross-spectral energy transfer led to a change in the spectral peak period from wind-wave frequency band [O (10 sec)] at the reef face



gauge (AQD60) to the infragravity band [O (100 sec)] at the most shoreward reef flat gauge (AQD44). The wave periods at the intermediate gauges (AQD57 & AQD48) oscillate between the wind-wave and infragravity frequency bands depending on the water level and incident wave height.

Since several wave breaking formulations assume a constant wave height-to-water depth ratio after breaking, we plotted the relative wave height ( $H_{mo} / (h + \bar{\eta})$ ) ratio at two of the reef flat gauges AQD 48 and 44 (Figure 61). We notice that  $H_{mo} / (h + \bar{\eta})$  is not constant but decreased between AQD 48 and 44. The wave height-to-water depth ratio also varied over the 9-day period, indicating a weak dependence on wave height, period, and/or direction.

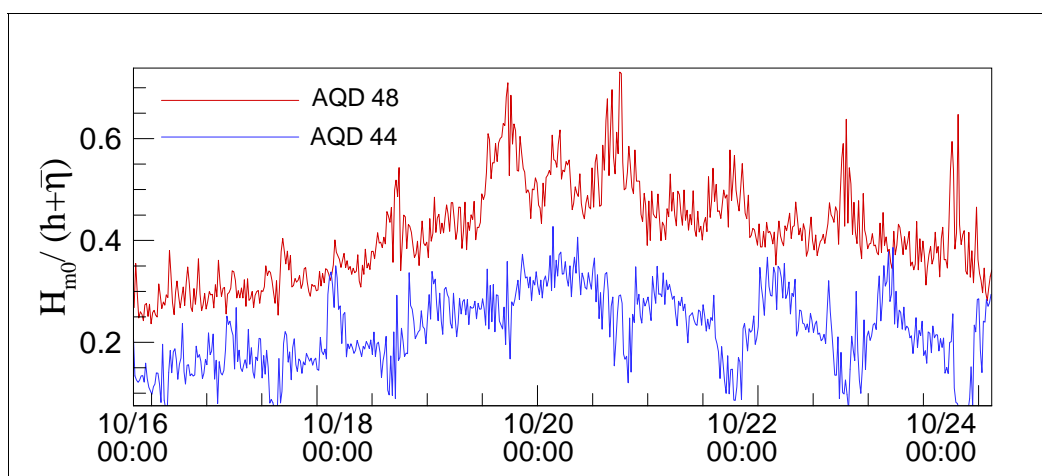


Figure 61. Wave height-to-water depth ratios recorded by lpan reef flat gauges in October 2005.

A plot of the magnitude of the time-averaged current ( $\sqrt{\bar{U}^2 + \bar{V}^2}$ ) is shown in Figure 62. Since the reef flat is relatively shallow, strong currents are generated on the reef flat by both the ambient tidal flow as well as storm waves. The largest currents occurred at the reef crest gauge (AQD 57). There is a baseline tidal flow of about 0.7 m/sec with perturbations due to wave-induced currents. The strongest wave-induced currents occur during low water level periods.

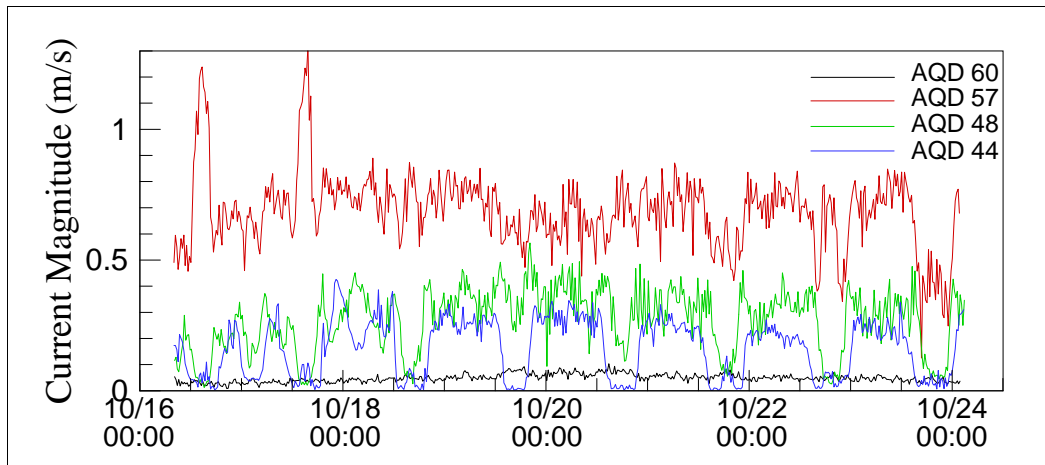


Figure 62. Mean current variation recorded by Ipan reef gauges in October 2005.

## Evaluation of Boussinesq model

Numerical simulations were carried out for seven distinct time periods around the peak of the storm as listed in Table 8. The different events were picked to represent different stages of the tide from low to high water. The bathymetry for the numerical model study was created using LIDAR survey data. The bathymetric data were interpolated onto a 301 by 301 rectangular grid with a uniform grid spacing of 5 m. The grid covers a 1,500- by 1,500-m area bounded by UTM Coordinates 258265 to 260000 (Easting) and 1478620 to 1480358 (Northing) with an orientation of the x-axis of 10 deg south of west as shown in Figure 63. The maximum depth in the offshore region was set to 20 m.

Numerical simulations were initially performed for the high-water level (WL = 0.69 m) for Storm Event 264. The directional wave spectrum recorded by the buoy was used to generate boundary conditions for the numerical model. The simulations were carried out using grid sizes  $\Delta x = \Delta y = 5$  m and time-step size  $\Delta t = 0.10$  sec for a duration of 2,800 sec. Default values were used for the turbulent length scale ( $l_t = H_s$ ) and Smagorinsky coefficient ( $C_v = 0.2$ ). A 3D view of the waves propagating over the reef is shown in Figure 64. The corresponding BOUSS-2D calculated significant wave height field is shown in Figure 65. We could clearly determine in 3D viewing of the BOUSS-2D simulations that waves shoal and break on the reef face, and then they propagate over the reef flat as steep, asymmetric cnoidal-type bores.

Table 8. Summary of selected storm events for Ipan simulations.

Storm Event	Day	Time (UTC)	$H_s$ (m)	$T_p$ (sec)	$D_p$ (deg)	Water Level (m)
243	10/19/2005	16:45	2.08	11.1	68	0.073
252	10/19/2005	19:45	1.91	11.1	67	0.264
264	10/19/2005	23:45	2.00	11.8	62	0.689
282	10/20/2005	05:45	2.15	11.8	71	0.511
294	10/20/2005	09:45	1.85	12.5	75	0.708
306	10/20/2005	13:45	1.92	11.1	71	0.363
318	10/20/2005	17:45	1.77	11.1	68	0.04

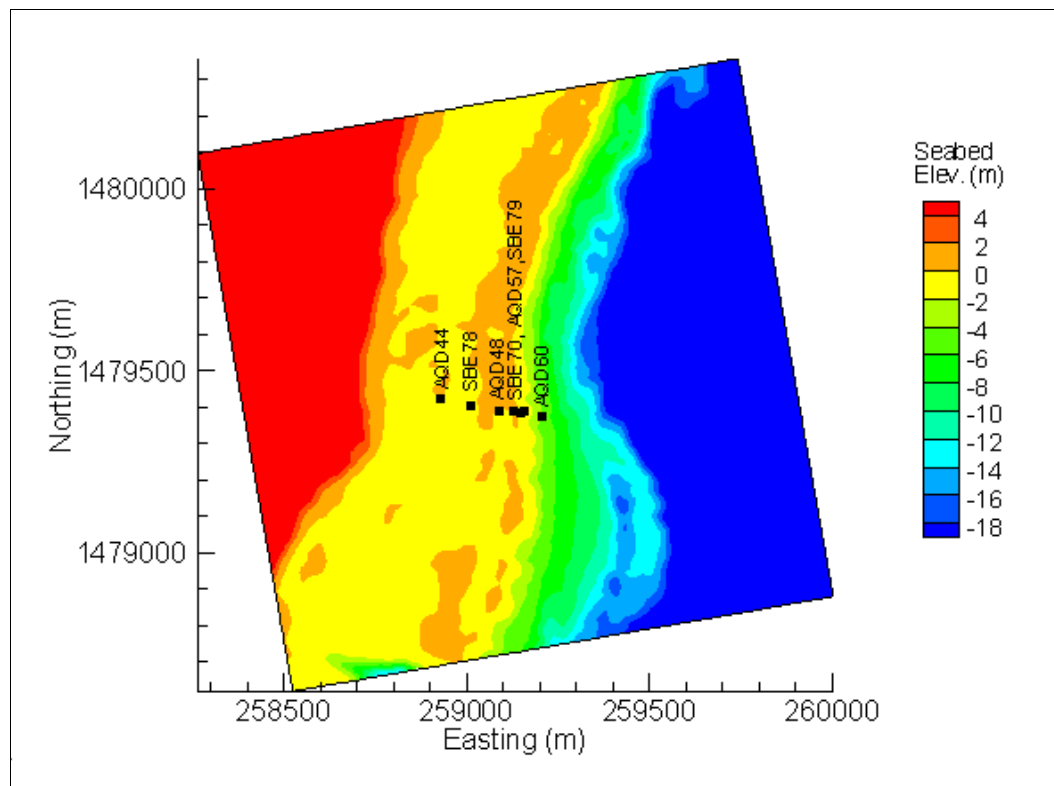


Figure 63. Two-dimensional map of reef bathymetry near Ipan, Guam, used in BOUSS-2D model simulations.

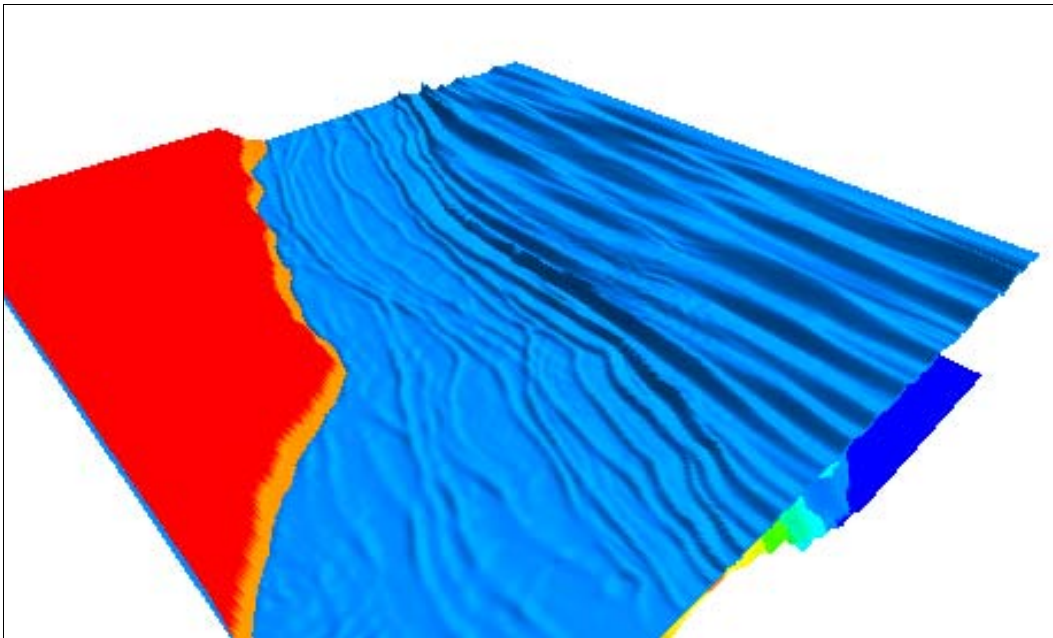


Figure 64. Three-dimensional view of waves from BOUSS-2D simulation propagating over Ipan reef for Storm Event 264 ( $H_s = 2$  m,  $T_p = 12$  sec, WL = 0.7 m).

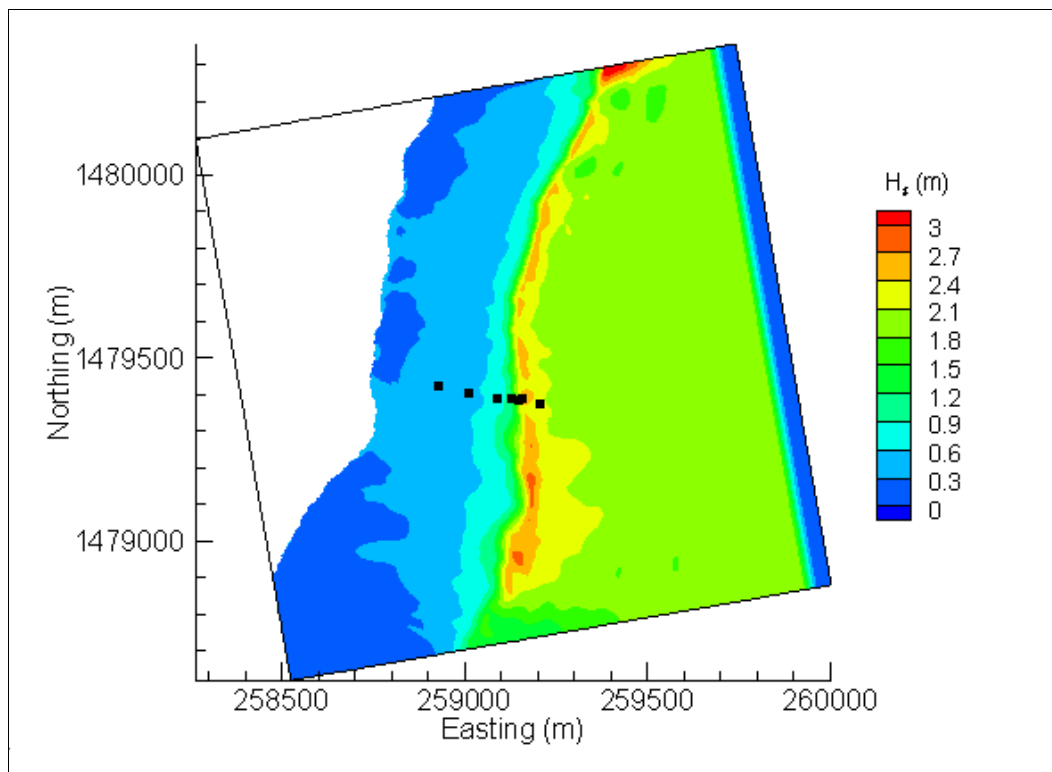


Figure 65. Predicted significant wave height field from BOUSS-2D simulation for Storm Event 264 ( $H_s = 2.0$  m,  $T_p = 11.8$  sec, WL = 0.69 m).

The measured and BOUSS-2D computed significant wave height variation along instrumentation transect are compared in Figure 66 for Storm Event 264 (WL = 0.69 m) for different bottom friction coefficients. The use of the Chezy value  $C_f = 20$  ( $f_w = 0.05$ ) leads to an overestimation the height over the reef flat while  $C_f = 10$  ( $f_w = 0.2$ ) underestimates the height. Plots of the significant wave height distribution give an overall view of the wave energy transformation across the reef but do not show the wave energy distribution in the frequency domain. Hence, we also compared the spectral densities of the measured and predicted surface elevation time-histories at the four AQD profiler locations in Figure 67. The use of  $C_f = 20$  provided a good match of the infragravity wave energy over the reef flat (AQD 48 and AQD 44) but overestimated the wave energy in the wind-wave frequency band. Decreasing the bottom friction coefficient to  $C_f = 10$  led to an excessive dissipation of the infragravity wave energy.

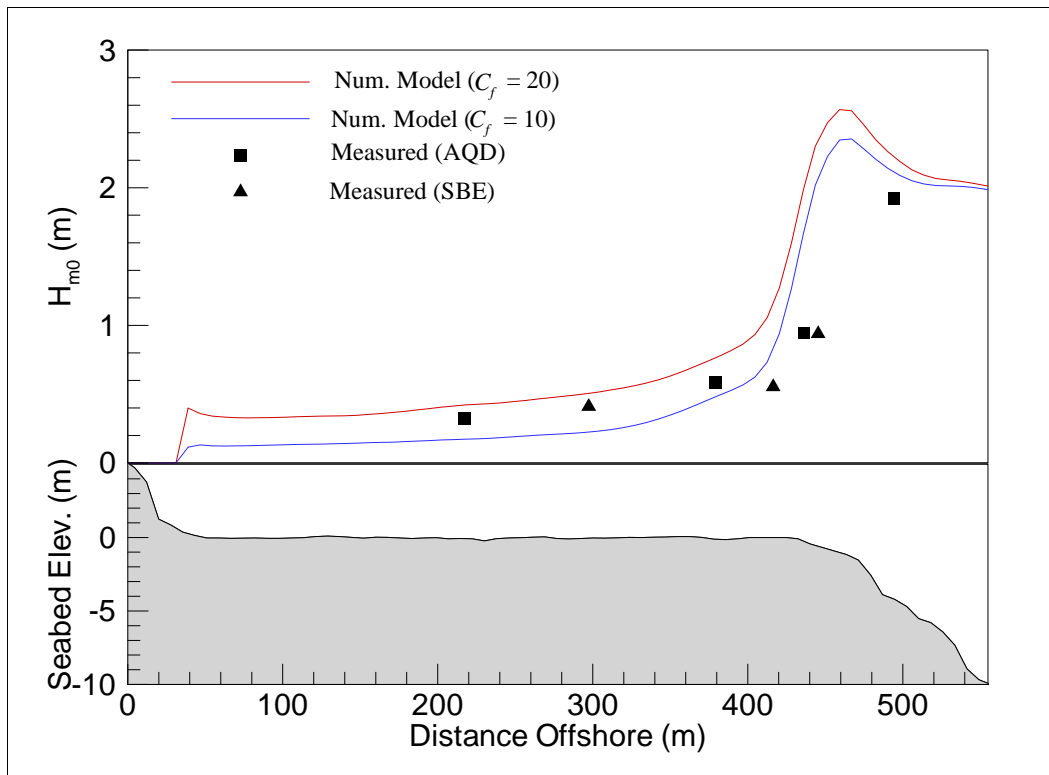


Figure 66. Computed and measured significant wave height variation along transect for Storm Event 264 (WL = 0.69 m) for different bottom friction coefficients.

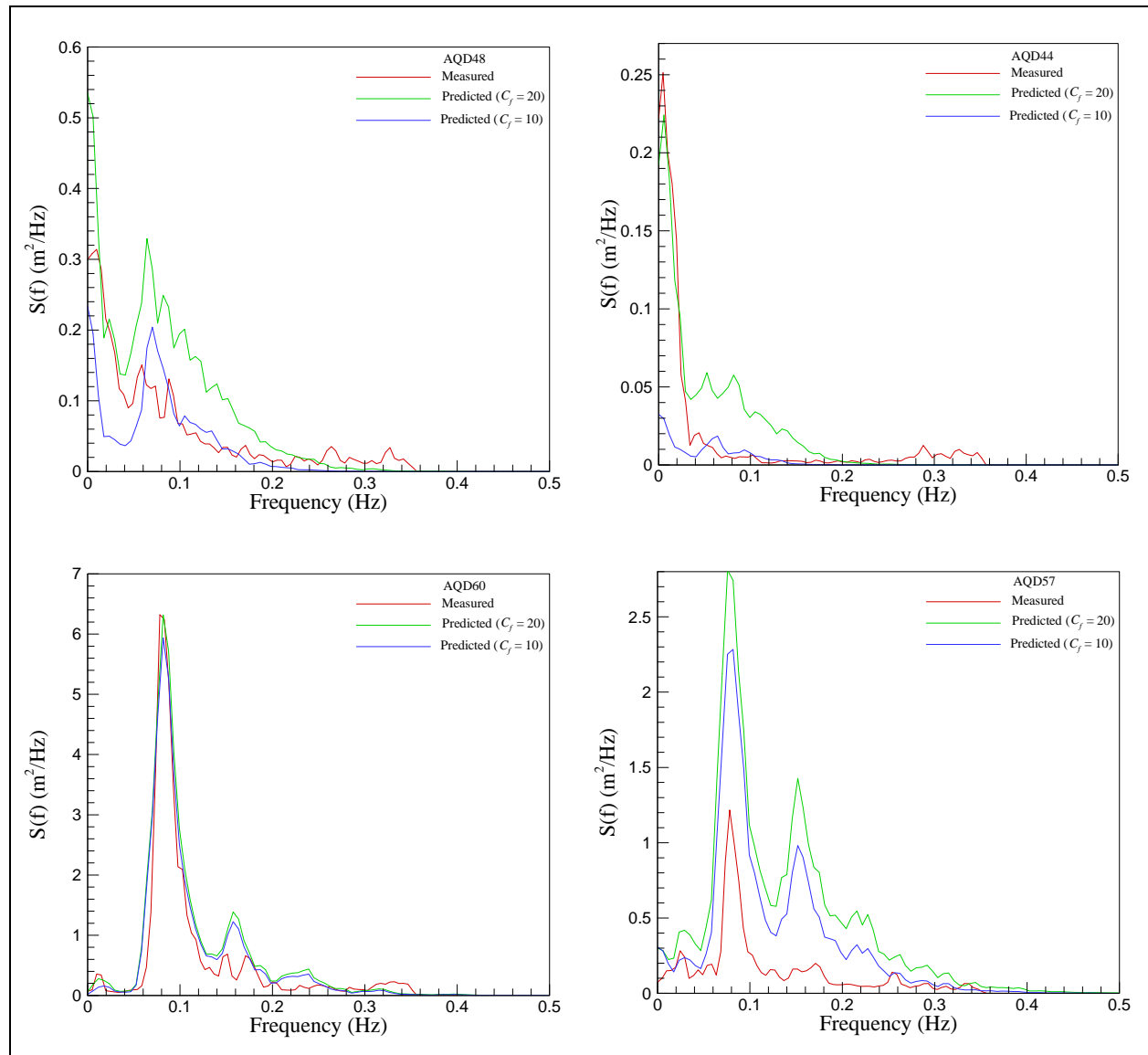


Figure 67. Measured and predicted wave spectra for Storm Event 264, different values of bottom friction coefficient.

We would also like to point out that AQD 57 is located in the surf zone, where there is a rapid decay in wave height. Errors in the gauge location of the order of 10 m could lead to significantly different wave heights and spectral densities. We illustrate this by moving the location of the AQD 57 gauge 15 m shoreward in the numerical model, which leads to a much better match between the model predictions and the field data as shown in Figure 68. *Therefore, a minor error in the location of gauges or the bathymetry may also cause some substantial differences between model and data, and such errors can produce large mismatch between model-data.*

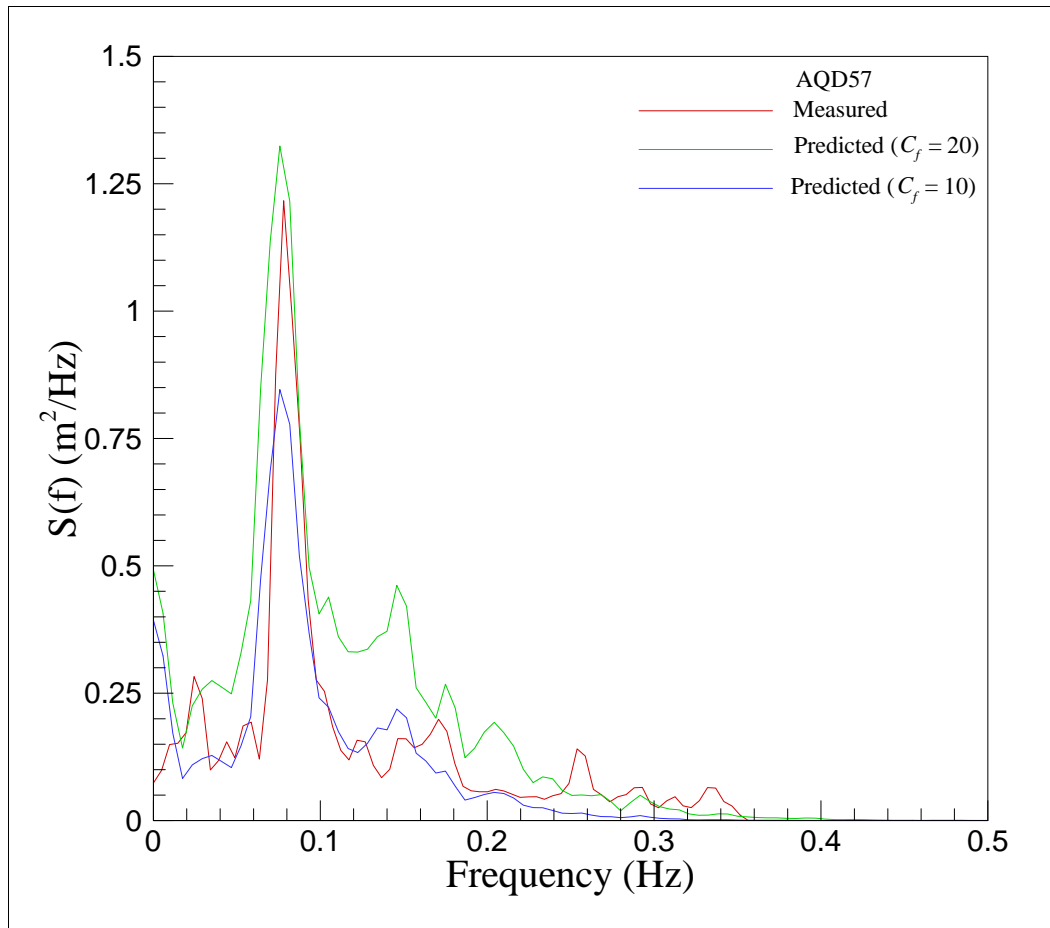


Figure 68. Measured and predicted wave spectra for Storm Event 264 at AQD 57 with numerical gauge location moved 15 m shoreward.

Based on previous experience with the Mokuleia field data, we decided to use the Smagorinsky eddy-viscosity coefficient to simulate wave energy dissipation over rough surfaces with characteristic roughness scales of the order of 10 percent of the water depth. We repeated the simulations for the seven selected storm events in Table 8 using a value of bottom friction coefficient  $C_f = 20$  and two values for the Smagorinsky coefficients.  $C_v = 0.5$  and  $1.0$ . The spatial distribution of the predicted significant wave height for Storm Event 264 is shown in Figure 69. For results shown in Figure 69, values of  $C_f = 20$  and  $C_v = 1.0$  were used. The significant wave height variation for the seven storm events are plotted in Figures 70 to 76 along the instrumentation transects. As shown in Figure 76, there was good agreement between the measured and predicted wave heights over the reef flat with the use of  $C_v = 0.5$ , including for an extreme low water level event with a still-water level of 4 cm over the reef flat.

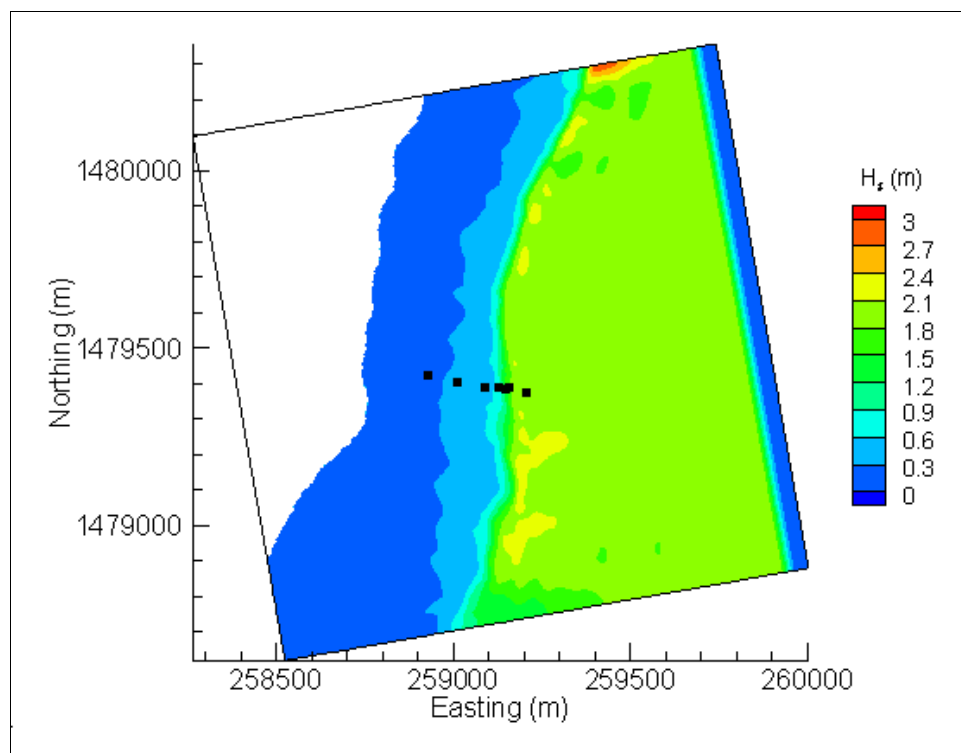


Figure 69. Predicted significant wave height distribution for Storm Event 264 ( $H_s = 2.0$  m,  $T_p = 11.8$  sec,  $WL = 0.69$  m,  $C_r = 20$ , and  $C_v = 1.0$ ).

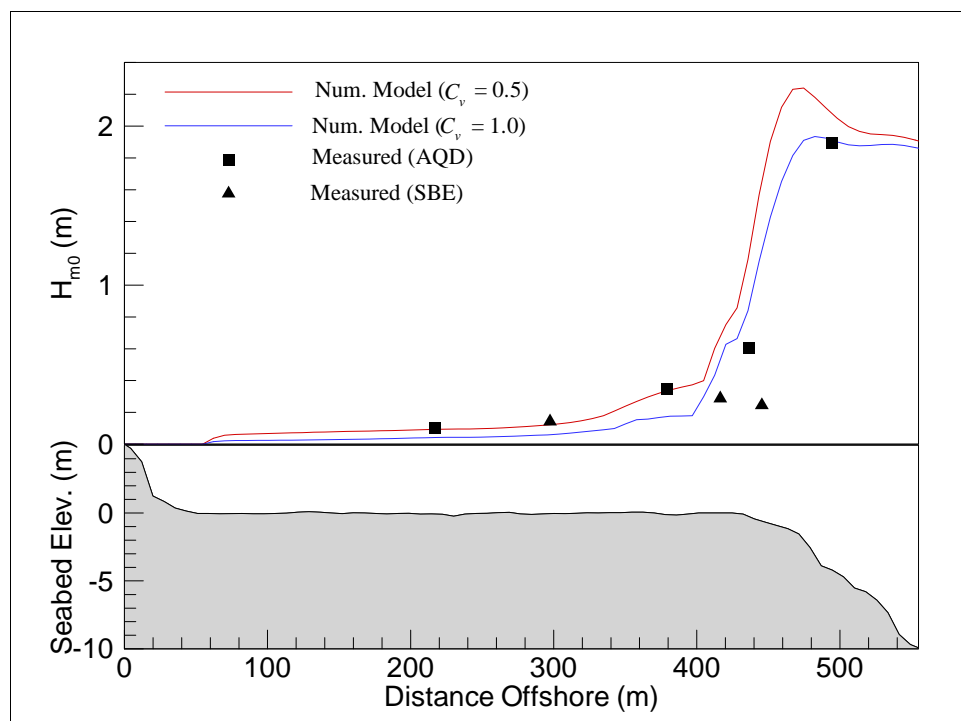


Figure 70. Computed and measured significant wave height variation along transect for Storm Event 243 ( $H_s = 2.08$  m,  $T_p = 11.1$  sec,  $WL = 0.073$  m).



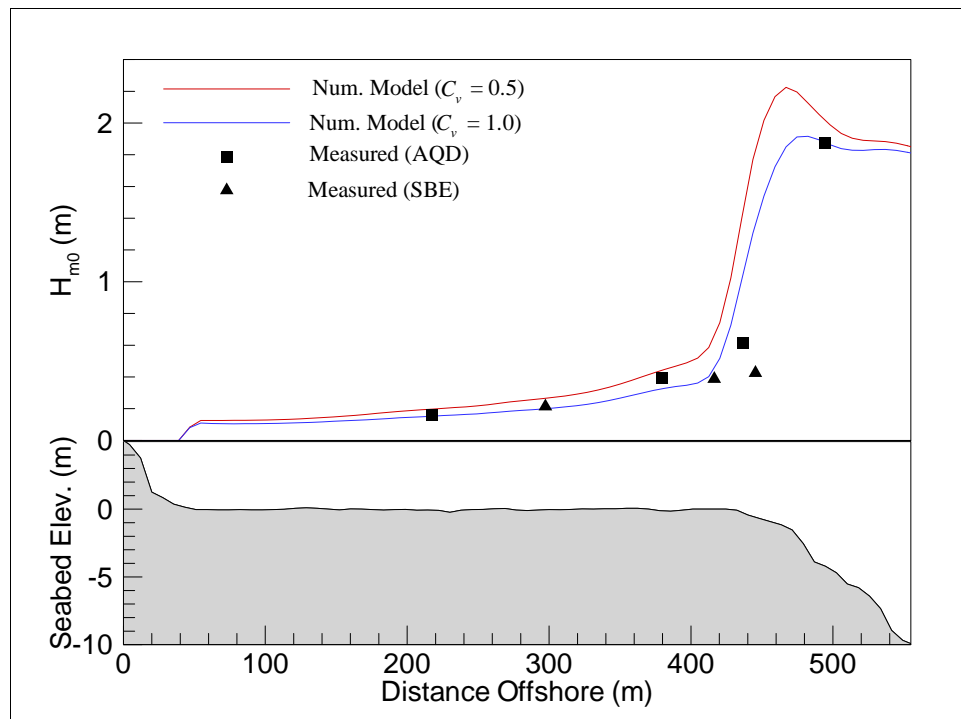


Figure 71. Computed and measured significant wave height variation along transect for Storm Event 252 ( $H_s = 1.91$  m,  $T_p = 11.1$  sec,  $WL = 0.264$  m).

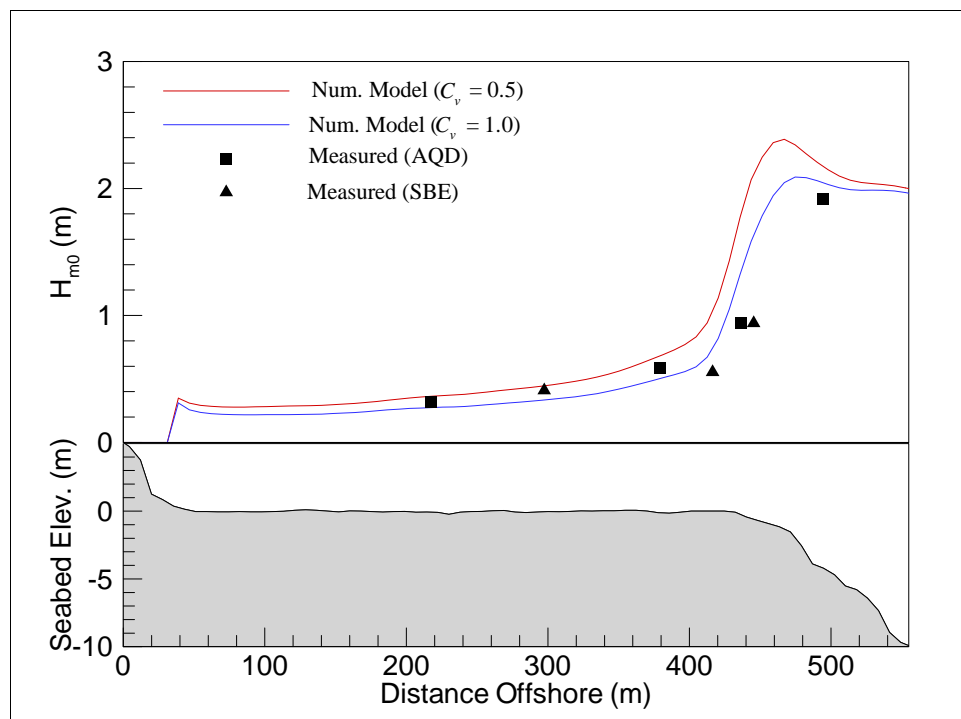


Figure 72. Computed and measured significant wave height variation along transect for Storm Event 264 ( $H_s = 2.0$  m,  $T_p = 11.8$  sec,  $WL = 0.69$  m,  $C_r = 20$ ).

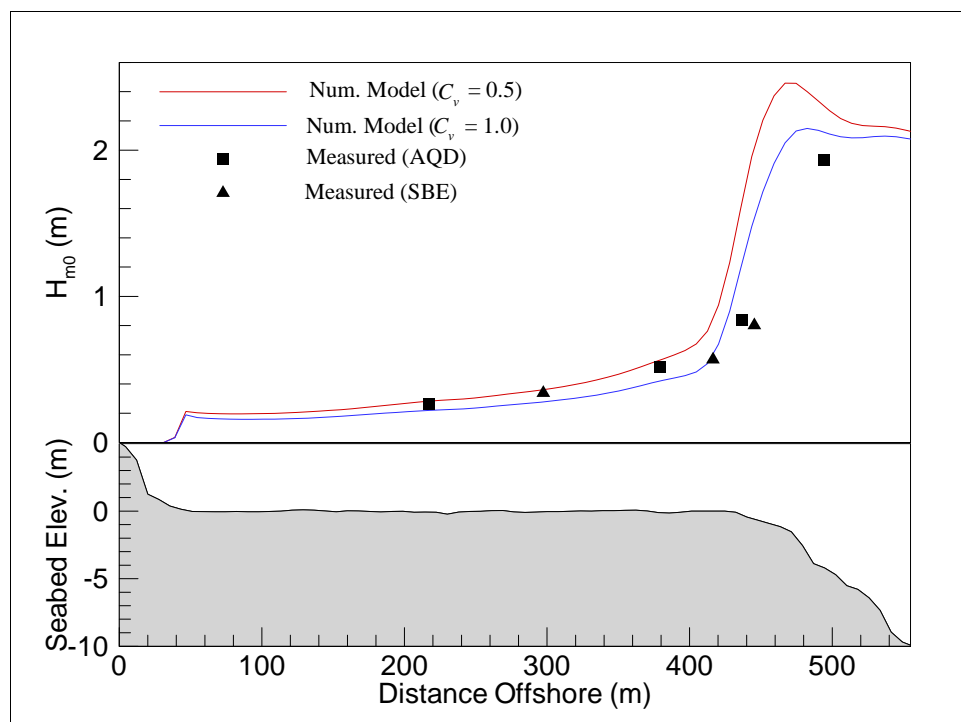


Figure 73. Computed and measured significant wave height variation along transect for Storm Event 282 ( $H_s = 2.15$  m,  $T_p = 11.8$  sec,  $WL = 0.51$  m,  $C_r = 20$ ).

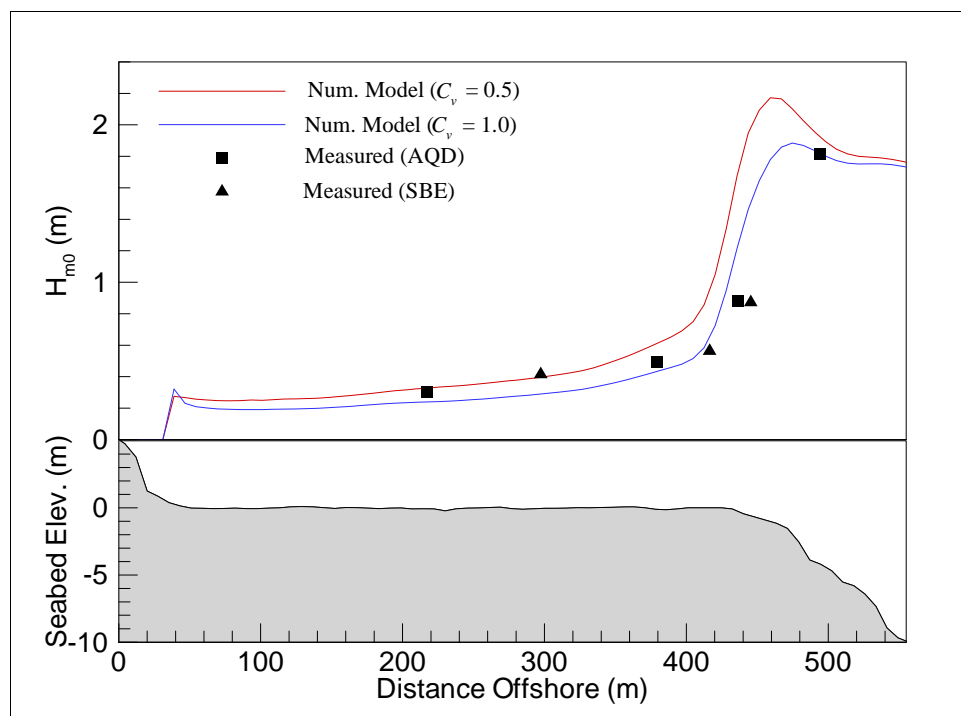


Figure 74. Computed and measured significant wave height variation along transect for Storm Event 294 ( $H_s = 1.85$  m,  $T_p = 12.5$  sec,  $WL = 0.71$  m,  $C_r = 20$ ).

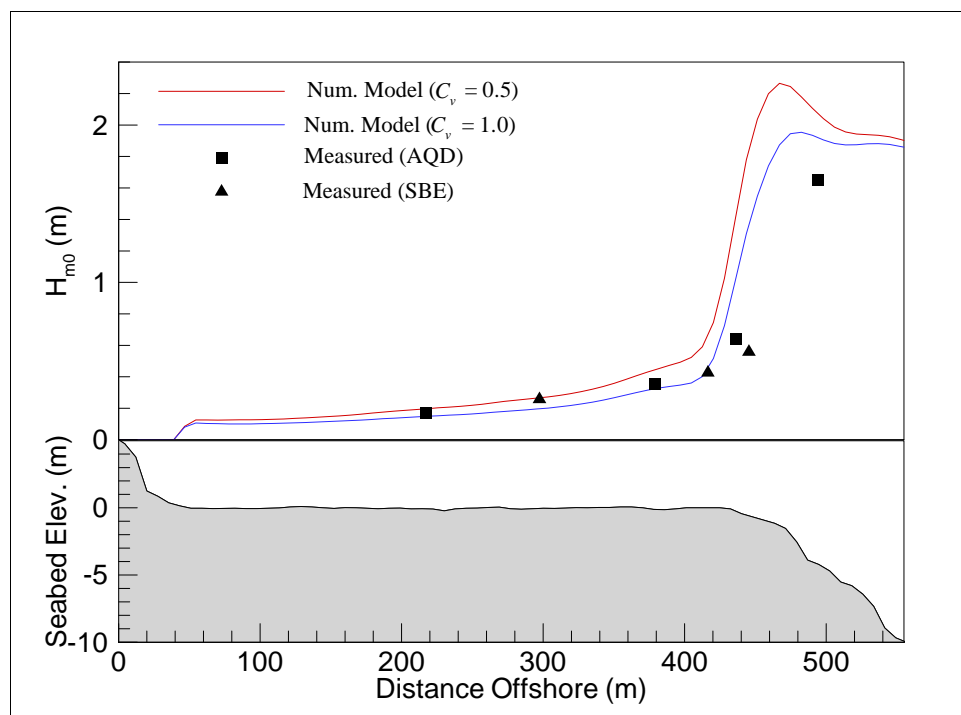


Figure 75. Computed and measured significant wave height variation along transect for Storm Event 306 ( $H_s = 1.92$  m,  $T_p = 11.1$  sec, WL = 0.36 m,  $C_r=20$ ).

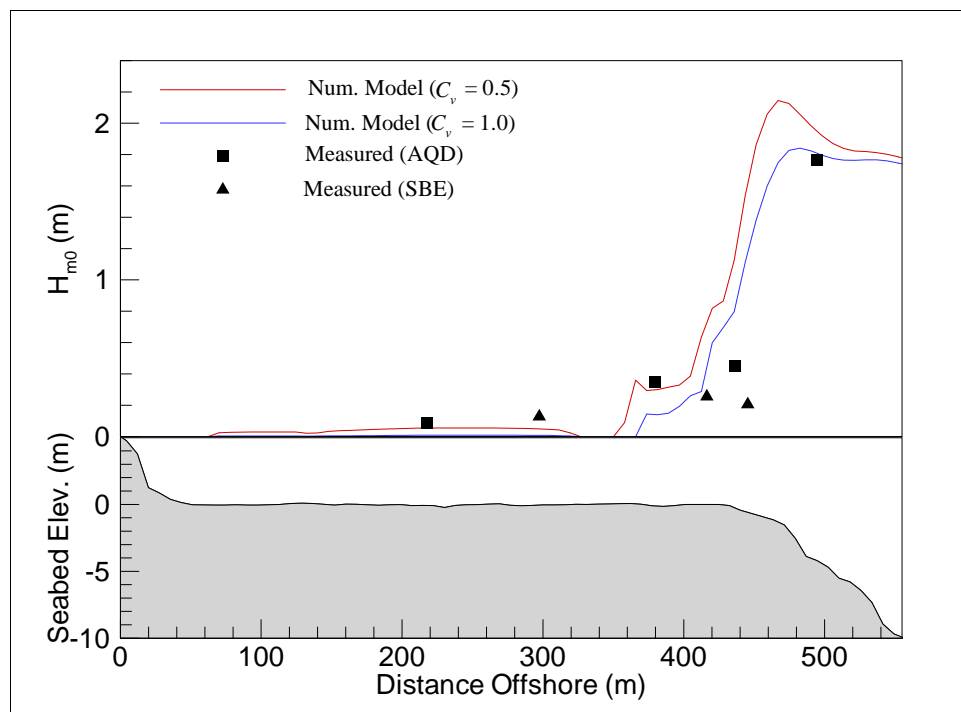


Figure 76. Computed and measured significant wave height variation along transect for Storm Event 318 ( $H_s = 1.77$  m,  $T_p = 11.1$  sec, WL = 0.04 m).

As shown in Figures 70, 71, and 76, we also note that for several of the low water level events, the SBE pressure gauges in the wave breaking zone recorded consistently much lower wave heights than the AQD current profilers. Since the nearshore SBE gauge also recorded lower than expected wave heights during the Mokuleia field experiments, this raises questions about the performance of these sensors under breaking waves. Additional investigation of this matter is warranted by field data collection teams through comparison of field data collected with the SBE gauges both in Guam and Hawaii to data obtained with other types of sensors. This comparison must consider different measurement conditions (i.e., low and high water level, large and small waves, and breaking and non-breaking surf zone waves).

The measured and predicted spectral densities at the AQD gauge locations are plotted in Figures 77 and 78 for a high water event (Storm Event 264, WL = 0.69 m) and low water event (Storm Event 243, WL = 0.073 m). Compared to the quadratic bottom friction only case (Figure 67), it is obvious can see that in this case the eddy-viscosity parameterization leads to a stronger dissipation of the high-frequency wave energy. However, the numerical model still overpredicts the wave energy in the incident-wave frequency band for the high-water level case. For the low water level case, good agreement was obtained between the measured and predicted wave spectra over the reef flat.

Additional results are provided in Appendix C for seven storm events for Guam field experiments. These results include measured and calculated wave heights at locations of the Aquadopp current profilers and Sea Bird Electronics gauges. As can be seen from Tables C1 through C3, AQD and SBE instruments have reported similar wave height values when depths at the location of these gauges were deep. For the first two gauges in deep water, the maximum difference between measured and calculated wave heights is 39 percent for AQD44 and 61 percent for SBE78. As water depth decreases, the difference for AQD profilers remains practically constant; while it increases for SBE gauges in shallower depths, becoming nearly 10 times larger. The cause of this radical change, specific to SBE gauges located in the breaker and surf zone, is unknown. As was reported earlier, similar performance issues were also noted for SBE gauges in the Hawaii field study.

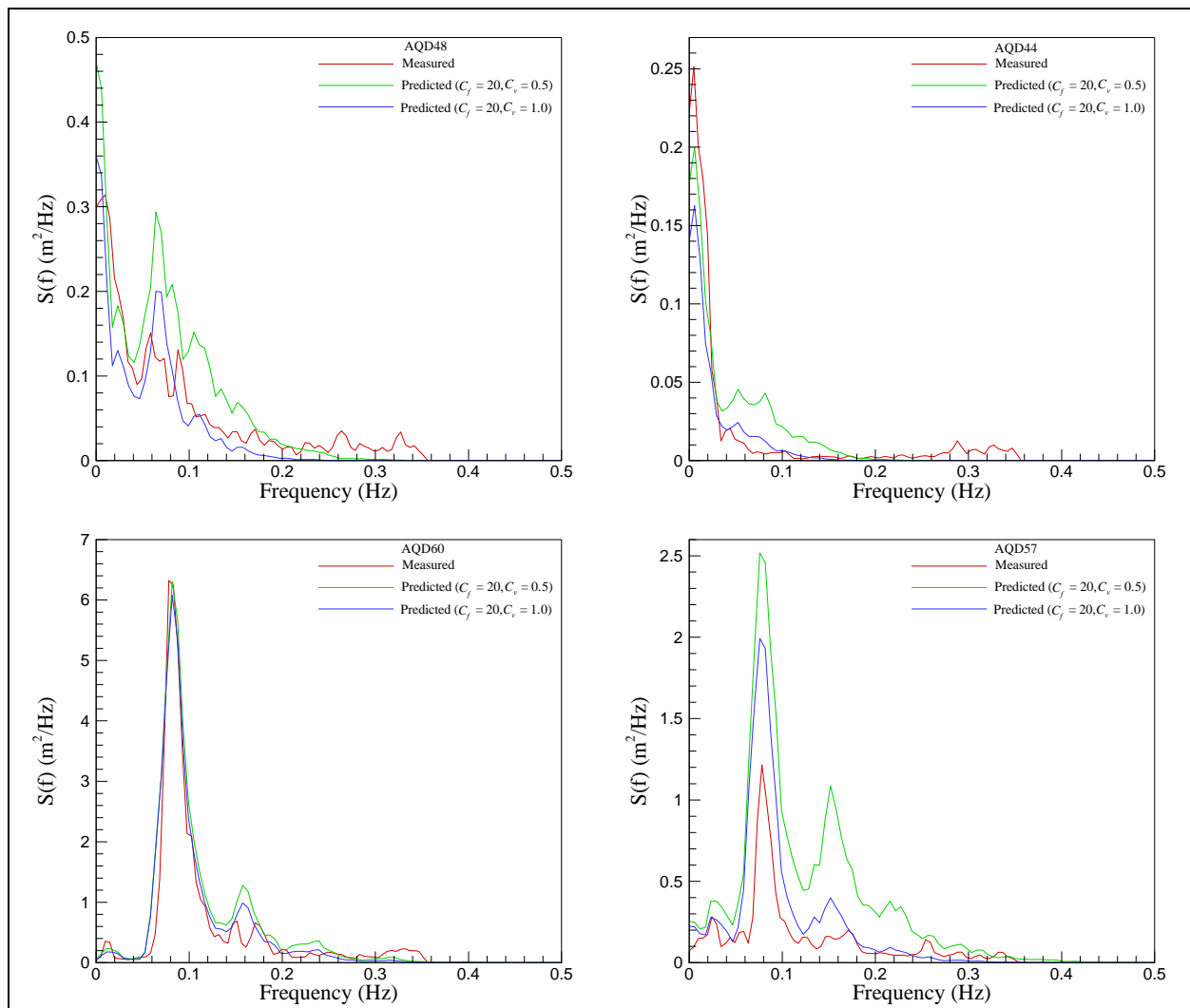


Figure 77. Measured and predicted wave spectra for Storm Event 243 with Smagorinsky dissipation.

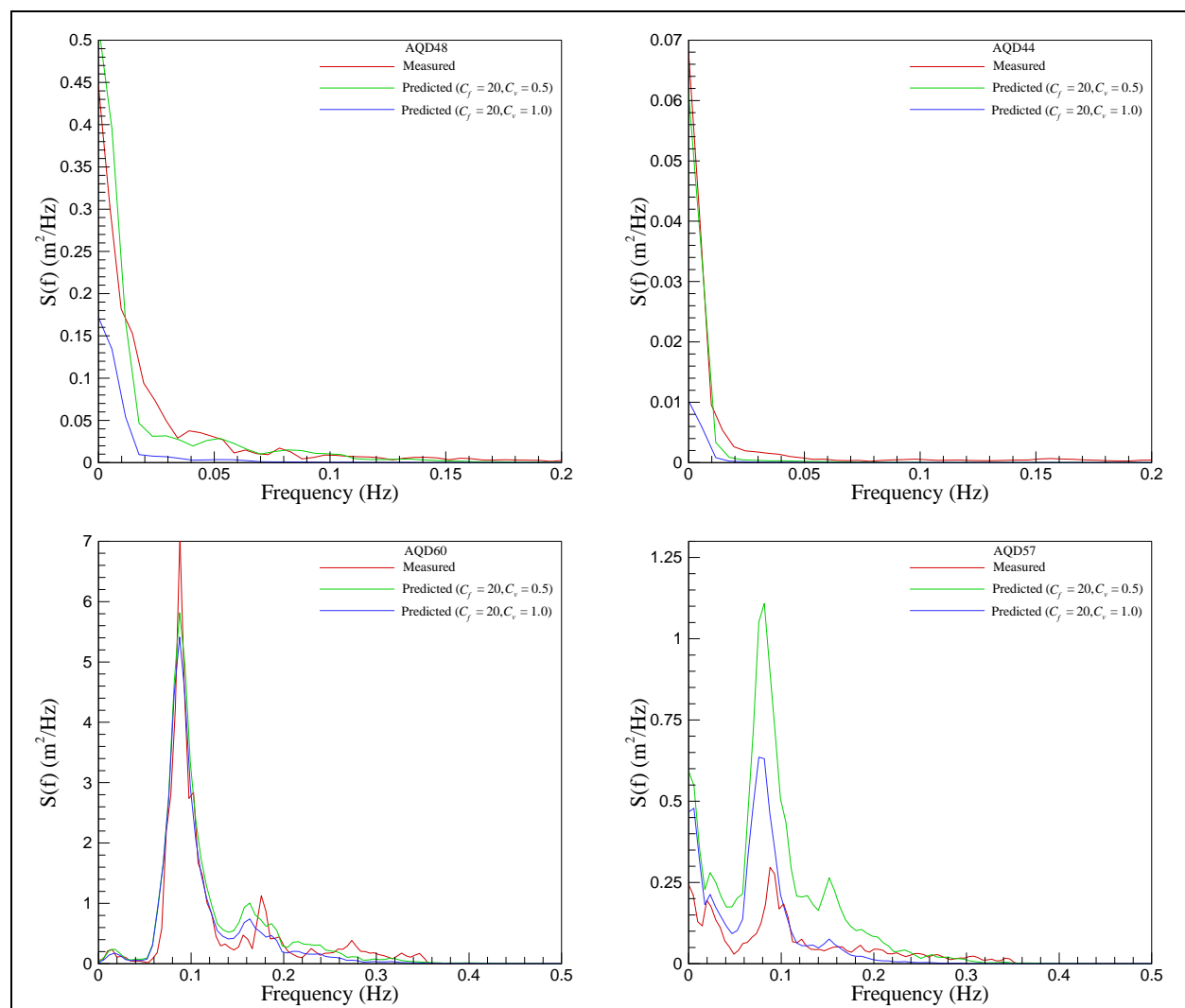


Figure 78. Measured and predicted wave spectra for Storm Event 264 with Smagorinsky dissipation.

## 7 Conclusions and Recommendations

Ocean waves propagating over coral reef systems undergo significant transformations due to nonlinear steepening and cross-spectral transfer of energy to infragravity modes, wave breaking and breaking-induced currents, and wave energy dissipation over rough coral reef bottoms. Most wave models assume an inviscid fluid and parameterize viscous processes such as wave breaking and bottom friction. This report details an investigation into the ability of BOUSS-2D, a Boussinesq-type wave model, to describe wave propagation and runup over complex fringing coral reef systems. In this comprehensive study, numerical as well as laboratory and field experiments have been used to understand and quantify various wave transformation processes over reefs of Guam and Hawaii.

This investigation revealed a number of complex features of wave propagation processes over the reef systems at Guam and Hawaii. First, BOUSS-2D model simulations revealed that due to the low water level over reef flats and strong nonlinearities in shallow water, the low-frequency (long-period) oscillations that occur over reefs at certain water levels could turn into bore-like surges. These surges are characterized by rather steep forward faces observed in the model simulations. The bore-like surges are capable of propagating over long distances without change in form, causing inundation to the land-based property and endangering the safety of humans living along coasts of islands.

Second, BOUSS-2D model was able to represent the resonant amplification of the long-period oscillations over long horizontal widths and varying beds of Guam and Hawaii reefs caused by the wave grouping of incident short-period waves. This was confirmed by nonlinear numerical experiments based on Boussinesq-type wave equations that compared very well both with laboratory measurements and also to field data for a range of incident wave conditions propagating over different reef geometries. Third, BOUSS-2D model also successfully captured the time variations in the location of breaking point and long-period sea surface elevation along the reefs for different incident waves.

It is also found that numerical model predictions of the post-breaking wave heights and setup over the reef flat, as well as runup on the beach, were sensitive to the parameterization of the wave breaking and bottom friction processes. For the laboratory experiments, the model-data comparisons suggest the use of a water depth-dependent friction coefficient. For the field experiments, these results revealed that the commonly used quadratic drag-law for bottom friction could not adequately describe frequency-dependent changes to the wave spectrum over the reef flat. The drag-law formulation led to an excessive dissipation of the infragravity wave energy relative to the incident wave frequency band.

We tested a new formulation for wave energy dissipation over rough coral reef bottoms. The formulation is based on the assumption that the thickness of turbulent boundary layers over rough reefs is no longer small but rather permeates the entire water column. The effect of turbulence is thus represented by a body force characterized by an eddy viscosity coefficient instead of an applied shear stress at the bottom of the water column. We were able to obtain an improved match with the field data by using the Smagorinsky approach to represent the eddy viscosity. The eddy viscosity term preferentially dissipates the higher-frequency energy as observed in the field data. The eddy-viscosity formulation of wave dissipation over fringing reefs was successful for both Guam and Hawaii sites. However, additional work is required to relate the eddy-viscosity coefficient to the characteristic height and length scales of the bottom roughness. It may also be important to include the effect of reef porosity in field applications since most coral reefs are relatively porous.

We have developed estimates of the maximum wave height, mean sea-surface elevation change (setup) and runup for four different types of reefs studied with laboratory and field experiments. This research has shown that calculated wave heights alone are not sufficient to quantify the complex wave processes occurring over reefs. Even if predicted wave height values were correct, other wave processes such as wave setup and runup may not be estimated correctly. It is imperative that wave studies over reefs consider the spectral evolution to ensure nonlinear wave transfer mechanisms are accurately captured by the numerical wave model used.

Lastly, it is noted potential problems with some of the sensors used in the field experiments. Coral reefs present a challenging environment for most sensors due to the low water levels, frequent wave breaking events, and the



breaking-induced turbulence in the water column. At low water levels, SBEs appeared to be in and out of water, and the intermittent submergence seemed to have affected the reliability of measurements. It would be prudent in future reef field experiments to conduct comparative studies to ascertain the limitations and accuracy of the different types of sensors.

## References

- Asmar, W. E., and O. G. Nwogu. 2006. Finite volume solution of Boussinesq-type equations on an unstructured grid. *Proceedings of the ICCE'06*, Vol 1. San Diego, CA, 73-85.
- Battjes, J. A., and J. P. F. M. Janssen. 1978. Energy loss and set-up due to breaking of random waves. *Proceedings 16th International Conference on Coastal Engineering*, ASCE, 569-587.
- Brander, R. W., P. S. Kench, and D. Hart. 2004. Spatial and temporal variations in wave characteristics across a reef platform, Warraber Island, Torres Strait, Australia. *Marine Geology* 207:169-184.
- Demirbilek, Z., O. G. Nwogu, and D. L. Ward. 2007. *Laboratory study of wind effect on runup over fringing reefs, Report 1: Data report*. Coastal and Hydraulics Laboratory Technical Report ERDC/CHL-TR-07-4. Vicksburg, MS: U.S. Army Engineer Research and Development Center.
- Demirbilek, Z., A. Zundel, and O. Nwogu. 2005a. *BOUSS-2D wave model in the SMS: I. Graphical interface*. Coastal and Hydraulics Laboratory Technical Note CHETN-I-69. Vicksburg, MS: U.S. Army Engineer Research and Development Center.
- Demirbilek, Z., A. Zundel, and O. Nwogu. 2005b. *BOUSS-2D wave model in SMS: II. Tutorial with examples*. Coastal and Hydraulics Laboratory Technical Note CHETN-I-70. Vicksburg, MS: U.S. Army Engineer Research and Development Center.
- Fredsoe, J., and R. Deigard. 1992. *Mechanics of coastal sediment transport (advanced series in ocean engineering)*. Teaneck, NJ: World Scientific Publishing Co.
- Garnier, J., and A. Nachbin. 2006. Eddy viscosity for gravity waves propagating over turbulent surfaces. *Physics of Fluids* 18:1-11.
- Gerritsen, F. 1980. Wave attenuation and wave set-up on a coastal reef. *Proceedings 17th International Conference on Coastal Engineering*, Sydney, Australia. New York, NY: ASCE, 444-461.
- Gourlay, M. R. 1996. Wave set-up on coral reefs. 1. Set-up and wave-generated flow on an idealized two dimensional horizontal reef. *Coastal Engineering* 27:161-193.
- Headquarters, U.S. Army Corps of Engineers. 2002. *Coastal engineering manual*. EM 1110-2-1100. Washington, DC: U.S. Army Corps of Engineers (in 6 volumes).
- Kamphuis, J. W. 1975. Friction factor under oscillatory waves. *Journal of Waterways, Harbors, Coastal Engineering Division* 101:135-144, ASCE.
- Kennedy, A. B., Q. Chen, J. T. Kirby, and R. A. Dalrymple. 2005. Boussinesq modeling of wave transformation, breaking, and runup. I: 1D. *Journal of Waterway, Port, Coastal and Ocean Engineering* 126:39-47, ASCE.

- Jaffe, B. E., and B. M. Richmond. 1993. Overwash variability on the shoreline of Guam during Typhoon Russ. *Proceedings Seventh International Coral Reef Symposium*, Vol. 1, Guam, 257-264.
- Lee, T. T., and K. P. Black. 1978. The energy spectra of surf waves on a coral reef. *Proceedings 16th International Conference on Coastal Engineering*, Hamburg, Germany. New York: ASCE, 588-608.
- Longuet-Higgins, M. S., and R. W. Stewart. 1964. Radiation stress in water waves: A physical discussion with applications. *Deep Sea Research* 11:529-562.
- Lowe, R. J., J. L. Falter, M. D. Bandet, G. Pawlak, M. J. Atkinson, S. G. Monismith, and J. R. Koseff. 2005. Spectral wave dissipation over a barrier reef. *Journal of Geophysical Research* 110, C04001, doi:10.1029/2004JC002711.
- Lugo-Fernandez, A., H. H. Roberts, and J. N. Suhayda. 1998. Wave transformation across a Caribbean fringing-barrier coral reef. *Continental Shelf Research* 18:1,099-1,124.
- Massel, S. R., and M. R. Gurlay. 2000. On the modelling of wave breaking and set-up on coral reefs. *Coastal Engineering* 39:1-27.
- Nakaza, E., and M. Hino. 1990. Bore-like surf beat in a reef zone caused by wave groups of incident short period waves. *Fluid Dynamics Research* 7:89-100.
- Nakaza, E, S. Tsukayama, and M. Hino. 1990. Bore-like surf beat on reefs. *Proceedings 22nd International Conference on Coastal Engineering*. Delft: The Netherlands, 743-756.
- Nelson, R. C. 1996. Hydraulic roughness of coral reef platforms. *Applied Ocean Research* 18:265-274.
- Nwogu, O. 1989. Maximum entropy estimation of directional wave spectra from an array of wave probes. *Journal of Applied Ocean Research* 11(4):176-182.
- Nwogu, O. 1993a. On the generation of infragravity waves by shoaling multi-directional waves. *Proceedings of the Second International Symposium on Ocean Wave Measurement and Analysis, WAVES '93*, New Orleans, 1-14.
- Nwogu, O. 1993b. Alternative form of Boussinesq equations for nearshore wave propagation. *Journal of Waterway, Port, Coastal and Ocean Engineering* 119(6):618-638, ASCE.
- Nwogu, O. G. 1996. Numerical prediction of breaking waves and currents with a Boussinesq model. *Proceedings 25th International Conference on Coastal Engineering* 4:4,807-4,820.
- Nwogu, O., and Z. Demirbilek. 2001. *BOUSS-2D: A Boussinesq wave model for coastal regions and harbors*. ERDC/CHL TR-01-25. Vicksburg, MS: U.S. Army Engineer Research and Development Center.
- Nwogu, O. G., and Z. Demirbilek. 2007. Numerical simulation of wave runup and overtopping with Boussinesq-type equations. (accepted for publication in *Coastal Engineering*).

- Nwogu, O. G., and Z. Demirbilek. 2006. Nonlinear wave interaction with submerged and surface-piercing porous structures. *Proceedings of the ICCE '06*, Vol. 1. San Diego, CA, 287-299.
- Ogg, J. G., and J. A. Koslow. 1978. The impact of typhoon Pamela, 1976, on Guam's coral reefs and beaches. *Pacific Science* 32:105-118.
- Roberts, H. H. 1975. Physical processes in a fringing reef system. *Journal of Marine Research* 33:233-260.
- Seelig, W. 1983. Laboratory study of reef-lagoon system hydraulics. *Journal of Waterway, Port, Coastal and Ocean Engineering* 109:380-391.
- Shore protection manual*. 1984. 4th ed., 2 Vol, U.S. Army Engineer Waterways Experiment Station. Washington, DC: U.S. Government Printing Office.
- Symonds, G., K. P. Black, and I. R. Young. 1995. Wave-driven flow over shallow reefs. *Journal of Geophysical Research* 100:2,639-2,648.
- Smagorinsky, J. 1963. General circulation experiments with the primitive equations. *Monthly Weather Review* 91:99-164.
- Tait, R. J. 1972. Wave setup on coral reefs. *Journal of Geophysical Research* 77:2,207-2,211.
- Thompson, E. F. 2005. *A physical model study for investigation of wave processes over reefs*. Coastal and Hydraulics Laboratory unpublished letter report. Vicksburg, MS: U.S. Army Engineer Research and Development Center.

## Appendix A: Comparison of Measured and Calculated Wave Parameters for UM Laboratory Experiments

Table A1. Measured and predicted significant wave height and wave setup at Gauge 1.

Test No.	Measured (m)		Predicted (m)		Difference (%)	
	$H_s$	$\bar{\eta}$	$H_s$	$\bar{\eta}$	$H_s$	$\bar{\eta}$
Test-17	0.083	-0.002	0.078	0.000	6	100
Test-18	0.092	-0.002	0.087	0.000	5	91
Test-20	0.065	-0.002	0.061	0.000	7	102
Test-21	0.088	-0.002	0.084	0.000	5	91
Test-27	0.059	-0.002	0.055	0.000	7	102
Test-29	0.075	-0.003	0.070	0.000	7	99
Test-30	0.082	-0.003	0.078	0.000	5	93
Test-31	0.092	-0.003	0.088	0.000	5	93
Test-36	0.073	-0.003	0.067	0.000	7	99
Test-37	0.082	-0.004	0.077	0.000	5	94
Test-38	0.091	-0.004	0.086	0.000	5	94
Test-46	0.062	-0.004	0.056	0.000	9	101
Test-48	0.079	-0.003	0.074	0.000	7	99
Test-57	0.083	-0.002	0.079	0.000	5	92
Test-58	0.092	-0.003	0.088	0.000	5	93

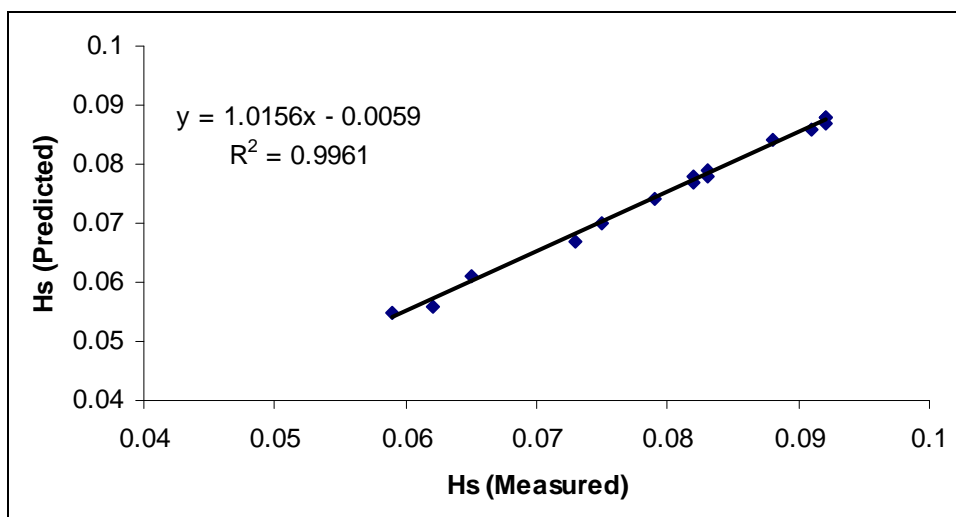


Figure A1. Predicted versus measured significant wave height at Gauge 1.

Table A2. Measured and predicted significant wave height and wave setup at Gauge 2.

Test No.	Measured (m)		Predicted (m)		Difference (%)	
	$H_s$	$\bar{\eta}$	$H_s$	$\bar{\eta}$	$H_s$	$\bar{\eta}$
Test-17	0.078	-0.001	0.078	0.000	0	99
Test-18	0.085	-0.001	0.087	0.000	-2	78
Test-20	0.061	-0.001	0.061	0.000	0	107
Test-21	0.082	-0.001	0.084	0.000	-2	84
Test-27	0.055	-0.001	0.055	0.000	1	103
Tets-29	0.071	-0.002	0.070	0.000	1	99
Test-30	0.076	-0.002	0.078	0.000	-2	89
Test-31	0.085	-0.003	0.088	0.000	-3	91
Test-36	0.068	-0.003	0.068	0.000	1	99
Test-37	0.076	-0.003	0.077	0.000	-2	93
Test-38	0.084	-0.003	0.086	0.000	-3	92
Test-46	0.059	-0.001	0.057	0.000	4	103
Test-48	0.075	-0.001	0.074	0.000	2	98
Test-57	0.077	-0.002	0.079	0.000	-2	88
Test-58	0.085	-0.002	0.088	0.000	-3	88

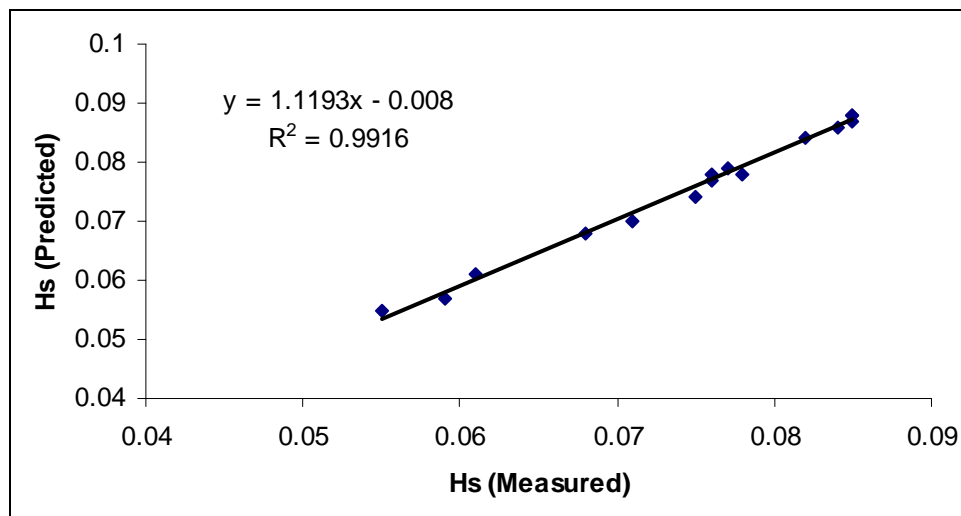


Figure A2. Predicted versus measured significant wave height at Gauge 2.

Table A3. Measured and predicted significant wave height and wave setup at Gauge 3.

Test No.	Measured (m)		Predicted (m)		Difference (%)	
	$H_s$	$\bar{\eta}$	$H_s$		$H_s$	$\bar{\eta}$
Test-17	0.079	-0.001	0.078	0.000	1	98
Test-18	0.084	-0.001	0.086	0.000	-3	80
Test-20	0.060	0.000	0.061	0.000	-1	109
Test-21	0.081	-0.001	0.084	0.000	-3	77
Test-27	0.055	-0.001	0.054	0.000	0	103
Test-29	0.071	-0.002	0.070	0.000	1	99
Test-30	0.075	-0.002	0.077	0.000	-4	89
Test-31	0.082	-0.002	0.087	0.000	-6	90
Test-36	0.068	-0.002	0.068	0.000	1	98
Test-37	0.074	-0.003	0.077	0.000	-4	92
Test-38	0.081	-0.003	0.086	0.000	-5	91
Test-46	0.058	-0.001	0.056	0.000	3	103
Test-48	0.075	-0.002	0.074	0.000	2	98
Test-57	0.076	-0.002	0.078	0.000	-3	88
Test-58	0.084	-0.002	0.087	0.000	-4	89

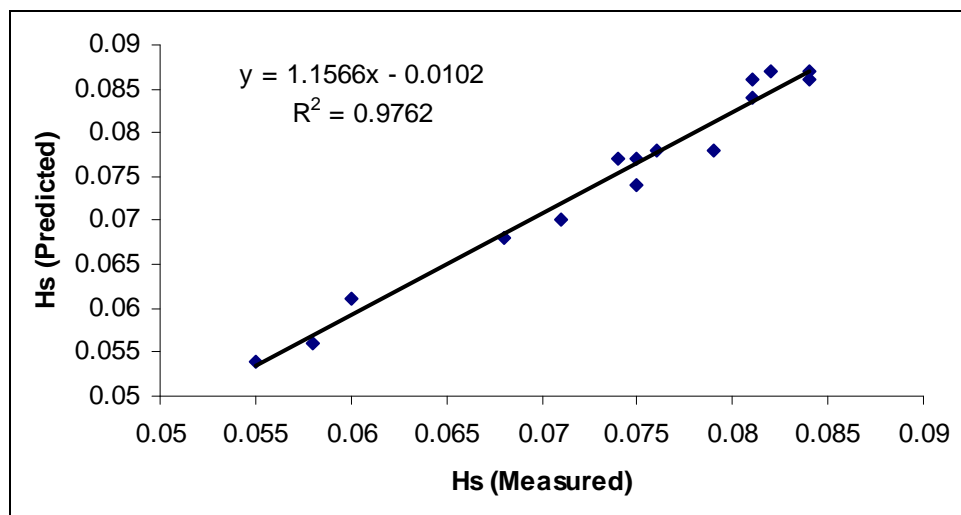


Figure A3. Predicted versus measured significant wave height at Gauge 3.

Table A4. Measured and predicted significant wave height and wave setup at Gauge 5.

Test No.	Measured (m)		Predicted (m)		Difference (%)	
	$H_s$	$\bar{\eta}$	$H_s$		$H_s$	$\bar{\eta}$
Test-17	0.078	-0.002	0.081	-0.001	-3	63
Test-18	0.095	-0.002	0.098	-0.001	-2	73
Test-20	0.058	-0.001	0.059	0.000	-2	67
Test-21	0.087	-0.002	0.090	-0.001	-4	61
Test-21	0.054	-0.002	0.055	0.000	-1	78
Test-29	0.073	-0.003	0.074	-0.001	-1	77
Test-30	0.082	-0.003	0.082	-0.001	0	82
Test-31	0.093	-0.004	0.093	0.000	0	91
Test-36	0.070	-0.003	0.070	-0.001	0	81
Test-37	0.079	-0.004	0.078	0.000	1	92
Test-38	0.089	-0.004	0.087	0.000	2	105
Test-46	0.057	-0.001	0.056	0.000	1	76
Test-48	0.076	-0.002	0.077	-0.001	-1	72
Test-57	0.081	-0.003	0.085	-0.001	-5	75
Test-58	0.092	-0.004	0.096	0.000	-5	87

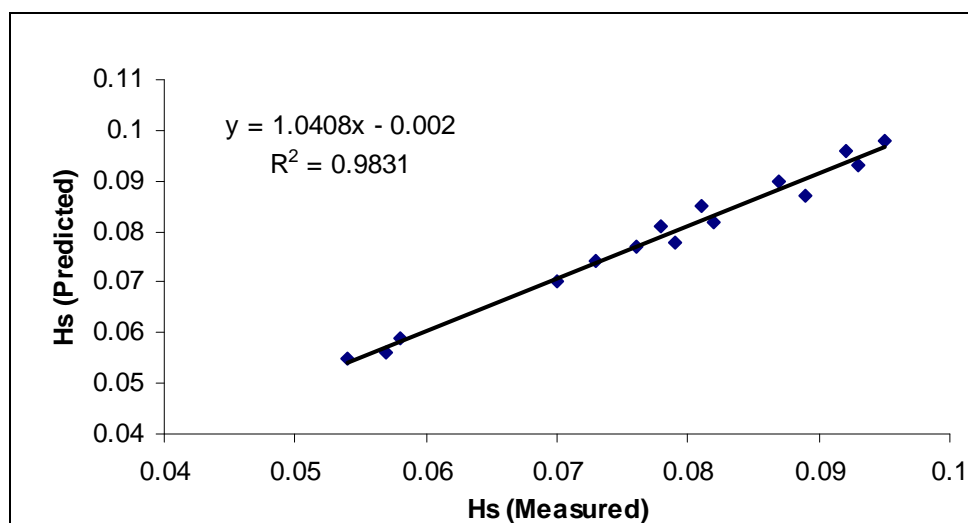


Figure A4. Predicted versus measured significant wave height at Gauge 5.



Table A5. Measured and predicted significant wave height and wave setup at Gauge 6.

Test No.	Measured (m)		Predicted (m)		Difference (%)	
	$H_s$	$\bar{\eta}$	$H_s$		$H_s$	$\bar{\eta}$
Test-17	0.083	-0.002	0.079	-0.001	4	67
Test-18	0.094	-0.003	0.089	0.000	4	86
Test-20	0.063	-0.001	0.062	-0.001	0	59
Test-21	0.088	-0.003	0.085	-0.001	4	72
Test-27	0.057	-0.002	0.055	0.000	4	78
Test-29	0.072	-0.003	0.066	0.000	8	95
Test-30	0.073	-0.003	0.071	0.000	3	109
Test-31	0.077	-0.003	0.077	0.001	0	140
Test-36	0.065	-0.003	0.059	0.000	8	111
Test-37	0.067	-0.003	0.064	0.001	5	153
Test-38	0.069	-0.002	0.068	0.003	1	243
Test-46	0.061	-0.002	0.058	-0.001	4	68
Test-48	0.079	-0.003	0.072	-0.001	8	80
Test-57	0.081	-0.003	0.077	0.000	6	87
Test-58	0.087	-0.003	0.083	0.000	5	111

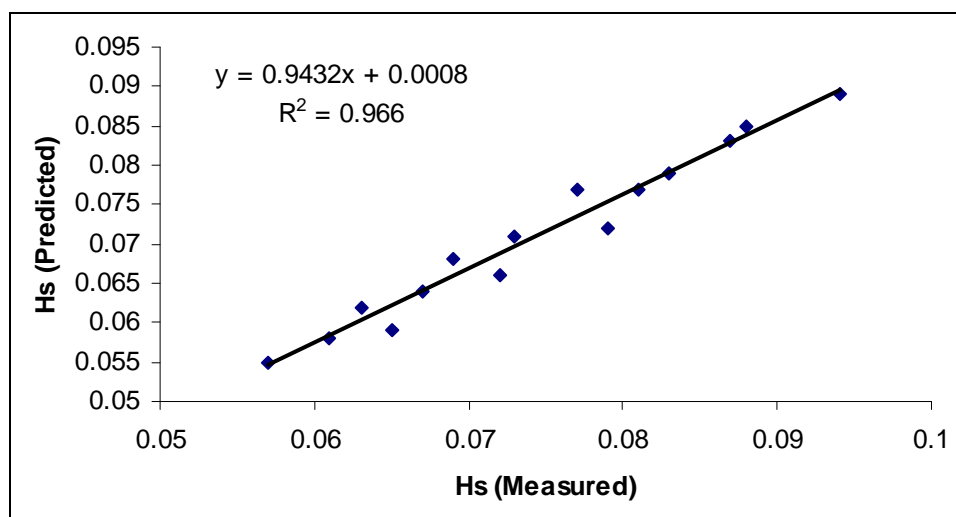


Figure A5. Predicted versus measured significant wave height at Gauge 6.

Table A6. Measured and predicted significant wave height and wave setup at Gauge 7.

Test No.	Measured (m)		Predicted (m)		Difference (%)	
	$H_s$	$\bar{\eta}$	$H_s$		$H_s$	$\bar{\eta}$
Test-17	0.060	0.003	0.062	0.002	-2	37
Test-18	0.070	0.004	0.071	0.004	-1	10
Test-20	0.050	0.002	0.050	0.001	2	59
Test-21	0.066	0.004	0.066	0.003	0	26
Test-27	0.030	0.007	0.027	0.005	8	24
Test-29	0.037	0.010	0.039	0.007	-5	29
Test-30	0.041	0.011	0.041	0.010	-1	8
Test-31	0.045	0.012	0.046	0.013	-2	-2
Test-36	0.027	0.012	0.028	0.013	-2	-11
Test-37	0.031	0.013	0.033	0.015	-6	-16
Test-38	0.034	0.015	0.039	0.018	-13	-17
Test-46	0.043	0.003	0.037	0.003	14	26
Test-48	0.050	0.006	0.046	0.005	9	13
Test-57	0.056	0.007	0.052	0.006	6	19
Test-58	0.061	0.008	0.062	0.007	-2	20

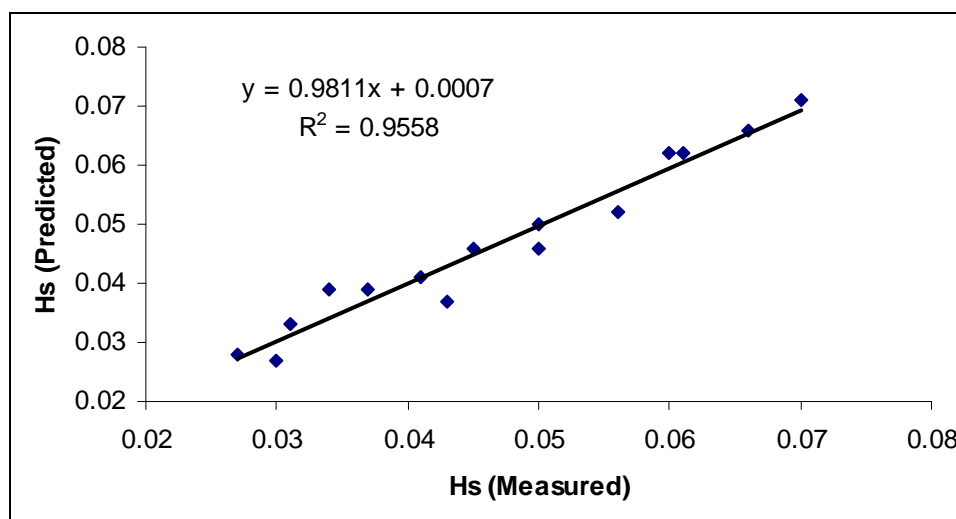


Figure A6. Predicted versus measured significant wave height at Gauge 7.

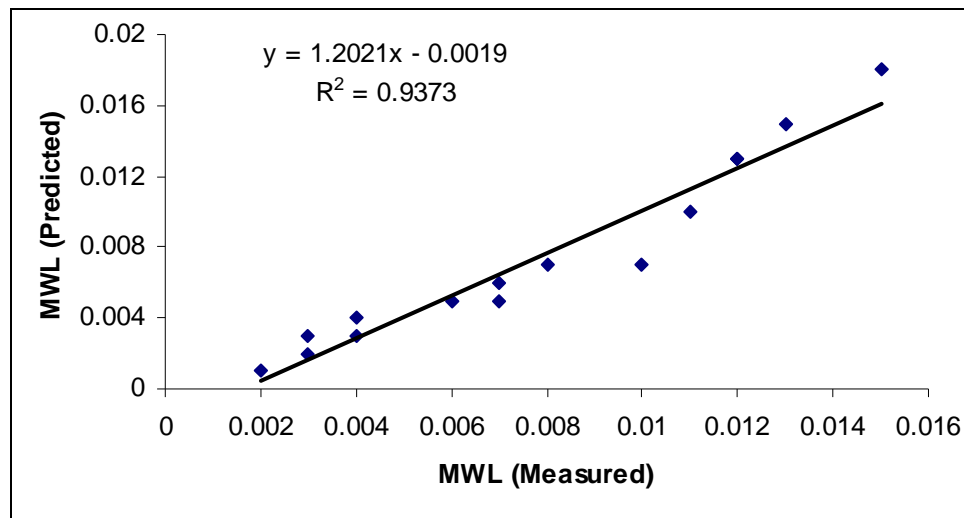


Figure A7. Predicted versus measured mean water level (setup) at Gauge 7.

Table A7. Measured and predicted significant wave height and wave setup at Gauge 8.

Test No.	Measured (m)		Predicted (m)		Difference (%)	
	$H_s$	$\bar{\eta}$	$H_s$		$H_s$	$\bar{\eta}$
Test-17	0.033	0.007	0.029	0.008	12	-2
Test-18	0.044	0.010	0.041	0.011	6	-12
Test-20	0.027	0.005	0.022	0.005	19	3
Test-21	0.039	0.008	0.035	0.009	9	-11
Test-27	0.016	0.009	0.013	0.008	16	11
Test-29	0.021	0.013	0.019	0.012	10	4
Test-30	0.024	0.014	0.024	0.015	0	-5
Test-31	0.029	0.017	0.033	0.018	-15	-10
Test-36	0.015	0.016	0.013	0.017	12	-9
Test-37	0.018	0.017	0.019	0.020	-6	-17
Test-38	0.021	0.019	0.025	0.024	-16	-23
Test-46	0.022	0.006	0.017	0.006	25	-8
Test-48	0.028	0.009	0.023	0.010	15	-10
Test-57	0.031	0.010	0.028	0.012	10	-12
Test-58	0.038	0.012	0.036	0.015	5	-24

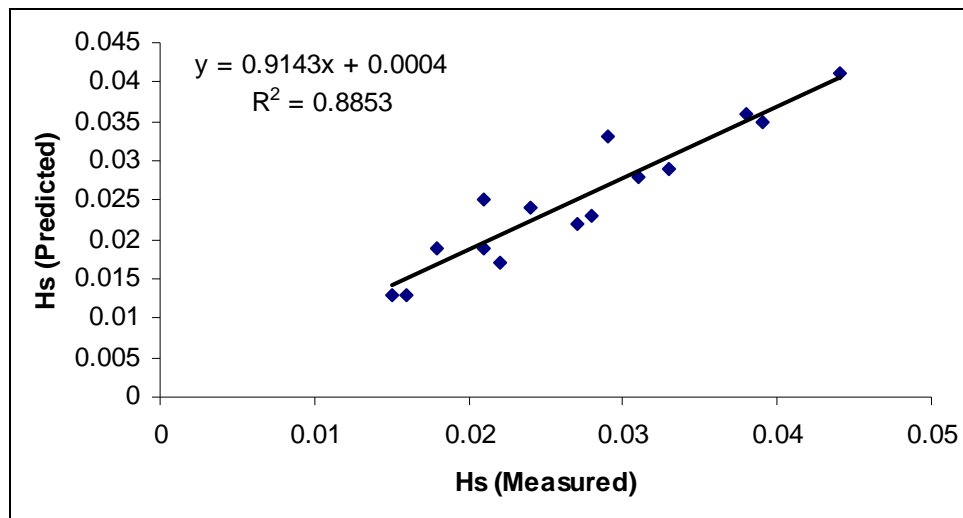


Figure A8. Predicted versus measured significant wave height at Gauge 8.

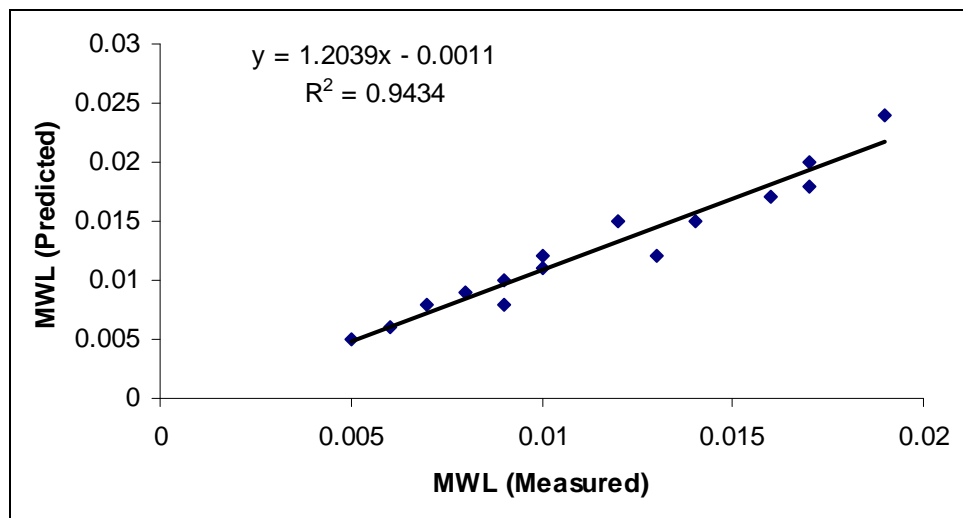


Figure A9. Predicted versus measured mean water level (setup) at Gauge 8.

Table A8. Measured and predicted significant wave height and wave setup at Gauge 9.

Test No.	Measured (m)		Predicted (m)		Difference (%)	
	$H_s$	$\bar{\eta}$	$H_s$		$H_s$	$\bar{\eta}$
Test-17	0.033	0.008	0.025	0.008	25	1
Test-18	0.046	0.010	0.040	0.012	13	-10
Test-20	0.026	0.005	0.019	0.005	28	4
Test-21	0.040	0.009	0.031	0.010	22	-7
Test-27	0.017	0.010	0.013	0.008	25	15
Test-29	0.021	0.014	0.018	0.013	12	11
Test-30	0.026	0.016	0.025	0.016	3	3
Test-31	0.033	0.018	0.036	0.019	-11	-2
Test-36	0.016	0.017	0.013	0.017	20	1
Test-37	0.021	0.020	0.020	0.021	5	-5
Test-38	0.026	0.022	0.027	0.024	-5	-10
Test-46	0.021	0.006	0.016	0.006	25	-6
Test-48	0.026	0.009	0.021	0.010	19	-6
Test-57	0.032	0.011	0.028	0.012	12	-13
Test-58	0.041	0.013	0.037	0.015	9	-18

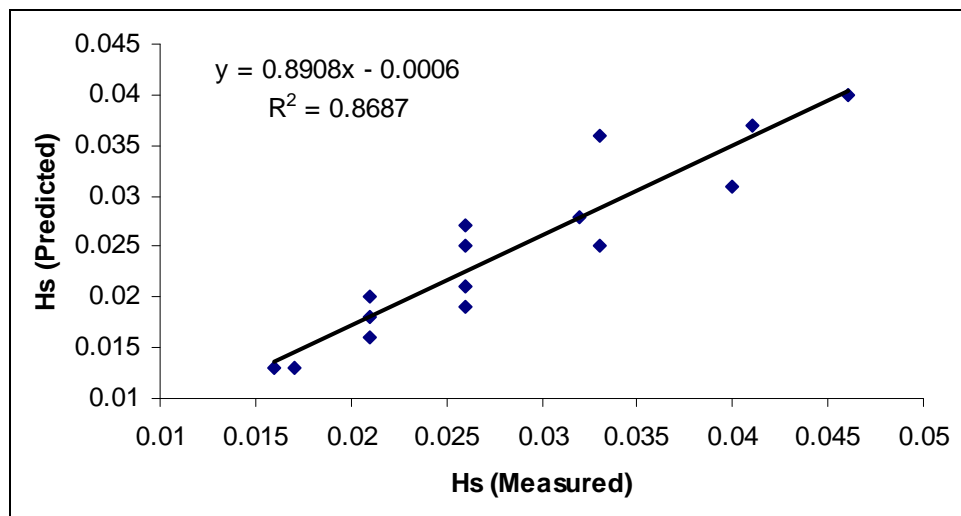


Figure A10. Predicted versus measured significant wave height at Gauge 9.

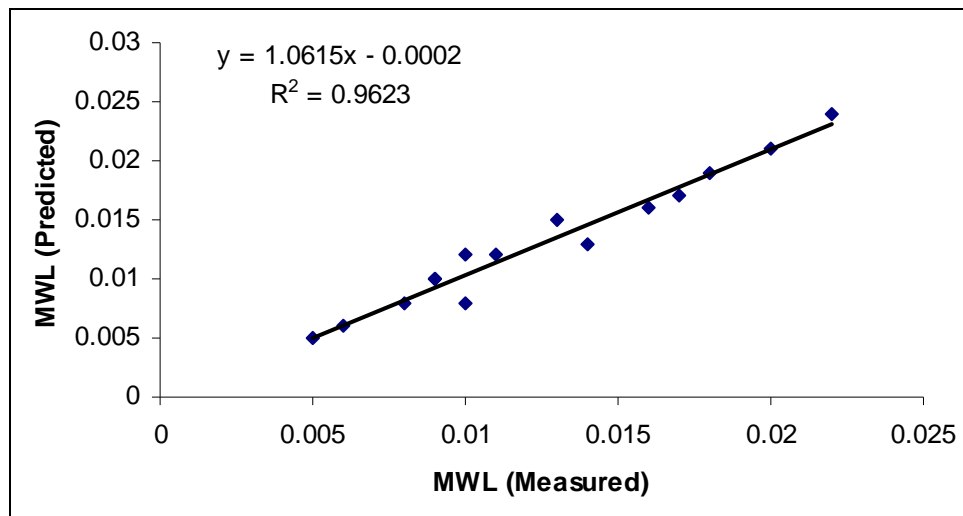


Figure A11. Predicted versus measured mean water level (setup) at Gauge 9.

Table A9. Summary of measured and calculated maximum runup heights.

Test ID	Maximum Runup Height (m)		% Difference
	Measured	Predicted	
Test-17	0.055	0.062	13
Test-18	0.084	0.090	6
Test-20	0.032	0.036	13
Test-21	0.072	0.075	4
Test-27	0.030	0.025	-16
Test-29	0.045	0.049	9
Test-30	0.060	0.064	7
Test-31	0.094	0.110	16
Test-36	0.040	0.042	6
Test-37	0.061	0.048	-21
Test-38	0.075	0.071	-5
Test-46	0.043	0.031	-29
Test-48	0.048	0.058	21
Test-57	0.075	0.066	-13
Test-58	0.083	0.083	0

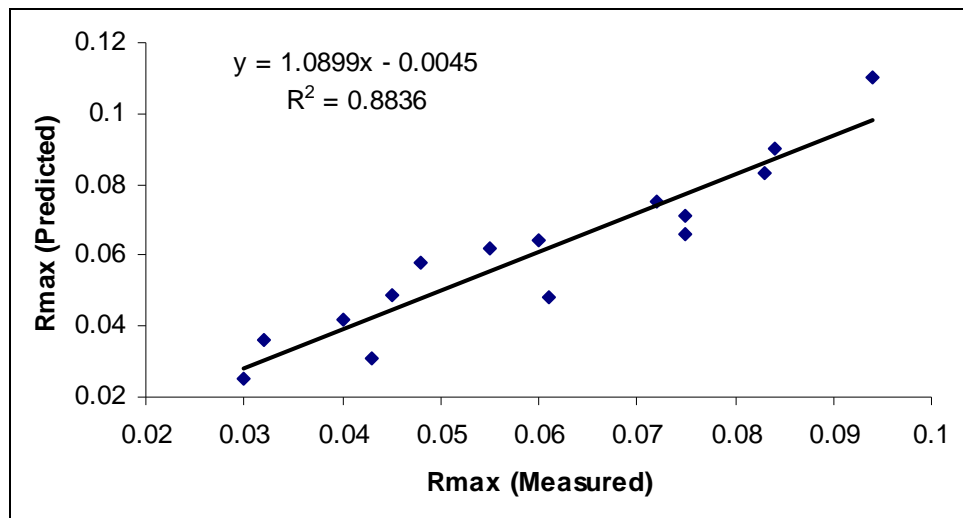


Figure A12. Predicted versus measured maximum runup at Gauge 9.

## Appendix B: Comparison of Measured Runup Values with CEM Empirical Formulae

The *Coastal Engineering Manual* (CEM) provides numerous empirical formulas for calculating regular and irregular wave runup on different geometries of sloping surfaces (beaches, structures, and shorelines). Most CEM formulas are applicable for monolithic sloping structures that are preceded by a mild offshore slope. Fringing reefs typically consist of a steep seaward face or fore-reef that plateaus at the reef crest. The reef crest is followed by a region called the reef top (or reef flat) that may be fairly wide and can be of constant depth or have shallow ponding areas. The reef top connects to the beach at the shoreline. Therefore, the majority of reef geometries are rather complex, and CEM formulae may need to be adapted to provide runup estimates for reef profiles.

The CEM provides a formula for determining irregular wave runup at the 2 percent exceedance probability level for a composite slope. It is given in Equation VI-5-7 as

$$\frac{R_{2\%}}{H_s} = \begin{cases} 1.5 \xi_{op} \gamma_r \gamma_b \gamma_h \gamma_\beta & \text{for } 0.5 < \xi_{op} < 2 \\ 3 \gamma_r \gamma_h \gamma_\beta & \text{for } \xi_{op} > 2 \end{cases} \quad (\text{B1})$$

where the  $\gamma$  factors are empirically determined corrections ( $\gamma_r$  = surface roughness,  $\gamma_b$  = berm influence,  $\gamma_h$  = wave breaking, and  $\gamma_\beta$  = wave obliqueness), and  $\xi_{op}$  is the surf-similarity parameter (Iribarren number) based on the deepwater wave parameter wave steepness:

$$\xi_{op} = \frac{\tan(\alpha)}{\sqrt{H_{m0} / L_{op}}} \quad (\text{B2})$$

where  $H_{m0}$  is the deepwater zero-moment spectral wave height,  $L_{op}$  is the deepwater wavelength based on the spectral peak period, and  $\alpha$  is the structure slope.

Equation B1 has been used to estimate the 2 percent runup limits ( $R_{2\%}$ ) for the test conditions in the University of Michigan laboratory experiments



(Demirbilek et al. 2007). The  $\gamma$  parameters were set to 1.0 while the beach slope ( $\tan \alpha = 1/12$ ) was used to calculate the surf similarity parameter.

A summary of the measured and predicted runup values are presented in Table 1 for the 15 tests used in the comparison. Wave parameters at Gauge 1 correspond to deepwater wave conditions. Values at Gauge 9 are near the toe of shore slope. Measured maximum and 2 percent runup values are listed in Table B1 with other information used in this comparison.

The  $R_{2\%}$  estimates in Table B1 have been calculated using the above CEM formula both with the significant wave height in deep water and also at the toe of shore slope. Results of comparison are shown in Figures B1 through B4. A weak correlation coefficient of 0.21 is obtained for the best fit curve to data as shown in Figure B1. The measured  $R_{2\%}$  runup is displayed in Figure B1 as a function of surf similarity parameter (Iribarren number). For measured  $R_{\max}$  runup (Figure B2), the correlation coefficient is 0.38. The correlation between measured and calculated runup in Figure B3 is weak ( $R^2 = 0.35$ ) using deepwater wave parameters. The correlation of the best fit curve between measured and calculated  $R_{2\%}$  runup based significant wave height at toe of slope is good ( $R^2 = 0.78$ ). In practice, this agreement would depend on accurate estimate of the wave height at the toe of beach.

Table B1. Measured and calculated runup estimates (calculations use CEM empirical equations.  
Runup values are in meters).

Test No.	$H_{m0}$ (m) at Gauge 1	$T_p$ (sec) at Gauge 1	$H_{m0}$ (m) at Gauge 9	$T_p$ (sec) at Gauge 9	$L_{Op}$	Surf- simpar <sup>1</sup>	$R_{2\%}$ with $H_{m0}$	$R_{2\%}$ with $H_{toe}$	$R_{max}$ (meas)	$R_{2\%}$ (meas)
Test-17	0.083	1.454	0.033	37.230	3.303	0.526	0.065	0.026	0.055	0.034
Test-18	0.092	2.029	0.046	37.380	6.430	0.698	0.096	0.048	0.084	0.064
Test-20	0.065	1.219	0.026	36.250	2.321	0.497	0.049	0.020	0.032	0.027
Test-21	0.088	1.813	0.040	36.810	5.133	0.637	0.084	0.038	0.072	0.051
Test-27	0.059	1.217	0.017	58.540	2.313	0.522	0.046	0.014	0.025	0.017
Test-29	0.075	1.439	0.021	135.850	3.231	0.546	0.062	0.017	0.040	0.028
Test-30	0.082	1.833	0.026	41.410	5.244	0.667	0.082	0.026	0.055	0.038
Test-31	0.092	2.013	0.033	40.130	6.327	0.691	0.095	0.034	0.090	0.049
Test-36	0.073	1.445	0.016	34.260	3.261	0.559	0.061	0.014	0.020	0.009
Test-37	0.082	1.814	0.021	52.770	5.135	0.661	0.081	0.021	0.041	0.015
Test-38	0.091	2.010	0.026	51.120	6.307	0.694	0.095	0.027	0.055	0.021
Test-46	0.062	1.218	0.021	36.850	2.317	0.509	0.047	0.016	0.043	0.030
Test-48	0.079	1.450	0.026	39.930	3.280	0.537	0.064	0.021	0.048	0.041
Test-57	0.083	1.836	0.032	38.170	5.264	0.664	0.083	0.032	0.075	0.055
Test-58	0.092	2.024	0.041	38.130	6.395	0.693	0.096	0.042	0.083	0.062

<sup>1</sup> Surf similarity parameter.

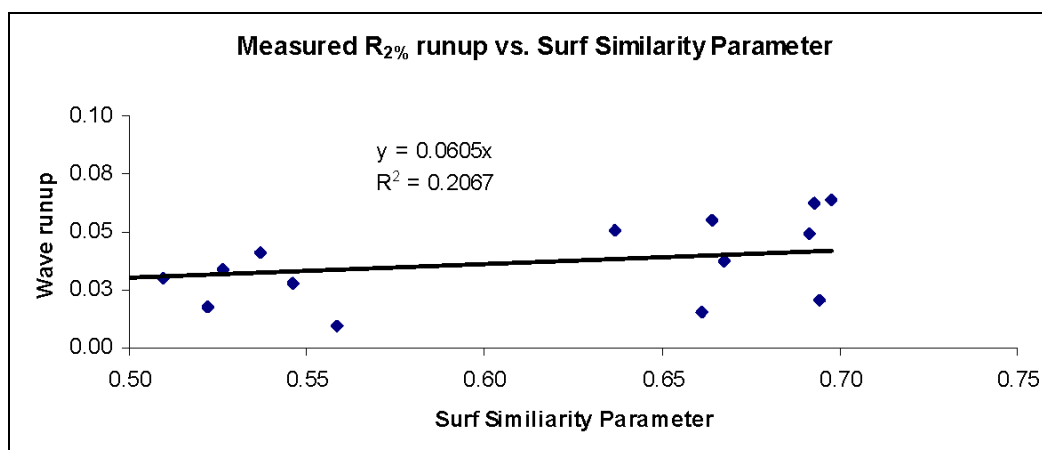


Figure B1. Measured  $R_{2\%}$  runup versus surf similarity parameter (Iribarren number).

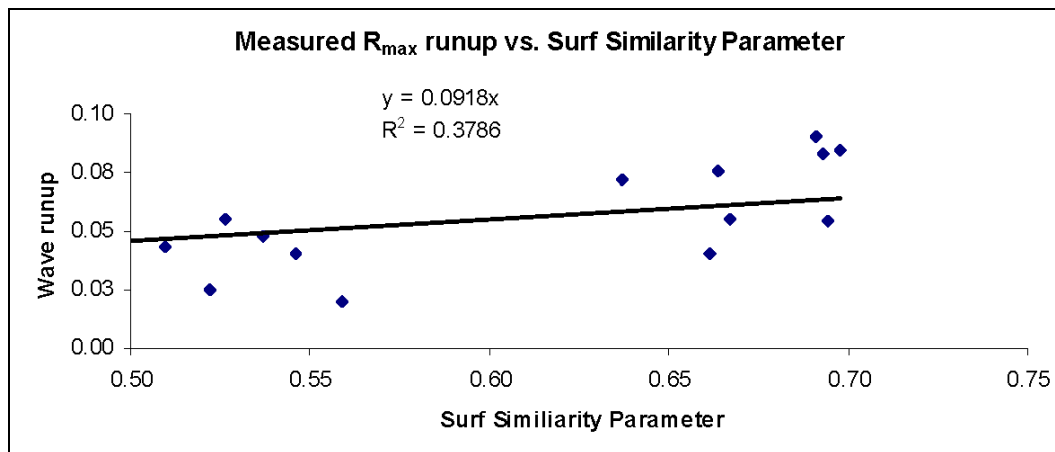


Figure B2. Measured  $R_{max}$  runup versus surf similarity parameter (Irribaren number).

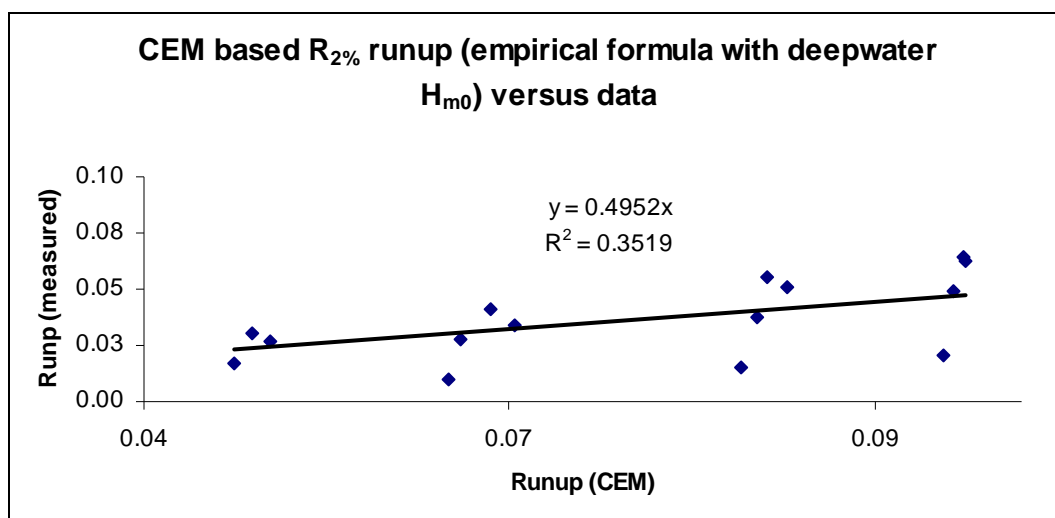


Figure B3. Correlation of best fit curve between measured  $R_{2\%}$  runup and CEM empirical runup estimates based on deepwater wave parameters.

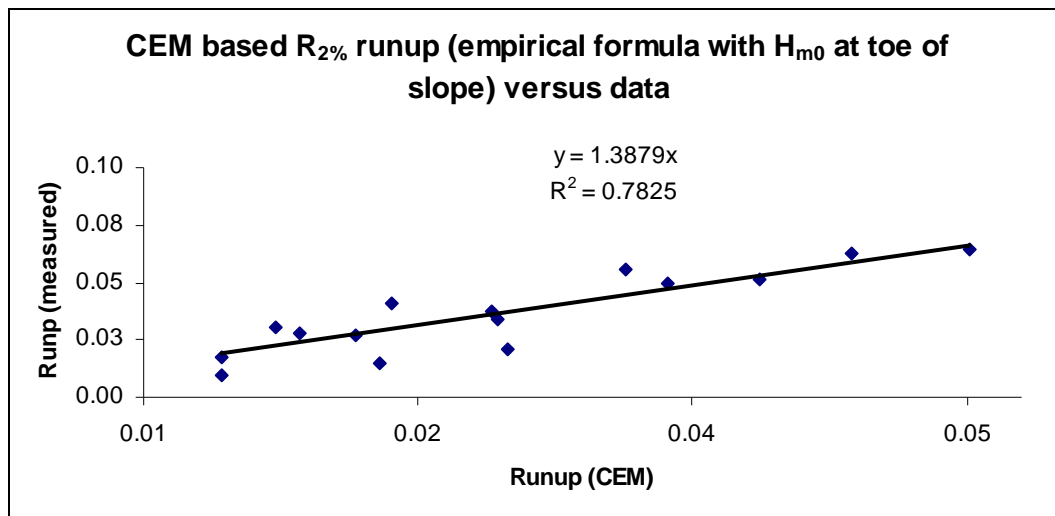


Figure B4. Measured  $R_{2\%}$  runup and CEM empirical runup estimates based significant wave height at toe of shore slope.

## Appendix C: Comparison of Measured and Calculated Wave Heights for Guam Field Experiments

Table C1. Measured and predicted significant wave heights AQD44.

Event No.	Measured (m)	Predicted (m)	Difference (%)
Event-243	0.099	0.093	6
Event-252	0.161	0.198	-23
Event-264	0.321	0.363	-13
Event-282	0.261	0.284	-9
Event-294	0.304	0.328	-8
Event-306	0.173	0.197	-14
Event-318	0.089	0.054	39

Table C2. Measured and predicted significant wave heights SBE78.

Event No.	Measured (m)	Predicted (m)	Difference (%)
Event-243	0.143	0.123	14
Event-252	0.214	0.264	-23
Event-264	0.410	0.443	-8
Event-282	0.339	0.359	-6
Event-294	0.414	0.394	5
Event-306	0.257	0.265	-3
Event-318	0.128	0.049	61

Table C3. Measured and predicted significant wave heights at AQD48.

Event No.	Measured (m)	Predicted (m)	Difference (%)
Event-243	0.344	0.341	1
Event-252	0.392	0.447	-14
Event-264	0.586	0.691	-18
Event-282	0.513	0.572	-11
Event-294	0.494	0.619	-25
Event-306	0.357	0.451	-27
Event-318	0.350	0.300	14

Table C4. Measured and predicted significant wave heights at SBE79.

Event No.	Measured (m)	Predicted (m)	Difference (%)
Event-243	0.288	0.702	-144
Event-252	0.387	0.586	-51
Event-264	0.553	0.941	-70
Event-282	0.568	0.762	-34
Event-294	0.563	0.856	-52
Event-306	0.426	0.590	-39
Event-318	0.256	0.635	-148

Table C5. Measured and predicted significant wave heights at AQD57.<sup>1</sup>

Event No.	Measured (m)	Predicted (m)	Difference (%)
Event-243	0.605	0.603	0
Event-252	0.613	0.586	4
Event-264	0.942	0.941	0
Event-282	0.841	0.852	-1
Event-294	0.879	0.856	3
Event-306	0.642	0.645	0
Event-318	0.450	0.635	-41

<sup>1</sup> Field gauge location was moved 15m shoreward in numerical model.

Table C6. Measured and predicted significant wave heights at SBE80.

Event No.	Measured (m)	Predicted (m)	Difference (%)
Event-243	0.245	0.856	-250
Event-252	0.425	1.770	-316
Event-264	0.939	2.069	-120
Event-282	0.802	1.957	-144
Event-294	0.872	1.949	-123
Event-306	0.558	1.779	-219
Event-318	0.205	1.539	-650

Table C7. Measured and predicted significant wave heights at AQD60.

Event No.	Measured (m)	Predicted (m)	Difference (%)
Event-243	1.896	2.049	-8
Event-252	1.872	1.987	-6
Event-264	1.920	2.206	-15
Event-282	1.930	2.270	-18
Event-294	1.818	1.894	-4
Event-306	1.648	2.040	-24
Event-318	1.765	1.921	-9

REPORT DOCUMENTATION PAGE				Form Approved OMB No. 0704-0188	
Public reporting burden for this collection of information is estimated to average 1 hour per response, including the time for reviewing instructions, searching existing data sources, gathering and maintaining the data needed, and completing and reviewing this collection of information. Send comments regarding this burden estimate or any other aspect of this collection of information, including suggestions for reducing this burden to Department of Defense, Washington Headquarters Services, Directorate for Information Operations and Reports (0704-0188), 1215 Jefferson Davis Highway, Suite 1204, Arlington, VA 22202-4302. Respondents should be aware that notwithstanding any other provision of law, no person shall be subject to any penalty for failing to comply with a collection of information if it does not display a currently valid OMB control number. <b>PLEASE DO NOT RETURN YOUR FORM TO THE ABOVE ADDRESS.</b>					
1. REPORT DATE (DD-MM-YYYY) December 2007		2. REPORT TYPE Final report		3. DATES COVERED (From - To)	
4. TITLE AND SUBTITLE  Boussinesq Modeling of Wave Propagation and Runup over Fringing Coral Reefs, Model Evaluation Report				5a. CONTRACT NUMBER	
				5b. GRANT NUMBER	
				5c. PROGRAM ELEMENT NUMBER	
6. AUTHOR(S)  Zeki Demirbilek and Okey G. Nwogu				5d. PROJECT NUMBER	
				5e. TASK NUMBER	
				5f. WORK UNIT NUMBER	
7. PERFORMING ORGANIZATION NAME(S) AND ADDRESS(ES) U.S. Army Engineer Research and Development Center Coastal and Hydraulics Laboratory 3909 Halls Ferry Road, Vicksburg, MS 39180-6199; University of Michigan Department of Naval Architecture and Marine Engineering 2600 Draper Road, Ann Arbor, MI 48109-2145				8. PERFORMING ORGANIZATION REPORT NUMBER  ERDC/CHL TR-07-12	
9. SPONSORING / MONITORING AGENCY NAME(S) AND ADDRESS(ES) Headquarters, U.S. Army Corps of Engineers Washington, DC 20314-1000				10. SPONSOR/MONITOR'S ACRONYM(S)	
				11. SPONSOR/MONITOR'S REPORT NUMBER(S)	
12. DISTRIBUTION / AVAILABILITY STATEMENT  Approved for public release; distribution is unlimited.					
13. SUPPLEMENTARY NOTES					
14. ABSTRACT <p>This report describes evaluation of a two-dimensional Boussinesq-type wave model, BOUSS-2D, with data obtained from two laboratory experiments and two field studies at the islands of Guam and Hawaii, for waves propagating over fringing reefs. The model evaluation had two goals: (a) investigate differences between laboratory and field characteristics of wave transformation processes over reefs, and (b) assess overall predictive capabilities of the model for reef systems with steep slopes and extended widths in shallower water. The focus in this evaluation study was on wave breaking, bottom friction parameterization, and wave setup and runup capabilities of Boussinesq wave model.</p> <p>In this report, the testing procedure and performance of the Boussinesq wave model are discussed. Because details of the laboratory and field studies were unavailable at the time of writing, and these are expected to be documented in other reports, only some general features of data pertinent to the numerical modeling study are presented. The time series of laboratory and field data were used in the numerical model validation study. These were converted to wave energy spectral densities, significant wave height, peak wave period, and mean water level setup for comparison to model predictions. Findings from comparisons of measurements and model calculations are presented in figures and tables, and these are supplemented as necessary with</p> <p style="text-align: right;">(Continued)</p>					
15. SUBJECT TERMS		Directional wave spectrum		Turbulence, Smargorinsky dissipation	
Bottom friction		Low-frequency oscillations		Wave setup	
Boussinesq wave model		Spilling and plunging breaking waves		Wave propagation	
				Wave runup	
16. SECURITY CLASSIFICATION OF:			17. LIMITATION OF ABSTRACT	18. NUMBER OF PAGES	19a. NAME OF RESPONSIBLE PERSON
a. REPORT	b. ABSTRACT	c. THIS PAGE			19b. TELEPHONE NUMBER (include area code)
UNCLASSIFIED	UNCLASSIFIED	UNCLASSIFIED		110	



#### **14. ABSTRACT (Concluded)**

discussion of the model's capability in describing different wave processes over coral reefs. Overall, the model performed reasonably well for laboratory data with errors of less than 10 percent for the maximum runup height. For the field data, it was determined that wave energy dissipation over extremely rough coral reef surfaces could not be simply described by a quadratic bottom friction law. Reasonable model-data agreement was obtained by using an eddy-viscosity type term to parameterize wave energy dissipation due to the turbulent boundary layer over rough coral reef bottoms.